THE PLANETARY SCIENCE JOURNAL, 6:150 (33pp), 2025 June https://doi.org/10.3847/PSJ/add46a

Surface Ages for the Sample Return Asteroids Bennu, Ryugu, and Itokawa

William F. Bottke[1], Alex J. Meyer[2], David Vokrouhlický[3], David Nesvorný[1], Edward B. Bierhaus[4], Daniella N. DellaGiustina[5], Rachael Hoover[1], Harold C. Connolly[6], and Dante S. Lauretta[5]
[1] Southwest Research Institute, 1050 Walnut St., Suite 300, Boulder, CO 80302, USA; william.bottke@swri.org
[2] University of Colorado Boulder, 3775 Discovery Dr., Boulder, CO 80309, USA
[3] Institute of Astronomy, Charles University, V Holešovičkách 2, CZ-18000, Prague 8, Czech Republic
[4] Lockheed Martin Space, Littleton, CO 80127, USA
[5] Lunar and Planetary Laboratory, University of Arizona, Tucson, AZ 85721, USA
[6] Department of Geology, Rowan University, Glassboro, NJ 08028, USA
Received 2024 August 29; revised 2025 April 14; accepted 2025 May 1; published 2025 June 30

Abstract

The OSIRIS-REx, Hayabusa2, and Hayabusa missions have returned samples from three near-Earth asteroids (NEAs), namely Bennu, Ryugu, and Itokawa, respectively. Insights into the geological and dynamical history of these NEAs can be gleaned by linking their surface ages, derived by modeling the production of their crater size–frequency distributions, to the cosmic-ray exposure (CRE) ages of their samples. The complication is that as these NEAs traveled from the main belt to their observed orbits, the impactor flux striking them from main-belt asteroids, Mars-crossing asteroids, and NEAs also changed. Here we account for these factors by allowing Bennu, Ryugu, and Itokawa to dynamically evolve within a crater production model. Each world was tracked over many tens of different orbital pathways. Crater erasure effects, produced by superposed craters, sandblasting effects, and the impact-driven mass movement of surface materials, were also included, with the latter parameterized using a crater damage function. Surface ages were determined by comparing model crater size–frequency distributions to the observed ones. Our results yielded median surface age values for Bennu, Ryugu, and Itokawa of 7.7, 4.1, and 3.2 Myr old, respectively. These model ages are broadly consistent with the CRE ages measured from the returned samples. We suggest that these model ages may represent the timing of global resurfacing events, with the most likely mechanisms being shattering impacts from main-belt projectiles and YORP-driven spin up. When combined with cratering events, we predict that near-surface materials on Bennu, Ryugu, and Itokawa have experienced considerable churn with time.

Unified Astronomy Thesaurus concepts: Asteroid dynamics (2210); Near-Earth objects (1092); Asteroid belt (70); Meteorites (1038); Impact phenomena (779); Craters (2282)

1. Introduction

The primary goals of NASA's OSIRIS-REx and JAXA's Hayabusa/Hayabusa2 missions were to collect materials from different kinds of near-Earth asteroids (NEAs) and return them to Earth for further study. OSIRIS-REx flew to (101955) Bennu (formerly 1999 RQ36), a 0.506 × 0.492 × 0.457 km diameter B-type NEA (D. S. Lauretta et al. 2017, 2019, 2022), while Hayabusa2 went to (162173) Ryugu (formally 1999 JU3), a 1.04 × 1.02 × 0.88 km diameter Cb-type NEA (S. Watanabe et al. 2017, 2019; S. Sugita et al. 2019; T. Yada et al. 2021; S. Tachibana et al. 2022) (Figure 1). Hayabusa flew to (25143) Itokawa, a 0.535 × 0.294 × 0.209 km S(IV)-type NEA with an ordinary chondrite composition (M. Yoshikawa et al. 2015; see Figure 1). All three missions were successful, with the returned samples now being subjected to a battery of tests by worldwide scientists. Key goals of these missions were to combine spacecraft and sample data together to constrain the geological and dynamical history of Bennu, Ryugu, and Itokawa and explore the origin of their parent bodies.

The parent body/bodies of Bennu and Ryugu were likely born as planetesimals within the giant planet zone, the probable source region of many carbonaceous chondrites (T. Kleine et al. 2020). The question whether Bennu and Ryugu came from one or two different parent bodies has yet to be answered (e.g., W. F. Bottke et al. 2015b), but distinct populations of exogenic impactors on their respective surfaces may indicate that they are at least once removed from the same parent asteroid (D. N. DellaGiustina et al. 2021; E. Tatsumi et al. 2021a, 2021b; K. J. Walsh et al. 2024). Their parent bodies were delivered to the main-belt zone by dynamical processes taking place when the solar nebula still existed (K. J. Walsh et al. 2011; S. N. Raymond & A. Izidoro 2017).

The parent body of Itokawa likely formed in the inner solar system within what is now called the non−carbonaceous chondrite zone (T. Kleine et al. 2020). Itokawa's parent body either was indigenous to the main belt or formed in the terrestrial planet zone and was later captured into the main belt by dynamical processes associated with early solar system evolution (e.g., W. F. Bottke et al. 2006a; K. J. Walsh et al. 2011; S. N. Raymond & A. Izidoro 2017; C. Avdellidou et al. 2024).

The original diameters of all three parent bodies were on the order of 100 km or larger (W. F. Bottke et al. 2005b, 2005a, 2015b; A. Morbidelli et al. 2009). Each parent body likely experienced thermal evolution, cratering events, and probable disruption event(s) within the inner main belt (e.g., K. J. Walsh et al. 2013; W. F. Bottke et al. 2015b, 2020; D. Vokrouhlický et al. 2017).

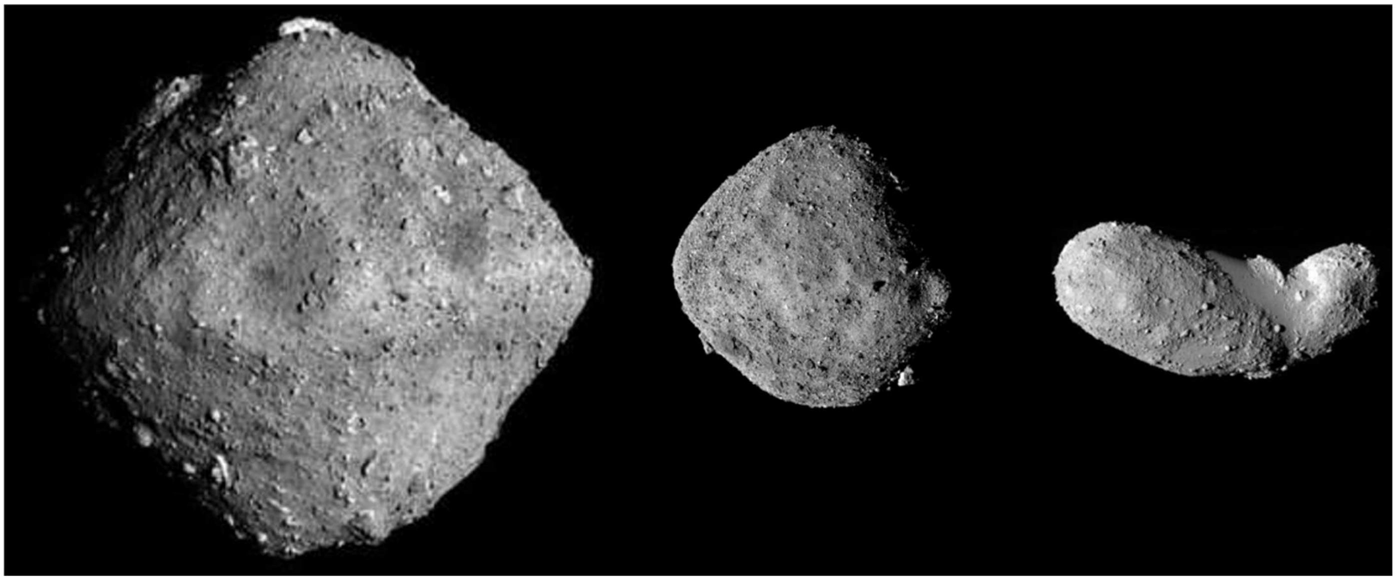

Figure 1. The sample-return NEAs. Ryugu (left) is a Cb-type asteroid that was sampled by Hayabusa2. It has a mean diameter of 896 m and a bulk density of 1.19 ± 0.02 g cm^{-3} (S. Watanabe et al. 2019). Bennu (middle) is a B-type asteroid that was sampled by the OSIRIS-REx mission. It has a mean diameter of 492 m and a bulk density of 1.190 ± 0.013 g cm^{-3} (D. S. Lauretta et al. 2019). Itokawa (right) is an S-type asteroid that was sampled by the Hayabusa mission. It has dimensions of 0.535 km × 0.294 km × 0.209 km and an estimated bulk density of 1.9 ± 0.13 g cm^{-3} (A. Fujiwara et al. 2006). Images courtesy of NASA/JAXA.

The immediate precursors of Bennu, Ryugu, and Itokawa were probably reassembled from debris ejected by the disruption of their parent bodies (P. Michel et al. 2020). These subkilometer-to-kilometer-sized fragments traversed the main belt over many hundreds of Myr or more via Yarkovsky thermal forces and resonances (e.g., W. F. Bottke et al. 2006b, 2015b, 2020; H. Campins et al. 2010, 2013; K. J. Walsh et al. 2013). While in transit, these precursors experienced one or more shattering or disruption events, with the last one yielding the approximate sizes of Bennu, Ryugu, and Itokawa (K. J. Walsh et al. 2024).

Note that some have argued that small rubble-pile asteroids like Itokawa are difficult to destroy by impacts and instead may survive for many billions of years in the main belt (F. Jourdan et al. 2023). This scenario, however, is incompatible with collisional evolution modeling results of how the main belt and asteroid families evolve (W. F. Bottke et al. 2015a), as well as recent numerical results showing how the DART spacecraft's impact into Dimorphos reshaped the 160 m diameter S-type body (S. D. Raducan et al. 2024).

Ryugu is about twice as large as Bennu (Figure 1), but both have top-like shapes and a rubble-pile structure (D. S. Lauretta et al. 2019; S. Watanabe et al. 2019). The term "rubble pile" is defined in D. C. Richardson et al. (2002). The objects also share the same bulk density of 1.19 g cm^{-3} and geometric albedo of ∼4.5% (S. R. Chesley et al. 2014; D. S. Lauretta et al. 2019; S. Watanabe et al. 2019). As mentioned above, both asteroids also have a small quantity of nonindigenous rocks on their surface (D. N. DellaGiustina et al. 2021; E. Tatsumi et al. 2021a, 2021b). These materials may be the remnants of projectiles that hit either their parent bodies or their precursor bodies while transiting out of the main belt.

Itokawa has two major lobes and is elongated in shape (H. Demura et al. 2006). It likely has a rubble-pile structure, but it is possible that the two lobes also have different bulk densities, with at least one large component within one of the lobes (S. C. Lowry et al. 2014; M. Kanamaru et al. 2019). Like Bennu and Ryugu, Itokawa was probably reassembled from materials ejected from the disruption of Itokawa's parent body (P. Michel et al. 2020). Itokawa has regions that are boulder-rich and those that are dominated by centimeter- and sub-centimeter-sized particles. Overall, Itokawa has a bulk density of 1.9 g cm^{-3} and a geometric albedo of ∼23% (A. Fujiwara et al. 2006).

Samples from Ryugu appear to be a compositional match with Ivuna-type CI chondrites (T. Nakamura et al. 2023; T. Yokoyama et al. 2023b). They are chemically unfractionated yet are aqueously altered. These properties are consistent with Ryugu's spectral properties (E. Tatsumi et al. 2021c). Similarly, Bennu particles seem to have many of the properties of average CI chondrites (D. S. Lauretta et al. 2024). D. S. Lauretta et al. (2024) report that Bennu samples have a similar elemental composition to Ryugu samples, but without refractory element enrichments (T. Nakamura et al. 2023; T. Yokoyama et al. 2023a). CI chondrites are among the weakest extraterrestrial bodies so far known (e.g., O. Eugster et al. 2006). Both the OSIRIS-REx and Hayausa2 spacecraft found evidence for extremely weak materials on the surface Bennu and Ryugu (e.g., R. Jaumann et al. 2019; M. Arakawa et al. 2020; R.-L. Ballouz et al. 2020; B. Rozitis et al. 2020; M. E. Perry et al. 2022; T. Nakamura et al. 2023). Given their limited prospects for passing through Earth's atmosphere intact, it is fair to say that our understanding of primitive carbonaceous chondrites suffers from sample bias. The existence of such fragile materials on Bennu and Ryugu also raises intriguing questions about how they survived on worlds that have been disrupted multiple times (K. J. Walsh et al. 2024).

While preliminary analysis has only begun for Bennu's samples, the particles show signs of aqueous alteration events occurring within an evolving briny fluid (K. A. McCain et al. 2023; T. Nakamura et al. 2023; T. Yokoyama et al. 2023b; D. S. Lauretta et al. 2024; T. J. McCoy et al. 2025). Water flow probably took place within the parent bodies of both asteroids, with supporting evidence found in the carbonates identified on the surfaces of Bennu and Ryugu (V. E. Hamilton et al. 2019; H. H. Kaplan et al. 2020; Y. Hu et al. 2024).

The Itokawa particles returned by the Hayabusa spacecraft match LL-type ordinary chondrites (T. Nakamura et al. 2011). Their composition confirmed the link between S-type asteroids, a common asteroid type among NEAs and main-belt bodies, and ordinary chondrites, the most common type of meteorite fall (T. H. Burbine et al. 2002). Ordinary chondrites are denser and stronger than CI, CM, and CR meteorites, which may in part explain why they make up many of the falls and finds residing in meteorite collections across the world (T. H. Burbine et al. 2002; O. Eugster et al. 2006).

In this paper, we will explore the collisional and dynamical evolution histories of Bennu, Ryugu, and Itokawa. Our goal is to set the stage for the interpretation of samples from all three missions. For example, cosmic-ray exposure (CRE) or space-weathering processes measured on returned samples may help us deduce how the surfaces of these NEAs have changed over relatively recent times from collisions, thermal torques like the Yarkovsky–O'Keefe–Radzievskii–Paddack (YORP) effect (D. P. Rubincam 2000), or tidal disruption of NEAs (D. C. Richardson et al. 1998). Concerning YORP, this mechanism can spin small asteroids up fast enough to produce mass movement and mass shedding (e.g., K. J. Walsh et al. 2008; D. Vokrouhlický et al. 2015). It is also possible that some samples will eventually show evidence for shock degassing processes produced by impact events, as has already been deduced for Itokawa (J. Park et al. 2015; K. Terada et al. 2018). If so, they might provide ground truth for when their parent body disrupted (e.g., W. F. Bottke et al. 2020).

With that said, placing Bennu, Ryugu, and Itokawa samples into an appropriate geologic context is challenging, with several complicating factors affecting the collisional and dynamical evolution of NEAs. Here are some examples.

Dynamical evolution of NEAs. The orbits of all three NEAs have changed with time (e.g., W. F. Bottke et al. 2002; M. Granvik et al. 2016, 2018; D. Nesvorný et al. 2023). Numerical models indicate that they traveled from the main belt to their current orbits in NEA space via dynamical resonances and encounters with the terrestrial planets (H. Campins et al. 2010, 2013; K. J. Walsh et al. 2013; W. F. Bottke et al. 2015b). Each body's trek was chaotic, such that we can only determine their past paths in a probabilistic sense.

As an analogy, consider trying to predict what happened to several balls within a Pachinko machine if you could only observe them at the very bottom. One could use a Monte Carlo code to calculate the most likely pathways for each ball, with certain starting positions more likely to produce a given bottom position than others, but the exact path followed by each ball will never be known.

Collisional evolution of NEAs. En route to their current orbits, Bennu, Ryugu, and Itokawa were struck by different subpopulations of asteroids, namely those from the main belt, those on solely Mars-crossing orbits, and those of other NEAs (W. F. Bottke et al. 1996, 2002). The degree of bombardment that each body experienced from these different impactor populations is established by the dynamical pathways they followed, which, as mentioned above, can only be determined in a probabilistic sense.

Missing small craters. Many small craters on Bennu, Ryugu, and Itokawa are missing compared to expectations from crater size–frequency distributions (SFDs) on the Moon (N. Hirata et al. 2009; S. Sugita et al. 2019; K. J. Walsh et al. 2019; D. N. DellaGiustina et al. 2020; Y. Cho et al. 2021; E. B. Bierhaus et al. 2022, 2023). This is not unusual; all observed NEAs are missing small craters at some level (S. Marchi et al. 2015; W. F. Bottke et al. 2020). The largest craters on NEAs are often considered to be in production, such that they are commonly used to calculate model surface ages. The simplest interpretation is that largest craters record the time of the last global resurfacing event on a given NEA. We caution, though, that this idea could be misleading if a given asteroid has experienced regional resurfacing events.

Our method to deal with these obstacles was to construct a versatile crater production model called NEA-EVOL. It includes (i) results from models showing how NEAs dynamically escape the main belt and evolve within the inner solar system, (ii) algorithms that track how the impact flux changes from different populations as the NEAs travel through the main belt and terrestrial planet-crossing region, and (iii) a realistic crater evolution code that can reasonably account for complex issues like crater erasure produced by superposed craters, sandblasting effects, and the impact-driven mass movement of surface materials. Together, NEA-EVOL allows us to simulate the full end-to-end evolution of Bennu, Ryugu, and Itokawa, with many characteristics treated with more realism than was previously possible. In turn, our results hopefully provide new ways to interpret the crater histories from and sample ages of Bennu, Ryugu, and Itokawa.

The structure of this paper is as follows: We first discuss how Bennu, Ryugu, and Itokawa likely reached their current orbits, as well as their probable parent bodies (and parent asteroid families; Sections 2.1–2.2). Next, we describe different ways in which they could have had their surfaces reset by shattering impacts, YORP spin-up, or tidal disruption (Sections 2.3–2.6). The crater SFDs of Bennu, Ryugu, and Itokawa are discussed in Section 3. From there, we describe the components of NEA-EVOL, including the nature of the various impactor populations; the crater scaling laws used for Bennu, Ryugu, and Itokawa; and how we treat crater formation and erasure within a separate code called CRASAT (Section 4). Our results for each asteroid are presented in Section 5, along with some discussion on how these surface ages compare to the CRE ages of the returned samples, as well as the ages found within various meteorite groups. These results lead into a discussion section on the mechanisms producing global resurfacing ages on small NEAs, as well as the meaning behind the dichotomy in CRE ages between weak and strong meteorite classes (Section 6). Finally, we summarize our conclusions in Section 7.

2. The Evolution of Bennu, Ryugu, and Itokawa

2.1. Overview

To set the stage for our work, it is useful to describe what happens to NEAs as they evolve from the main belt to Bennu-, Ryugu-, and Itokawa-like orbits. The orbits of these bodies, which by definition are highly accessible for missions (e.g., P. A. Abell et al. 2009), are similar to that of Earth, namely, they have a semimajor axis near 1 au, low eccentricities, and low inclinations.

Numerical simulations indicate that most main-belt asteroids smaller than $D < 10$ km were produced by collisions on objects that were $D > 100$ km in diameter (e.g., W. F. Bottke et al. 2005b, 2015a, 2015b, 2020). Large-scale collisions that occurred over the past several hundreds of millions of years to a few billion years ago frequently leave behind clusters of fragments in semimajor axis, eccentricity, and inclination space and are referred to as asteroid families (e.g., D. Nesvorný et al. 2015). The leading candidate families to have produced Bennu and Ryugu are Eulalia and New Polana, with the observable contributions located at low inclinations between 2.4 and 2.49 au (e.g., H. Campins et al. 2010; K. J. Walsh et al. 2013; W. F. Bottke et al. 2015b). This puts them just sunward of the 3:1 mean motion resonance with Jupiter (J3:1) at 2.5 au.

Spectroscopic investigations of whether the New Polana and Eulalia families can produce Bennu and Ryugu have generally yielded favorable results, but issues of uniqueness remain. For example, ground-based observations of 65 asteroids in New Polana/Eulalia region by J. de León et al. (2016) and N. Pinilla-Alonso et al. (2016) showed a spread of spectral slopes, from blue to moderately red, all of which are characteristic of B- and C-type asteroids. They argued that their visible spectra were consistent with Bennu and Ryugu but that there was not enough diagnostic information in the signatures to distinguish between the two families or the background population.

Using the same spectra, M. Brož et al. (2024) used an asteroid evolution model to claim that the Polana family is the likely source of both Ryugu and Bennu, though they did not distinguish between New Polana and Eulalia. As part of their work, they asserted that Polana members fit well with C-, Cb-, and Cg-type asteroid spectra, with those worlds displaying a broad convex band centered around 1.1–1.3 μm that is characteristic of CI chondrites, as found for Bennu and Ryugu samples.

Similarly, using asteroid reflectance spectra in Gaia Data Release 3, M. Delbo et al. (2023) showed that the average reflectance spectra of the Eulalia and New Polana families were the most similar to Bennu and Ryugu out of all candidate families in the inner main belt. More discordantly, D. Takir et al. (2024) used ground-based spectra to show that (142) Polana does not exhibit a 3 μm hydrated mineral absorption feature, while Bennu has such a signature (V. E. Hamilton et al. 2019). This could mean that Bennu did not come from the New Polana family or that the interior of the Polana parent body had diverse levels of aqueous alteration.

Here we will assume that the New Polana and Eulalia families are the sources of Bennu and Ryugu. According to a numerical analysis of family and NEA evolution by W. F. Bottke et al. (2015b), the New Polana and Eulalia families have a ∼70% and ∼30% probability of producing Bennu, respectively, while they have a ∼15% and 85% probability of yielding Ryugu, respectively. Their predicted ages for the New Polana and Eulalia families were 1400 [+150, −150] Ma and 830 [+370, −100] Ma, respectively.

Returned samples from Itokawa indicate that it has an LL chondrite–type composition ranging from metamorphic type 4 to 6 (T. Nakamura et al. 2011; A. Tsuchiyama et al. 2013). Flora family members, also located along the inner edge of the main belt next to the ν_6 resonance at low to medium inclinations, have Itokawa-like spectra consistent with LL-type chondrites (P. Vernazza et al. 2008; J. de León et al. 2010; T. L. Dunn et al. 2013; R. P. Binzel et al. 2019). Dynamical models of the NEA population from W. F. Bottke et al. (2002) and M. Granvik et al. (2018) suggest that there is an ∼86%–100% probability that Itokawa came from the innermost region of the main belt. These results are consistent with an origin within the Flora family.

Several grains from Itokawa yield ^{40}Ar/^{39}Ar shock degassing ages of 1.3 ± 0.3 Gyr old (J. Park et al. 2015), while multiple phosphate grains dated using the U–Pb system provide reset ages of 1.51 ± 0.85 Gyr old (K. Terada et al. 2018). These ages are possibly dating the disruption of the parent body that formed Itokawa's precursor, though some dispute this (F. Jourdan et al. 2023). The best available dynamical evolution models of the Flora family suggest that it is 1.35 ± 0.3 Gyr old (D. Vokrouhlický et al. 2017; see also M. J. Dykhuis et al. 2014). These ages are also consistent with the inferred crater retention age of (951) Gaspra, a Flora family member observed by the Galileo spacecraft (W. F. Bottke et al. 2020). When all these components are put together, one can make a strong case that Itokawa and its precursors were once members of the Flora family and that the family formed approximately 1.3–1.4 Gyr ago from a catastrophic impact event.

Many newly formed bodies made by catastrophic collisions or large-scale cratering events are agglomerations of smaller rocky components that have become gravitationally bound to one another (e.g., P. Michel et al. 2020). Bodies that consist of reaccumulated rocky debris weakly bound under the influence of gravity are called rubble-pile asteroids (D. C. Richardson et al. 2002). Their shapes can take on many forms, from "top-like" (e.g., Bennu and Ryugu) to "potato-like" (Itokawa) (Figure 1).

Once created, asteroids with diameter $D < 30$ km obtain mobility from the Yarkovsky effect, a thermal radiation force that causes asteroids to drift inward toward or outward away from the Sun via the absorption and reemission of sunlight (see reviews in W. F. Bottke et al. 2006b and D. Vokrouhlický et al. 2015). The drift direction depends on the orientation of the spin axis; retrograde spinning objects migrate inward, and prograde spinning objects move outward.

The bodies also undergo a thermal torque called the YORP effect (D. P. Rubincam 2000; see reviews in W. F. Bottke et al. 2006b; D. Vokrouhlický et al. 2015). It modifies the spin vector of the bodies. Depending on their shape, the torque can spin them up or down while also moving their obliquities to values near $\delta \sim 0°$ or 180°. The dominance of these extreme obliquity values for small main-belt asteroids has been confirmed using data from the Gaia spacecraft (J. Ďurech & J. Hanuš 2023; see their Figure 4). These orientations maximize Yarkovsky drift rates. Bennu, Ryugu, and Itokawa all have obliquities near 180°, with values of $\delta = 177\overset{\circ}{.}6$, $\delta = 171\overset{\circ}{.}64$, and $\delta \simeq 172°$, respectively (D. Vokrouhlický et al. 2004; H. Demura et al. 2006; D. S. Lauretta et al. 2019; S. Sugita et al. 2019; S. Watanabe et al. 2019). Our interpretation is the that precursors of all three worlds were moving inward toward the Sun when they escaped the main belt (W. F. Bottke et al. 2015b; K. J. Walsh et al. 2024).

The inward drift of Bennu, Ryugu, Itokawa, and their precursor bodies allowed them to migrate into gravitational resonances that drove them onto orbits that approach Earth's path. As will be discussed below, these objects were likely driven out of the main belt through the ν_6 secular resonance that defines the innermost boundary of the inner main belt, but plausible pathways also exist for smaller resonances in the inner main belt.

2.2. Dynamical Evolution of Bennu, Ryugu, and Itokawa

2.2.1. Likely Source Regions

As discussed in the Pachinko game analogy in the previous section, we will never know the exact dynamical pathways taken by Bennu, Ryugu, and Itokawa to get to their observed orbits. Still, much can be gleaned from an analysis of possible pathways for these bodies. As discussed in the previous section, the link between the Flora family and Itokawa is arguably well established, so we will focus here on Bennu and Ryugu.

The probable routes taken by Bennu and Ryugu to reach their current orbits were numerically simulated by W. F. Bottke et al. (2015b). They tracked the dynamical evolution of main-belt asteroids from three of the primary NEA source regions defined by W. F. Bottke et al. (2002): the ν_6 resonance, the 3:1 mean motion resonance with Jupiter (i.e., J3:1 resonance), and the intermediate-source Mars-crossing (IMC) region.

For the ν_6 resonance, they identified all bodies (known at that time) with absolute magnitude $H < 18$ that resided within 0.05 au of the antisunward side of the resonance boundary. They added the further criterion that none were on Mars-crossing orbits (assumed here to be perihelion $q > 1.66$ au). All these bodies had inclination $i < 17°$ (see Figure 1 in W. F. Bottke et al. 2015b). This gave them a starting set of 6396 main-belt asteroids. At the inclinations of Eulalia and New Polana, the ν_6 resonance escape zone is near 2.15–2.2 au (W. F. Bottke et al. 2002).

Next, using the symplectic *N*-body code SWIFT-RMVS3 (H. F. Levison & M. J. Duncan 1994), modified to accommodate Yarkovsky thermal forces (D. Vokrouhlický & D. Nesvorný 2008), they assigned the test bodies inward drift rates of $da/dt = 2.5 \times 10^{-3}$ au Myr^{-1} and 2.5×10^{-4} au Myr^{-1}. These values bracketed the plausible Yarkovsky drift values of Bennu and Ryugu in the main belt near 2.2 au. Additional details can be found in W. F. Bottke et al. (2015b).

When objects enter the ν_6 resonance, they are driven to larger eccentricities and planet-crossing orbits. From there, they can be removed from resonance by an encounter with one of the terrestrial planets (most commonly Earth). This will cause the asteroids to wander in semimajor axis a, eccentricity e, and inclination i space in response to gravitational interactions with the planets. Objects become defined as NEAs after they reach perihelion distance $q \leqslant 1.3$ au. We will provide more specific information on this evolution in the upcoming sections.

Most NEAs have dynamical lifetimes of a few million to a few tens of millions of years (e.g., W. F. Bottke et al. 2002; M. Granvik et al. 2018; D. Nesvorný et al. 2023). The most common ways for them to be eliminated are by hitting the Sun or by being thrown out of the inner solar system by a close encounter with Jupiter. Only a small fraction (∼1%) collide with a terrestrial planet.

For the test asteroids that enter into NEA space, W. F. Bottke et al. (2015b) ran checks to see which ones passed close to the current orbits of Bennu and Ryugu, namely semimajor axis, eccentricity, and inclination (a, e, i) values of (1.126 au, 0.204, 6°.035) and (1.190 au, 0.1902, 5°.884), respectively. A similar procedure was followed in this paper for Itokawa, which has a current (a, e, i) orbit of (1.324 au, 0.280, 1°.621), respectively. A match was defined when any test asteroid simultaneously passed within $\Delta a = 0.01$ au, $\Delta e = 0.01$, and $\Delta i = 1°$ of these values.

This gave us a subset of 42 test pathways for Bennu, 44 pathways for Ryugu, and 30 pathways for Itokawa. The best Bennu, Ryugu, and Itokawa matches came from main-belt test asteroids that had starting semimajor-axis values between 2.1 and 2.2 au, starting inclination values between 3° and 4°, and starting eccentricities between 0.1 and 0.2. The favored starting parameters for Bennu and Ryugu are broadly consistent with two probable source families for these two objects, namely Eulalia and New Polana (K. J. Walsh et al. 2013; W. F. Bottke et al. 2015b), while those for Itokawa are consistent with the dynamical spread of the Flora family (D. Vokrouhlický et al. 2017).

For the IMC region, W. F. Bottke et al. (2015b) examined asteroids in the inner main belt with orbital parameters of 2.1 au $< a <$ 2.5 au, 1.3 au $< q <$ 1.7 au, $i \leqslant 40°$, and $H \leqslant 18$. These criteria yielded 7918 objects (see Figure 2 in W. F. Bottke et al. 2015b). Here the test asteroids were assumed to have inward/outward drift rates of $da/dt = \pm 2.5 \times 10^{-3}$ au Myr^{-1} and $\pm 2.5 \times 10^{-4}$ au Myr^{-1}. All bodies were then sifted to determine which ones reached Bennu, Ryugu, and Itokawa orbits. This procedure provided us with 32 test pathways for Bennu, 31 pathways for Ryugu, and 19 pathways for Itokawa.

Finally, for the J3:1 resonance, we tracked 4092 objects with $H \leqslant 18$ within 0.05 au of both sides of the resonance that had $i < 27°$. Those on the inner side of the resonance were given positive drift rates of $da/dt = 2.5 \times 10^{-3}$ au Myr^{-1} and 2.5×10^{-4} au Myr^{-1}, while those on the outer side were given the opposite. Overall, we found one test pathway for Bennu, two pathways for Ryugu, and none for Itokawa.

Numerical simulations indicate that the ν_6 resonance is four times more likely to produce Bennu, Ryugu, and Itokawa than the IMC region (W. F. Bottke et al. 2002). The J3:1 was deemed an unlikely source for either Bennu and Ryugu, partly because few test bodies from that resonance reached their observed orbits, but also because their likely parent families, the New Polana and Eulalia families, are located sunward of the inner 3:1 resonance boundary. As discussed in K. J. Walsh et al. (2013) and W. F. Bottke et al. (2015b), Bennu and Ryugu would have had to reach the 3:1 resonance by drifting away from the Sun, which in turn would have required them to have obliquities $>0°$. These values are not observed.

Still, the dynamical evolution of IMC and J3:1 test bodies, once they get into the NEA region, is not appreciably different from those coming out of the ν_6 resonance. The primary difference is that the majority reach suitable starting orbits with modestly larger semimajor-axis values (i.e., 2.2 au $< a <$ 2.5 au) and $i < 7°$. For this reason, to increase our statistics in our modeling work below, we will use all the above test asteroid runs above that match Bennu, Ryugu, and Itokawa (i.e., 75, 77, and 49, respectively).

2.2.2. Orbital Evolution

The orbital histories of test bodies reaching Bennu, Ryugu, and Itokawa share qualitatively similar behavior in how they evolve in semimajor axis, eccentricity, and inclination. To display this behavior, we have discretized the space using

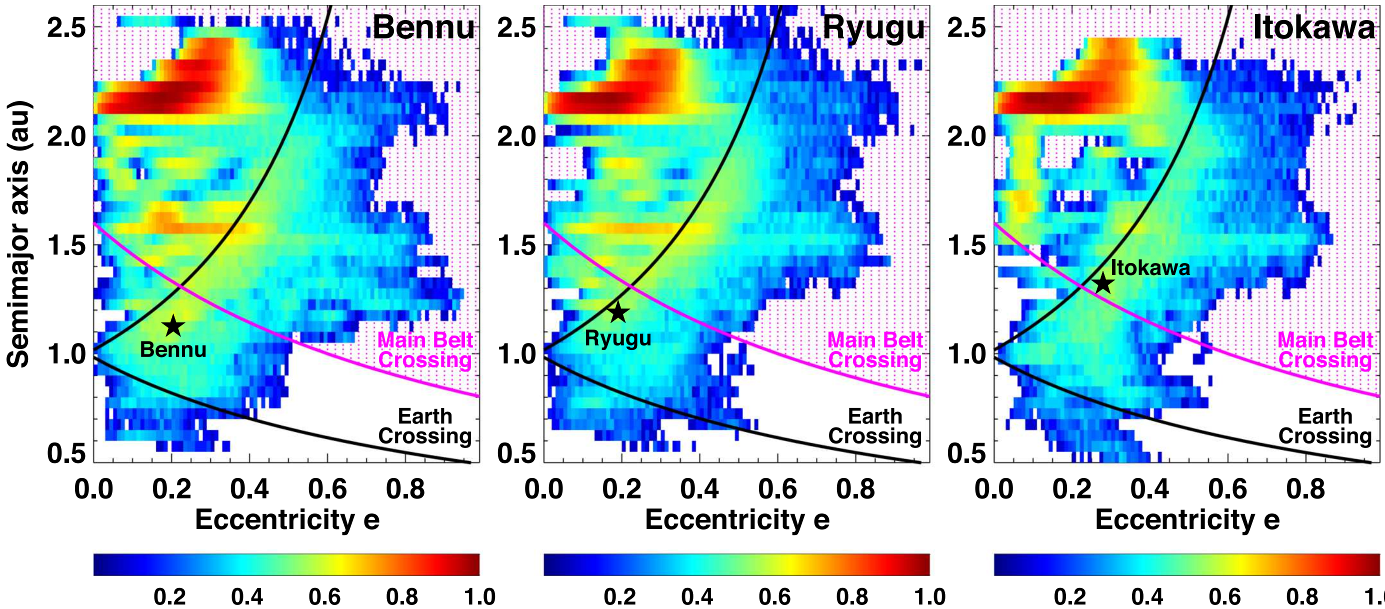

Figure 2. Residence time probability distributions for test asteroids from the main belt reaching the orbits of Bennu, Ryugu, and Itokawa. Earth-crossing asteroids have orbits between the black lines, while objects that can be hit by main-belt asteroids are above the magenta line. After sifting many tens of thousands of test asteroid pathways from W. F. Bottke et al. (2015b), 75, 77, and 49 were found to pass within $\Delta a = 0.01$ au, $\Delta e = 0.01$, and $\Delta i = 1°$ of the (*a, e, i*) values of Bennu (1.126 au, 0.204, 6°035), Ryugu (1.190 au, 0.1902, 5°884), and Itokawa (1.324 au, 0.280, 1°621), respectively (black stars). Most test asteroids were started in or near the dark-red colors (upper left corner). From there, they were driven to Earth-crossing orbits, where Earth encounters often remove them from resonance. Subsequent Earth encounters cause them to walk down lines of constant Tisserand invariant, located near the Earth-crossing line, to low (*e, a*) orbits. Additional spread in (*e, i*) is caused by interactions with resonances. The (*a, e, i*) orbits of the test asteroids were reported every 10,000 yr, with the values added up in a series of (*a, e, i*) bins. The objects were then removed after matching the orbits of Bennu, Ryugu, or Itokawa. For the colors, we summed the values over all inclination bins, took the logarithm, and normalized the distribution by the largest bin value. This sets the top of the scale bar to 1.

these elements, tracking each time a test asteroid enters an (*a, e, i*) bin. Here we use bin sizes that are $0\ \text{au} \leqslant a < 4.0$ au with $\Delta a = 0.05$ au, $0 \leqslant e < 1.0$ with $\Delta e = 0.01$, and $0° \leqslant i < 90°$ with $\Delta i = 5°$. The time spent in each bin is summed, with the results normalized by the (*a, e, i*) bin with the peak time value. These kinds of results are frequently called residence time probability distributions (e.g., W. F. Bottke et al. 2002; M. Granvik et al. 2016; D. Nesvorný et al. 2023).

Bennu's simulated trajectories are shown in Figure 2. They provide a measure of the number of times each orbit passes through a given bin in (*e, a*) space, with inclination results from all values folded into the plotted values. They follow a common pattern. Starting in the main belt, the asteroids enter an escape resonance and have their eccentricities increased to Earth-crossing values or beyond. For bodies in the ν_6 resonance, they will then oscillate in eccentricity over a wide range of values. In fact, on occasion, some trajectories will even pass close to the Sun for a limited time. Eventually, though, the test Bennus are removed from resonance, usually by an Earth encounter. From there, they migrate along the Earth-crossing line, which lowers their semimajor-axis and eccentricity values. In doing so, the test Bennus are trying to follow lines of constant Tisserand invariant with Earth (e.g., R. Greenberg & M. C. Nolan 1993).

The orbital evolution of the test Bennus is also affected by various smaller resonances with $a < 2$ au, which can move their eccentricities away from the Earth-crossing line. This prevents the evolution of NEAs from being entirely dominated by Earth encounters. These resonances also affect the inclination evolution of the test Bennus. While all of them start in the main belt with low inclinations, their inclination distribution becomes more dispersed as they evolve into NEA space. By definition, though, the inclination of our test Bennus must pass through Bennu's (*a, e, i*) orbit of (1.126 au, 0.204, 6°035).

The same general behavior is shown for Ryugu and Itokawa (Figure 2), which is not a surprise given that observed (*a, e, i*) values of Bennu, Ryugu, and Itokawa are similar to one another. As before, the orbital histories of most of these test asteroids follow the Earth-crossing line down to lower (*a, e*) values, with some variability produced by resonances in the inner solar system.

The timescale for our test asteroids to dynamically evolve from the main belt to the observed orbits of Bennu, Ryugu, and Itokawa is contingent on their starting orbits in the main belt. Unfortunately, there is no known way to determine when they became NEAs (e.g., Y. Cho et al. 2021). The NEA boundary of $q \leqslant 1.3$ au is arbitrary, and many near-Earth objects and Earth-crossers have orbits that allow them to be hit by main-belt projectiles.

A potentially more interesting timescale is the interval for Bennu, Ryugu, and Itokawa to go from an Earth-crossing orbit for the first time (i.e., perihelion $q \leqslant 1$ au) to their observed (*a, e, i*) orbits. For ease of use, we will define these values using the variable t_{transit}. Earth-crossing bodies can potentially have close encounters with Earth, which in some cases may lead to resurfacing events via tidal disruption (D. C. Richardson et al. 1998).

Using our test Bennu, Ryugu, and Itokawa values discussed above, we find that t_{transit} for Bennu, Ryugu, and Itokawa are generally <10 Myr, with median ages of 7.6, 5.7, and 6.0 Myr, respectively. We show these values in Figure 3. A few runs have t_{transit} of many tens of Myr or more, corresponding to NEAs that spend considerable time on low semimajor-axis orbits. These bodies have few ways to be eliminated, other than hitting a terrestrial planet or migrating back out to

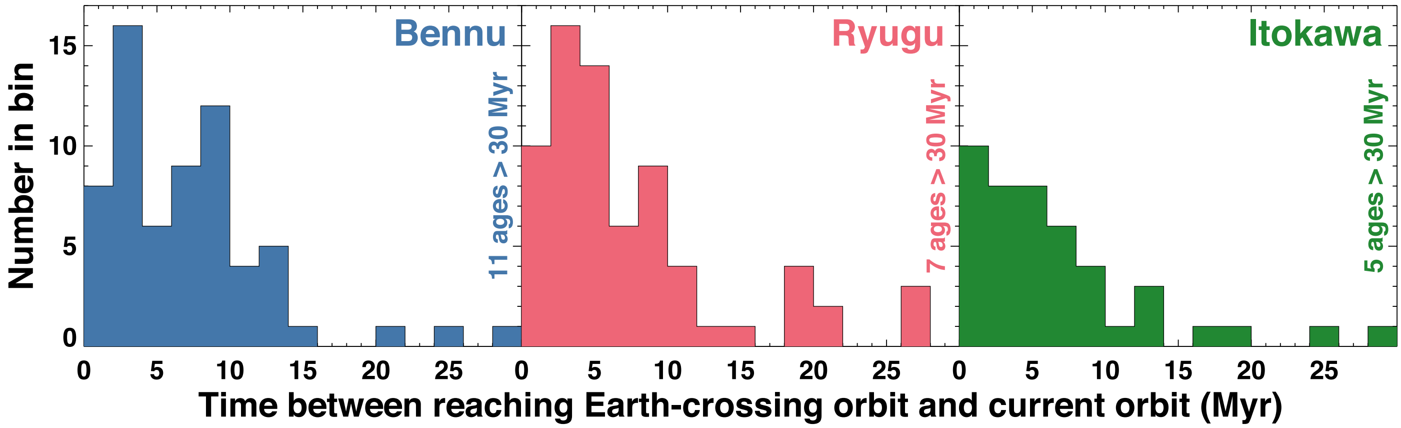

Figure 3. The elapsed time from when the 75, 77, and 49 test asteroids discussed in Figure 2 went from an Earth-crossing orbit to the orbits of Bennu, Ryugu, and Itokawa. This time is referred to as t_{transit}. The median t_{transit} times are 7.6, 5.7, and 6.0 Myr, respectively, for the three sample-return asteroids.

$a > 2$ au, so they tend to survive much longer than typical NEAs.

2.3. Surface Reset Timescales from Impacts

As small bodies cross the main belt, they can be hit by other asteroids. If the collisions are large enough, they will potentially disrupt them and/or erase their surface histories (e.g., R. Greenberg et al. 1994, 1996). We suspect that this has taken place for Bennu, Ryugu, and Itokawa.

For the moment, let us consider Bennu and Ryugu. If both started near their suspected parent families of Eulalia or New Polana, which reside near 2.4 au, and they escaped out of the ν_6 resonance near 2.2 au, as suggested by their current orbits (K. J. Walsh et al. 2013, 2024; W. F. Bottke et al. 2015b), they would need to have traveled at least 0.2 au across the main belt. Note that this value is probably an overestimate because the real distance is dependent on the ejection velocity of their precursor body from the family-forming event. Their Yarkovsky drift rates in the main belt are on the order of 4×10^{-4} au Myr^{-1} and 2.5×10^{-4} au Myr^{-1}, respectively (W. F. Bottke et al. 2006b; D. Vokrouhlický et al. 2015), while their mean collisional lifetimes should be on the order of ∼100 Myr and a few hundreds of Myr, respectively (W. F. Bottke et al. 2020). Put together, these values are such that none are likely to travel all the way from their source family/families to the ν_6 resonance without disrupting a few times. Sophisticated numerical simulations have helped to verify this scenario (K. J. Walsh et al. 2024).

Between disruption events, Bennu, Ryugu, Itokawa, or their precursor bodies are also likely to experience global resurfacing events from subcatastrophic impacts. The projectile size needed to produce a surface reset event has yet to be quantified with models or observational data, but it is probably smaller than the size needed for a disruptive collision. Accordingly, this means that impact-derived surface reset events for Bennu, Ryugu, and Itokawa are more frequent than disruption events.

For subkilometer bodies, the projectile size needed to disrupt the target should be smaller than 100 m in diameter, while the SFD of sub–100 m objects in the main belt follows a cumulative power law with a slope $q = -2.7$ (W. F. Bottke et al. 2020). Here we assume that the projectile size needed to disrupt the target is d_{disrupt}, while the size needed to reset the surface is $d_{\mathrm{reset}} = \varphi d_{\mathrm{disrupt}}$, with φ being between 0 and 1. We are interested in the difference between (i) the cumulative number of objects that produce reset events and (ii) the cumulative number of objects that produce disruption events. We want to exclude the latter. If both follow the same power-law SFD, surface reset events should occur $\sim\varphi^{-q} - 1$ or, for our case, $\varphi^{-2.7} - 1$ times more frequently than disruption events.

According to this relationship, φ values of 0.66 will double the reset rate, while $\varphi = 0.5$ will increase this rate by a factor of 5.5. If we assume that Bennu's and Ryugu's mean lifetimes against disruption in the main belt were 100 and 250 Myr, respectively (W. F. Bottke et al. 2020), while their surface ages were only ∼10 Myr old, the size of object needed to cause a global resurfacing event by impact on each would need to be $\varphi \sim 0.41$ and 0.30, respectively. If the surface ages were 5 Myr, the values would have to be even lower (∼0.32 and ∼0.23, respectively).

At this time, we have no idea whether such small projectiles can plausibly produce global resurfacing events. It might be possible to scale from the largest, oldest craters on Bennu, Ryugu, and Itokawa, but each world has several that are comparable in size. This suggests that the formation of one such crater was insufficient to erase another large crater. Numerical simulations of such impacts on these worlds would be needed to assess what such impacts can do to the surface of each body. We will return to the issue of impact-derived reset events in later sections.

2.4. Surface Reset Timescales from YORP

Another way to produce a surface reset event is YORP spin-up. Here thermal torques allow asteroids to achieve such fast spins that considerable material is driven off the body near the equator in a manner analogous to a landslide. Such behavior was inferred for Bennu from the mass movement patterns found there (E. R. Jawin et al. 2020). Free-floating debris produced by YORP spin-up will dynamically evolve into a disk of rubble around the primary, with some material escaping the system, some reaccreting with the primary, and some potentially forming into one or more small satellites. A short list of papers on this topic includes K. J. Walsh et al. (2008), D. J. Scheeres (2015), M. Hirabayashi et al. (2015, 2020), K. J. Graves et al. (2018), R. Hyodo & K. Sugiura (2022), and H. F. Agrusa et al. (2024). Reviews can be found in J.-L. Margot et al. (2015), K. J. Walsh & S. A. Jacobson (2015), and K. J. Walsh (2018).

The nature of these mass-shedding and potential surface reset events is contingent on the shape, strength, and surface structure of the asteroid, as well as the specifics of how the body rids itself of excess rotational angular momentum. In the most energetic cases, the cratered surface of the asteroid could potentially be erased, leaving behind a clean slate for new cratering. In more gentle cases, existing craters might survive. For example, the NEA binary (65803) Didymos and Dimorphos, which are 765 and 150 m in diameter, respectively, have crater SFDs that suggest that Dimorphos is younger than Didymos (S. Marchi et al. 2024). This would indicate that the YORP spin-up event on Didymos that created Dimorphos did not globally resurface Didymos. On the other hand, (152830) Dinkinesh and Selem, which are 720 and 220 m in diameter, respectively (H. F. Levison et al. 2024), have similar crater retention ages (within errors; S. Marchi et al. 2024). At this time, we cannot say which circumstance dominates evolution among small asteroids.

Another complicating issue is that the frequency of YORP spin-up reset events depends on multiple variables for each asteroid: its orbit, shape, spin state, surface and interior structure, composition, thermal properties, etc. This means that there is no "one size fits all" treatment for when such events occur on a generic asteroid, let alone the immediate precursors of Bennu, Ryugu, and Itokawa, whose parameters are unknown. In addition, it also appears that C-type asteroids are less likely to undergo YORP-driven mass-shedding events than S-type asteroids (Y. Zhang et al. 2022), as suggested by their lower abundance of satellites and asteroid pairs (K. Minker & B. Carry 2023; L. Liberato et al. 2024). We will return to this fascinating topic in the next section.

To glean insights into the issue, we will consider a simple zeroth-order scaling relationship for YORP spin-up timescales. Using the work in D. Čapek & D. Vokrouhlický (2004), who estimated YORP spin-up on a large sample of Gaussian spheres (i.e., mathematical potato-shaped objects), we can say the following. For a $D = 2$ km diameter body with heliocentric distance $d = 2.5$ au, bulk density $\rho = 2.5$ g cm^{-3}, spin period $P = 6$ hr, and plausible thermal conductivity values for such asteroids, the estimated asymptotic change in the rotation frequency ω, or spin rate, is $d\omega/dt \sim 3 \times 10^{-5}$ Myr^{-3} s^{-1}. The timescale for a generic asteroid to reach $P = 2$ hr, approximately the spin period needed to achieve mass shedding (e.g., K. J. Walsh & S. A. Jacobson 2015), is $\Delta\omega \sim 5.8 \times 10^{-4}$ s^{-1}. This criterion is achieved at time $T \sim \Delta\omega\ /\ (d\omega/dt) \sim 20$ Myr. Scaling to our input parameters, we get the relationship

$$T \sim 5\ \mathrm{Myr}(D/1\ \mathrm{km})^2(a/2.5\ \mathrm{au})^2(\rho/2.5\ \mathrm{g\ cm^{-3}}). \qquad (1)$$

We suspect that this timescale, drawn from generic initial conditions, is overly aggressive. Real asteroids undergo a slower initial phase before reaching the asymptotic branch where YORP is maximized. The reason for the slowdown may be stochastic YORP, a condition where small shape changes produced by impacts, minor landslides, boulder movement, etc., can lead to changes in the direction of the spin rate (T. S. Statler 2009; W. F. Bottke et al. 2015b). Objects may also rearrange their shapes in response to an increase in rotational angular momentum from YORP, which can in turn stretch the time needed to reach mass-shedding spin speeds (Y. Zhang et al. 2022). In addition, observations of YORP values for small asteroids indicate that top-shaped bodies are less susceptible to strong YORP spin-up than potato-shaped objects (i.e., many of the former are more spherical, while the latter tend to be more propeller-like; e.g., D. P. Rubincam 2000; W. F. Bottke et al. 2006b; D. Vokrouhlický et al. 2015).

Still, we would like to improve Equation (1). A key problem in doing so is that the YORP effect has been shown to depend on parameters that are largely inaccessible to ground-based observations (such as the small-scale surface topography, lateral conduction through boulders resting on the asteroid surface, etc.). This means that theoretical predictions of YORP spin-up rates will have large uncertainties.

In this situation, our best guide is the sample of asteroids where the YORP effect has been detected. Here we take advantage of the C_Y factor, which is a nondimensional coefficient that describes YORP strength for different asteroid shapes (B. Rozitis & S. F. Green 2013a, 2013b; see also A. Rossi et al. 2009). It normalizes the dependence of YORP over semimajor axis, eccentricity, diameter, and estimated density (though not obliquity).

In Table 1 of J. Ďurech et al. (2024), the C_Y factor is defined for different asteroids. The largest C_Y values, ∼0.015–0.025, are seen for (1862) Apollo, (1620) Geographos, and (10115) 1992 SK. In these cases, the simple YORP models that disregard small-scale topographic effects agree with the detected signal. For this reason, we adopt C_Y values of ∼0.01 as a reference level for YORP strength.

Several asteroids, like (1685) Toro, (3103) Eger, (54509) YORP, and (161989) Cacus, have C_Y values that are smaller than this reference level by a factor of 2–3. Of particular interest here, though, are those cases where C_Y values are even smaller, such as (101955) Bennu, top-shaped (138852) 2000 WN10, and (25143) Itokawa. For these bodies, C_Y is reduced by a factor of 8–20 compared to the reference level. We have yet to find any asteroids where C_Y is smaller than the reference level by a factor >25. We therefore conclude that available YORP detections support an attenuation factor between 2 and 20.

Taking values in the middle of this range, we favor increasing the timescales in Equation (1) by an approximate factor of 5–10, leading to

$$T \sim\ [25\text{–}50\ \mathrm{Myr}]\ (D/1\ \mathrm{km})^2\ (a/2.5\ \mathrm{au})^2\ (\rho/2.5\ \mathrm{g\ cm^{-3}}). \qquad (2)$$

These values are shown as the two blue curves in Figure 4. In the same plot, we also show as dashed lines what T would be for 12 different asteroids whose spin rates have been empirically determined from observations (J. Ďurech et al. 2024). These values were scaled over a range of diameters and under the assumption that each asteroid had a semimajor axis $a = 2$ au.

Overall, we find an order of magnitude in variation in T, which is driven by the enormous sensitivity in YORP to shape details and small-scale irregularities. Our interpretation is that Equation (2) should be taken as something of a median value. Note that asteroids with more symmetric shapes tend to have longer timescales than our blue curves, but boulders, craters, and other topographic features can modify this behavior.

Applying this equation to Bennu, if we assume that it has a diameter $D = 0.5$ km, bulk density $\rho = 1.2$ g cm^{-3}, and semimajor axis $a = 1.13$ au, we find that YORP spin-up timescales range between 0.7 and 1.3 Myr. These values compare reasonably well but are a little lower than the observed value of T for YORP spin-up, namely $T_{\mathrm{OBS}} \sim \Delta\omega/(d\omega/dt) \sim 1.52$ Myr, with about 15% uncertainty (C. W. Hergenrother et al. 2019).

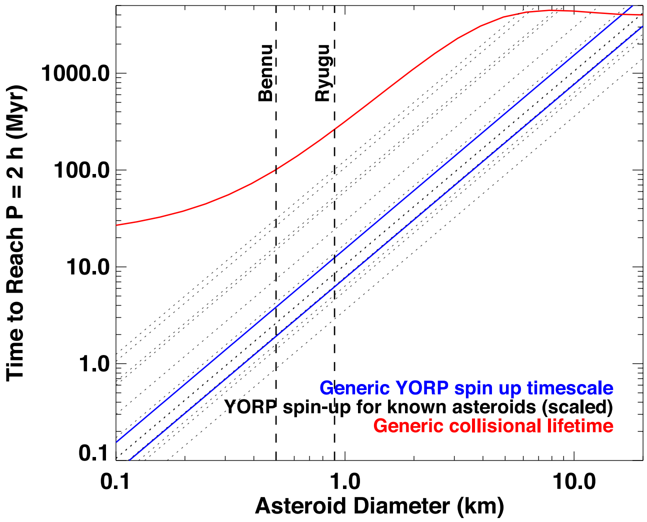

Figure 4. A comparison of collisional disruption timescales against YORP mass-shedding timescales for objects at $a = 2$ au. The red curve shows the average collisional lifetime of all main-belt objects from W. F. Bottke et al. (2020). The blue curves show the estimated timescale for asteroids to spin up from $P = 6$ hr to 2 hr by the YORP effect, according to Equation (2). The bulk density used in Equation (2) was 1.2 g cm^{-3}, similar to that of Bennu and Ryugu. Itokawa (not shown) has a bulk density of 1.9 g cm^{-3}, so the curves for those values should be scaled up by a factor of 1.6. For reference, the dashed lines show the predicted YORP spin-up timescales for 12 different asteroids whose shape and current YORP spin rates are known (J. Ďurech et al. 2024). Shape irregularities lead to a large spread in possible values, such that blue curves should only be considered approximations.

The current values of Bennu's $T_{\rm OBS}$, however, may be considerably shorter than its past values. For example, when Bennu first reached an Earth-crossing orbit, its representative semimajor axis was close to ∼2 au, which would in turn push T to timescales of 2–4 Myr. Using Bennu's real shape at this moment, we would perhaps push the upper bound to ∼5 Myr.

Similar calculations can be performed for Ryugu and Itokawa. Assuming that Ryugu has a diameter $D = 1$ km, bulk density $\rho = 1.2$ g cm^{-3}, and semimajor axis $a = 1.19$ au, the YORP spin-up timescale is $T \sim 3$–5 Myr. Moving Ryugu's representative semimajor axis to $a = 2$ au increases this value to 8–15 Myr. Here the timescales are longer because Ryugu is twice the size of Bennu. For Itokawa, assuming a semimajor axis of 2 au, diameter $D = 0.3$ km, bulk density $\rho = 1.9$ g cm^{-3}, and current semimajor axis $a = 1.3$ au, we find that its characteristic YORP spin-up timescale T should be ∼1.1–2.2 Myr.

These ages potentially provide us with insights into what might be expected for the crater retention age of Bennu, Ryugu, and Itokawa. On the other hand, it is not clear whether these timescales correspond to a gentle mass-shedding event or a global surface reset event. We will return to this topic when discussing results.

2.5. Surface Reset Timescales from Tidal Disruption

In recent years, tidal disruption has become the forgotten NEA resurfacing mechanism. Before YORP was discovered, it was considered to be the primary mechanism for making NEA binaries (e.g., W. F. Bottke et al. 1996; D. C. Richardson et al. 1998). The idea was that NEAs undergoing hyperbolic flybys near or within the Roche limit of Earth or Venus might undergo sufficient distortion and spin-up from tidal forces that they would shed mass. Numerical simulations showed that modestly common end states for these encounters would be small bodies orbiting what was left of the progenitor.

This perception changed, however, when it was recognized that the YORP spin-up mechanism was highly effective at producing mass-shedding events and satellites among small asteroids (e.g., K. J. Walsh et al. 2008; for a review, see K. J. Walsh & S. A. Jacobson 2015). YORP is effective for orbits across the inner solar system and as such can explain binary asteroids within the main-belt and NEA populations (e.g., Dinkinesh and Selam; H. F. Levison et al. 2024). Additional studies have shown that tidal forces are much better at stripping satellites from binaries than making them (A. Morbidelli et al. 2006; K. J. Walsh & D. C. Richardson 2006, 2008; A. J. Meyer & D. J. Scheeres 2021). As a consequence, tidal disruption studies became something of a sleepy backwater for most small-body researchers.

It may be time for a correction, with tidal forces thought responsible for several NEA observables. For example, consider that tidal forces probably stretched (1620) Geographos, an S-type NEA with dimensions of 5.0 × 2.0 × 2.1 km (R. S. Hudson & S. J. Ostro 1999), into its highly elongated shape, with a single convex side, tapered ends, and small protuberances swept back against the rotation direction (W. F. Bottke et al. 1999). This gives Geographos the appearance of a spinning pinwheel in space. Another example would be the plethora of Q-type NEAs residing near the Earth-crossing line. These objects, prone to be disturbed by tidal forces, have spectral signatures consistent with freshly exposed non-space-weathered ordinary chondrites (R. P. Binzel et al. 2010; D. Nesvorný et al. 2010).

The most exciting example, however, may originate from modeling work of the NEA population by M. Granvik & K. J. Walsh (2024) and D. Nesvorný et al. (2024a). Using nearly a decade of NEA detections from the Catalina Sky Survey as constraints, they found a distinct population of small bodies at low (a, e, i) orbits associated with the crossing orbits of Earth and Venus. Both deemed it unlikely that these bodies come from traditional NEA sources, such as the main belt or scattered disk. In D. Nesvorný et al. (2024a), the largest excess occurred for orbits between 1 au $< a < 1.6$ au, $q \simeq 1$ au, and $i \lesssim 10°$. We show their orbital distribution in Figure 5.

The small NEAs in this excess population have absolute magnitudes $25 < H < 28$. For reference, asteroids with C-type and S-type albedos of 0.04 and 0.20, respectively, correspond to asteroid diameters in the range of 17–66 m and 7–30 m, respectively. Note that the Catalina Sky Survey rarely sees asteroids with $H > 28$, so this excess population could potentially extend to even smaller sizes as well. Intriguingly, these objects reside exactly where one would expect to find them if they had formed by tidal disruption (e.g., W. F. Bottke et al. 1998; M. Granvik & K. J. Walsh 2024; D. Nesvorný et al. 2024a, 2024b). This would imply that the excess population is made up of rocks and boulders removed from the surfaces of many different NEAs.

We find that the preferred pathways for Bennu, Ryugu, and Itokawa to go from the main belt to their observed orbits pass through the (a, e, i) location of the excess population (Figures 2 and 5). This raises the possibility that tidal distortion or disruption may be an important yet unrecognized factor in the evolution of our three sample-return asteroids. We also suspect that the distances that Bennu, Ryugu, and Itokawa need to pass near Earth to undergo resurfacing events are

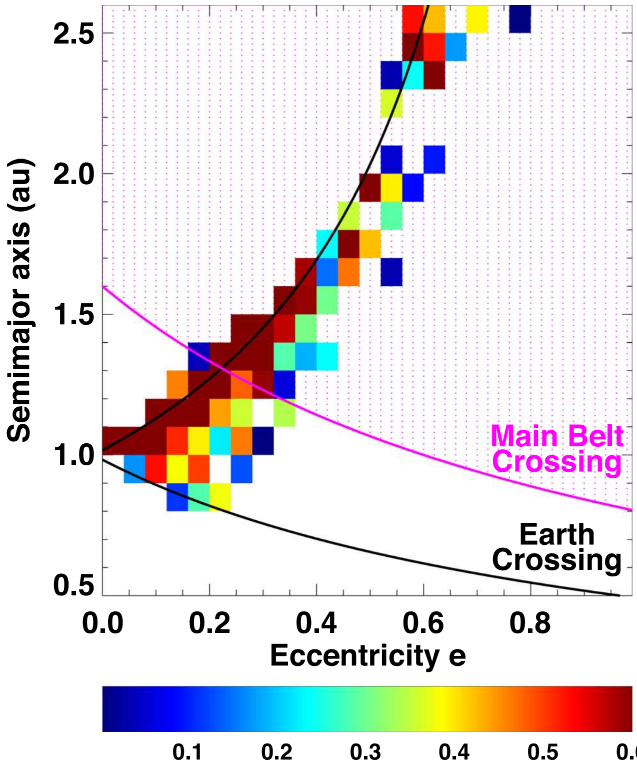

Figure 5. The residence time distribution of the excess population of small bodies relative to a base model of the NEA population (D. Nesvorný et al. 2024a, 2024b). The objects shown have absolute magnitudes $25 < H < 28$. The brown-red color shows the largest excess, with 1 au $< a < 1.6$ au, $q \simeq 1$ au, and $i \lesssim 10^\circ$. These orbits are consistent with their formation by tidal disruption among NEAs. The orbital locations of the excess population are similar to the orbits of Bennu, Ryugu, and Itokawa. This could suggest that these bodies have experienced close Earth encounters in the recent past, possibly enough to produce some degree of tidal resurfacing or perhaps even tidal disruption.

larger than those for tidal disruption events. If so, this would make the former more common than the latter, with the latter often requiring special conditions.

To get some feeling for whether tidal resurfacing is plausible, we have mapped the probabilities that our test asteroids have had close encounters with Earth in the past. We did this as follows. First, using the numerical integration runs discussed in W. F. Bottke et al. (2015b), we identified the (*a, e, i*) orbit of Earth at each output time step of our test asteroids for Bennu, Ryugu, and Itokawa, respectively (Figure 2).

Next, using the methodology of W. F. Bottke et al. (1994a), we calculated the intrinsic collision probabilities P_i between our target asteroids and Earth at each output time step. Here pairs of (*a, e, i*) orbits are used to calculate the likelihood that the two bodies will strike one another over all possible orbital orientations, defined by their longitudes of apsides and nodes, for a given unit of time and cross-sectional areas. This approximation is valid because secular perturbations randomize these values over relatively short ($\sim 10^4$ yr) timescales. Our code also includes gravitational focusing for Earth, which can be sizable because asteroids on Earth-like orbits have low encounter velocities with our planet.

Once P_i is computed, we multiplied this value by R_{Earth}^2 and the output time step of our numerical integration runs (10,000 yr). This yields the probability that the target asteroid would strike Earth. The probability values are binned in (*a, e, i*) in the same manner used to make Figure 2 (i.e., 0 au $\leqslant a < 4.0$ au with $\Delta a = 0.05$ au, $0 \leqslant e < 1.0$ with $\Delta e = 0.01$, and $0^\circ \leqslant i < 90^\circ$ with $\Delta i = 5^\circ$). For plotting purposes, we sum across the inclination bins for a given set of (*a, e*) values. The results are then normalized using the (*a, e*) bin with the top value. Our map of collision probabilities between our test asteroids for Bennu, Ryugu, and Itokawa and Earth is shown in Figure 6.

These probability maps show the (*a, e*) orbits where NEAs are most likely to have a close encounter or collision with Earth. The red contours are located close to the Earth-crossing line and reach their peak values for low (*a, e*) orbits. In addition, the excess NEA population in Figure 5 lines up with the red contours found in the Figure 6 maps. This match indicates that tidal disruption is indeed a likely candidate to make this population. Note that the gray circles in Figure 6 will be explained in Section 5.

The trends in Figure 6 show that as our model asteroids evolve closer to the current orbits of Bennu, Ryugu, and Itokawa, their encounter probabilities with Earth increase substantially. In dynamical evolution terms, these orbits are only a few Myr away or less from the current orbits of Bennu, Ryugu, and Itokawa. This result is not a surprise; as bodies take on orbits similar to that of Earth, their encounter probabilities must increase, especially when they find themselves on similar inclinations.

The next issue is to determine whether Bennu, Ryugu, or Itokawa experienced a past tidal resurfacing event. To glean insights into this problem, we calculated the net collision probability between our test asteroids and Earth. The results are shown in Figure 7. The curves show the impact probability for each test asteroid multiplied by distance from Earth's center squared. The *y*-axis shows the probability that a given test asteroid passed within this distance between the time it first reached an Earth-crossing orbit and its current orbit. The black line is the median probability for the ensemble of test asteroids.

We find that the median probability of Bennu, Ryugu, and Itokawa hitting Earth during their traverse from the main belt is less than 10%. From here, we can ask how close Bennu, Ryugu, and Itokawa need to pass near Earth to undergo a tidal resurfacing event. Unfortunately, there is currently no preferred answer to this question.

To probe this issue further, we considered the results of S. Sridhar & S. Tremaine (1992; see also E. Asphaug & W. Benz 1996). They estimated that the mass-shedding limit r_{disrupt} of a spherical nonrotating self-gravitating inviscid (i.e., zero viscosity) body approaching a planet on a parabolic orbit was

$$r_{\mathrm{disrupt}} = 0.69\, r_{\mathrm{roche}} = 1.69\, R_{\mathrm{pl}} \left(\frac{\rho_{\mathrm{pl}}}{\rho_{\mathrm{ast}}}\right)^{1/3}. \qquad (3)$$

Here R_{pl} and ρ_{pl} are the planet's radius and bulk density, while ρ_{ast} is the asteroid's bulk density. By setting ρ_{pl} for Earth to 5.513 g cm^{-3}, and ρ_{ast} of Bennu/Ryugu and Itokawa to 1.2 and 1.9 g cm^{-3}, respectively, the disruption distance becomes $2.8 R_{\mathrm{Earth}}$ and $2.4 R_{\mathrm{Earth}}$ from the center of Earth, respectively. Note that adding rotation to the body would modify this value, making it smaller or larger, depending on the orientation of the body's spin vector at perigee (D. C. Richardson et al. 1998).

Using these values, we find that the median probability that Bennu, Ryugu, and Itokawa had an encounter at these distances is 67%, 52%, and 30%, respectively. These are

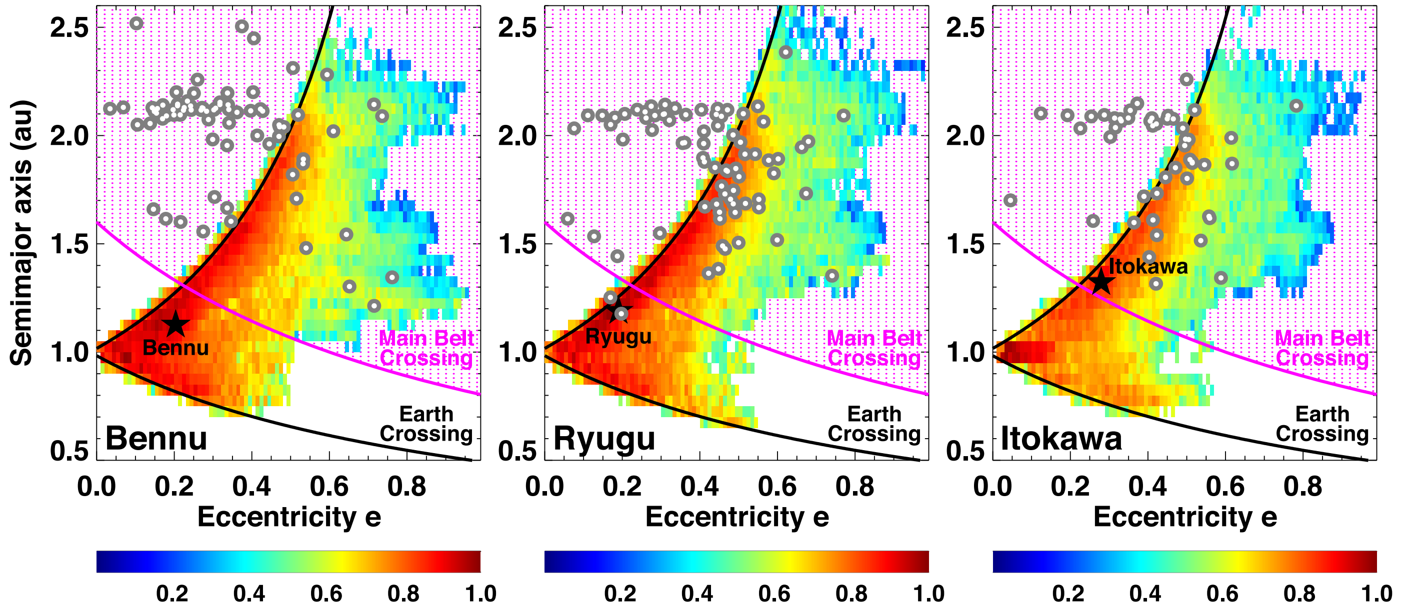

Figure 6. Map of the collision probabilities between test asteroids that reach the orbits of Bennu, Ryugu, and Itokawa and Earth. Our calculations used the orbital pathways discussed in the text and shown in Figure 2. Labels are discussed in Figure 2. At each 10,000 yr time step, the intrinsic collision probabilities between the (a, e, i) orbits of the test asteroids and Earth were calculated. The values were then added up within a series of (a, e, i) bins. For the colors, we summed the values over all inclination bins, took the logarithm, and normalized the distribution by the largest bin value. This sets the top of the scale bar to 1. This map is also a proxy for where objects are likely to undergo a close Earth encounter and possibly a tidal resurfacing event. The surface ages calculated from our crater production model allow us to predict where our test asteroids had their surfaces reset (gray circles). Those located near their starting orbits (high a and low e; see Figure 2) were most likely reset by impacts or YORP spin-up. For Bennu, few circles are found on or near the red contours, indicating that tidal resurfacing for this body is relatively unlikely. The odds are better for Ryugu and Itokawa, with many circles found on or near the red contours.

decent odds, enough that tidal resurfacing events require further discussion as a crater erasure mechanism in Section 5. The reason the probability for Itokawa is lower than that of Bennu and Ryugu is partly due to its higher density but also because its (a, e, i) orbit is modestly larger in semimajor axis and eccentricity (1.324 au, 0.280, 1°.621) than the other two worlds ((1.126 au, 0.204, 6°.035) and (1.190 au, 0.1902, 5°.884), respectively). This means that the encounter velocities are generally higher and the encounter probabilities are lower.

At this time, we cannot say whether the close-encounter distances in Equation (3) are sufficient to consistently produce tidal resurfacing. There are some reasons to think that they are not. For example, Y. Zhang et al. (2022) found that low-cohesion and low-friction structures often morph into more flattened shapes under the influence of YORP spin-up (or presumably Earth's tidal forces). In turn, this allows them to take on additional rotational angular momentum rather than lose it via mass shedding. Y. Zhang et al. (2022) argued that this type of behavior could explain the known geophysical characteristics of Bennu. It also provides a plausible solution for the curious paucity of moons among small C-type asteroids when compared to S-type asteroids (K. Minker & B. Carry 2023; L. Liberato et al. 2024).

It is similarly unclear whether Equation (3) is valid for all S-type asteroids, though some evidence is positive. For example, impact simulations of the DART spacecraft hitting Dimorphos indicate that Dimorphos is weak; its inferred cohesive strength is less than a few Pa, much like Ryugu and Bennu (S. D. Raducan et al. 2024). For Itokawa itself, we are not dealing with a top-shaped body but instead one with two large lobes and an elongated shape (Figure 1). This gives tidal forces a sizable lever arm that can be manipulated during a close encounter (D. C. Richardson et al. 1998). Moving the two lobes to new locations during such encounters would almost certainly erase craters.

There are other factors as well that affect whether tidal forces can produce a surface reset event. Numerical tidal disruption simulations from D. C. Richardson et al. (1998) indicate that elongated rubble-pile objects passing close to Earth (or Venus) can lose mass, but the outcome depends on the direction of their spin vector and long axis at encounter. Elongated objects whose long axis is approaching Earth at perigee can undergo mass shedding at $\sim 5R_{\rm Earth}$. Conversely, when the long axis is past Earth at perigee, the body can lose rotational angular momentum and become more spherical.

Objects whose spin vector is in the opposite direction of how tidal forces would like to spin them up can also lose rotational angular momentum during a close Earth encounter. In these cases, creating a binary asteroid is extremely unlikely, but reshaping the asteroid and possibly resetting surface features are possible. We suspect that reshaping a top-like asteroid may be difficult, though, without very close Earth encounters, given that these bodies lack a large lever arm that tidal forces can easily manipulate.

The bottom line is that studies of how tidal forces might globally resurface NEA topography are in their infancy. Until more work is done, the best we can do is make reasonable estimates and determine their probable effects. We will try to do so in the coming sections.

2.6. Synthesis

The takeaway massages from the sections above are as follows. First, while there is no way to know the exact path Bennu, Ryugu, and Itokawa took to their current orbit, dynamical modeling work suggests that they likely followed a common "orbital superhighway" for NEAs. Once they

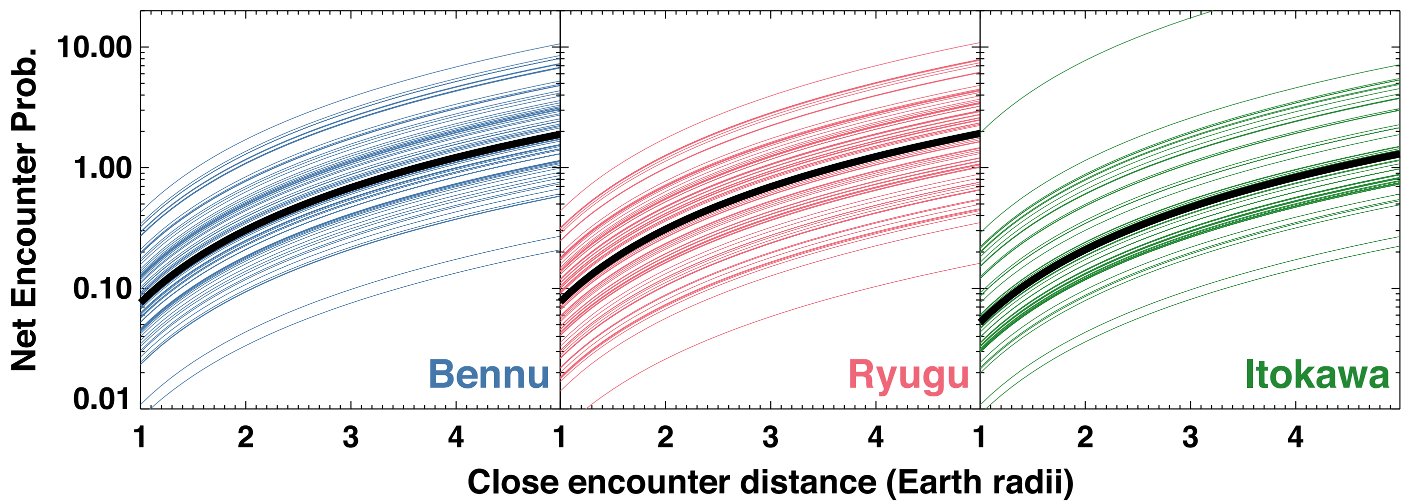

Figure 7. Net probability that our test asteroids for Bennu (blue), Ryugu (red), and Itokawa (green) have passed within a given close-encounter distance of Earth. See text and Figure 6 for calculation details. The black lines show the median net probability. The probabilities increase as distance from Earth's center squared. Each body has favorable odds (∼50% or more) of passing within ∼3 Earth radii over their lifetimes. The strongest likelihood is that these putative events took place near their current orbits, where close Earth encounters are probable (Figure 6). Few test asteroids, however, had their surfaces reset near those locations (gray circles in Figure 6). This indicates either that this distance is not close enough to consistently produce tidal resurfacing or that Bennu, Ryugu, and Itokawa avoided such close-encounter distances.

reached an Earth-crossing orbit, the objects started to migrate down the Earth-crossing line to lower semimajor axes and eccentricities values via Earth encounters (Figure 2). The timescale needed to follow this path was <10 Myr (Figure 3).

Second, as NEAs get lower semimajor-axis values, the frequency of YORP mass-shedding events becomes faster. As they then move to lower (*a, e*) values, the frequency of close Earth encounters increases as well (Figure 3). Given the abundance of small NEAs near the Earth-crossing line and at low (*a, e*) (Figure 5), Earth's tidal forces may well produce more mass shedding than YORP spin-up for NEAs on these orbits (e.g., W. F. Bottke et al. 1998; M. Granvik & K. J. Walsh 2024; D. Nesvorný et al. 2024a, 2024b). Accordingly, collisions, YORP, and tidal resurfacing of NEAs are all in play to explain crater resurfacing events on Bennu, Ryugu, and Itokawa.

Third, a key question for Bennu, Ryugu, and Itokawa is whether collisional resurfacing events, YORP spin-up, or tidal resurfacing events are most important for producing global crater erasure events. Given that we do not know the precise pathway taken by these bodies to their observed orbits, the best we can do is use our estimates of the surface ages of these bodies to glean insights into this question.

With these ideas in hand, we are now ready to model the crater SFDs found on Bennu, Ryugu, and Itokawa.

3. Crater Size Distributions for Bennu, Ryugu, and Itokawa

In this section, we briefly review the crater SFDs used in this paper for Bennu, Ryugu, and Itokawa.

3.1. Bennu

Airless bodies are subject to the impact of small particles and the solar wind. This has two main effects: (i) it can change the spectral appearance of surface material, a process often called space weathering, and (ii) it can cause small particles to be lost via electrostatic levitation and radiation pressure (C. M. Hartzell & D. J. Scheeres 2013; C. M. Hartzell 2019). The degree of weathering can be tracked through visible−near-infrared color imaging and spectral slopes, with changes giving us the relative ages of an asteroid's surface (S. Sugita et al. 2019; Y. Cho et al. 2021; D. N. DellaGiustina et al. 2020; E. B. Bierhaus et al. 2023). By obtaining the relative and potentially absolute ages of craters, we can glean insights into how fast crater erasure processes work with time, whether these processes are gradual or episodic, and how they might change with crater size.

Using spatially resolved color images (pixel scale ∼25 cm) taken from the OSIRIS-REx Camera Suite (OCAMS) and the multispectral MapCam imager, D. N. DellaGiustina et al. (2020) found that Bennu has space-weathering trends. For example, Bennu's midlatitudes are spectrally less weathered than the equator (i.e., they are younger). On Bennu, material generally wants to move toward the midlatitudes (E. R. Jawin et al. 2020; 2022), so these weathering trends match expectations for Bennu.

Using data from D. N. DellaGiustina et al. (2019) and K. J. Walsh et al. (2019), D. N. DellaGiustina et al. (2020) identified relationships between color and crater morphology for ∼700 craters. Recent updates can be found in E. B. Bierhaus et al. (2023). The crater SFDs of Bennu's oldest (blue) and youngest (magenta) craters are shown in Figure 8. The youngest were defined using space weathering as an age proxy (see D. N. DellaGiustina et al. 2020, for details). Many craters are redder than Bennu's global average color by $\geqslant 0.5\sigma$ in the near-UV to near-IR. Here σ is defined as the full width at half-maximum of the global distribution of spectral slopes in the available bands. These craters are generally small ($D_{\rm crater} \leqslant 25$ m) and are superposed on the bluish craters, with those on top being younger with more recently exposed materials. Conversely, the largest craters on Bennu ($D_{\rm crater} \geqslant 100$ m) were found to be indistinguishable from the space-weathered colors of the average terrain. Given that the largest craters are likely to be the oldest and the hardest to erase, this degree of space weathering was expected.

Put together, we can say that many small craters on Bennu are red/young, while most bigger craters are bluer/older.

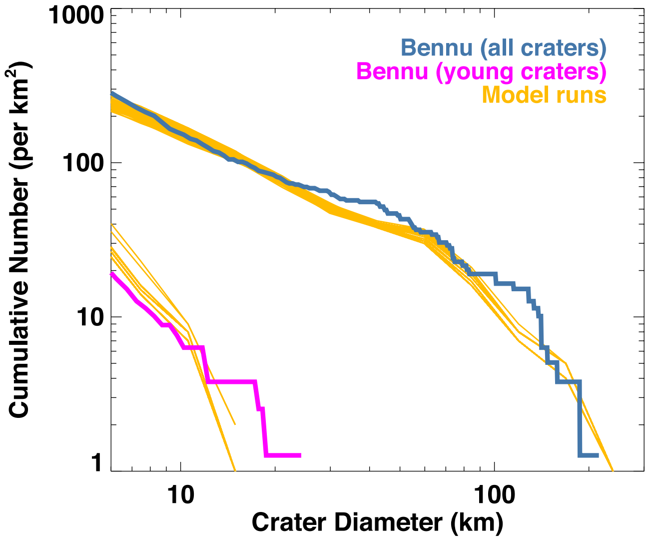

Figure 8. The crater SFDs for Bennu's craters. (a) The blue curve shows all craters identified by D. N. DellaGiustina et al. (2020), while the magenta curve shows craters more than 1σ redder than the average spectrum of Bennu. The gold curves show our model crater SFDs over 75 different orbital pathways (see Figure 2). Overall, we consider the fits between model and observations to be reasonable, but some features are missed, partly because our crater formation process is stochastic but also because our damage function is an imperfect tool for modeling crater erasure at small crater sizes.

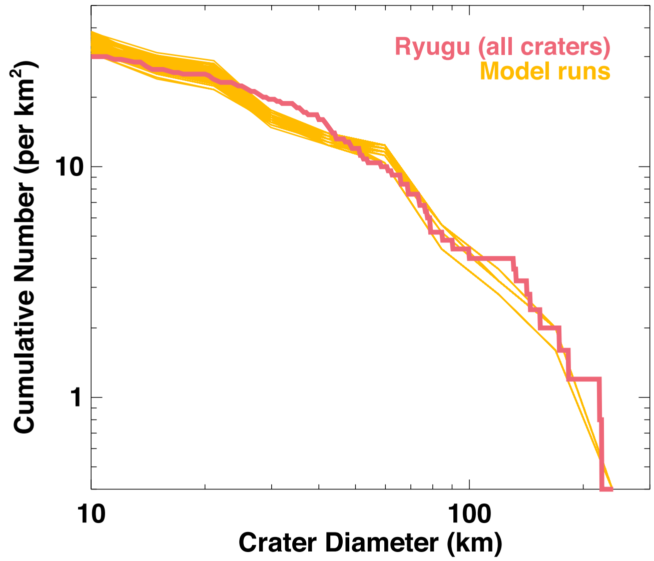

Figure 9. The crater SFDs for Ryugu's craters. (a) The red curve shows 77 craters identified by N. Hirata et al. (2021; see also T. Morota et al. 2020; Y. Cho et al. 2021). The gold curves show our model crater SFD over 77 different orbital pathways (see Figure 2). As with Figure 8, stochastic crater production and an imperfect crater damage function produce some minor mismatches between model and data.

Accordingly, blue and red colors on Bennu are a proxy for crater age. Here we will determine new model ages for the red/young and blue/old craters, which can then be compared to previous results (D. N. DellaGiustina et al. 2020; E. B. Bierhaus et al. 2023).

The SFD of young craters (magenta line) shown in Figure 8 is close to a cumulative power-law index of −2.7, consistent with the size distribution of small lunar and main-belt asteroid craters (W. F. Bottke et al. 2020). This indicates that the reddest craters may still be in production. Conversely, the size distribution of all craters shows a major change in slope at small crater sizes. This change could indicate that the crater SFD has undergone crater erasure processes (see Section 4 and Figures 15 and 16 in E. B. Bierhaus et al. 2023).

3.2. Ryugu

The craters used for our analysis of Ryugu come from N. Hirata et al. (2020), whose work builds on the initial report in S. Sugita et al. (2019). They examined the surface of Ryugu for craters over its surface area of ∼2.5 km^2. Craters were assumed to be circular or quasi-circular depressions, but many were also degraded and filled with regolith or boulders. This means that there is some ambiguity in their interpretation of a crater. To deal with this issue, the craters were classified by their morphology. The most clear-cut craters were defined as having a "circular depression with rim," while the most degraded were "quasi-circular features." The latter features were not considered craters. Moreover, due to spacecraft limitations, imaging on Ryugu was best at latitudes closer to the equator, which may bias crater identification. Given the image resolution of the spacecraft, they set a minimum diameter threshold of 20 m, though craters as small as 10 m were also reported.

All told, 77 craters were identified in the N. Hirata et al. (2020) data set. They are listed in their Table 3 and are shown in Figure 9. Three were larger than 200 m, with the largest being 290 m. Their spatial distribution is not uniform. The equatorial regions have more craters than the polar regions, while the meridian region has more craters than their western bulge. This difference may have been caused by regional resurfacing events on each hemisphere (Y. Cho et al. 2021). Y. Cho et al. (2021) also argue that the oldest feature on Ryugu is the ridge that lies near or on its equator. At some later time, the biggest crater formed on Ryugu, scattering material around the surface that possibly buried other nearby craters (via global jolt; R. Greenberg et al. 1994; 1996). Then, in more recent times, the large-scale movement of rocks and boulders in the western hemisphere erased some craters.

In this paper, we take the approach used by the Hayabusa2 team and will treat Ryugu's crater population as having formed in an isotropic manner across its entire surface. This will introduce some imprecision into our surface age results, given that the spatial density of craters varies from region to region, as discussed above. Given that the distribution of large craters is fairly uniform, however, mainly because they are less susceptible to crater erasure mechanisms, we do not expect this assumption to strongly affect our overall results in calculating Ryugu's surface age. It is beyond the scope of this paper to date all the distinct resurfacing events on Ryugu, though that could be done in future work.

Space weathering has also been observed on Ryugu and is discussed in T. Morota et al. (2020). Compositional differences and/or the physical structure of Ryugu's materials, however, cause it to work in the opposite direction compared to Bennu. On Ryugu, space weathering leads to the reddening of the surface, with the youngest features being more bluish. Overall, the equatorial regions of Ryugu tend to be older, while the higher-latitude regions are younger.

An alternative explanation for space weathering was also proposed by T. Morota et al. (2020). They suggested that Ryugu could have made a close passage to the Sun en route to its current orbit, which would heat up the surface enough to cause it to redden. From there, Ryugu would pull away from the Sun, with subsequent craters exposing fresh (and spectrally blue) materials in the subsurface. The authors point out, however, that this putative passage near the Sun is inconsistent with the abundance of hydrous minerals found on the surface among the reddish material. Material excavated by the Small Carry-on Impactor (SCI) experiment also shows no spectral color evidence that Ryugu passed close to the Sun in its past (K. Kitazato et al. 2021).

From a dynamical standpoint, we did find examples of test objects in the ν_6 resonance that are potentially comparable to the pathways suggested by T. Morota et al. (2020). Using the methods described in M. Delbo & P. Michel (2011), we found that some of our test asteroids reach eccentricities of ~0.9 and surface temperatures of 900°C before they recede from the Sun and find their way back to a Ryugu-like (*a, e, i*) orbit.

A possible issue for these orbital pathways being linked to Ryugu is that they are rare. Out of the ν_6 resonance test bodies that reach Ryugu-like orbits, we found that only 7% reach such extreme temperatures. If we were to assume that the temperature threshold needed to explain the space-weathering results in T. Morota et al. (2020) was only 600°C, we can increase the fraction of objects that reach those temperatures and Ryugu-like orbits to 16%. Doing so, however, still leaves another problem. The temperature thresholds discussed above are reached relatively early in the history of the Ryugu model asteroids, namely they are still in the ν_6 resonance. According to the dynamical framework discussed in Section 2, most of Ryugu's crater history is still to come, which would violate the T. Morota et al. (2020) constraints.

Overall, we consider space weathering to be a more viable scenario to explain the differences in Ryugu's spectra across its surface than sudden heating near the Sun. This is not to say, however, that such extreme heating events do not happen with other NEAs. Additional information on extreme solar heating of NEAs can be found in certain CM meteorites that have apparently experienced high heating events (e.g., E. Tonui et al. 2014; A. J. King et al. 2021). Moreover, if the temperatures become too high, the carbonaceous-chondrite-like objects may disrupt near the Sun (M. Granvik et al. 2016; D. Nesvorný et al. 2023).

3.2.1. Itokawa

The craters found on Itokawa come from the work of N. Hirata et al. (2009). They identified 38 candidate craters, with confidence in their craters labeled by numerical values between 1 (high confidence) and 4 (low confidence). Here we only use those craters designated with values of 1 or 2, which yields about 20 craters. Their crater SFD is shown in Figure 10.

Itokawa's surface has two main geologic units, one containing numerous boulders and the other with smooth terrains made up of numerous centimeter- and sub-centimeter-sized particles (J. Saito et al. 2006; H. Yano et al. 2006). No classical bowl-shaped craters were found on either unit. Instead, the craters seem to consist of vague circular features. In some cases, rocks and boulders were apparently shoved out of the way by an impacting asteroid. Such behavior was also seen on Bennu (e.g., E. R. Jawin et al. 2020). Detailed information on how Itokawa's craters experienced space weathering has yet to be published.

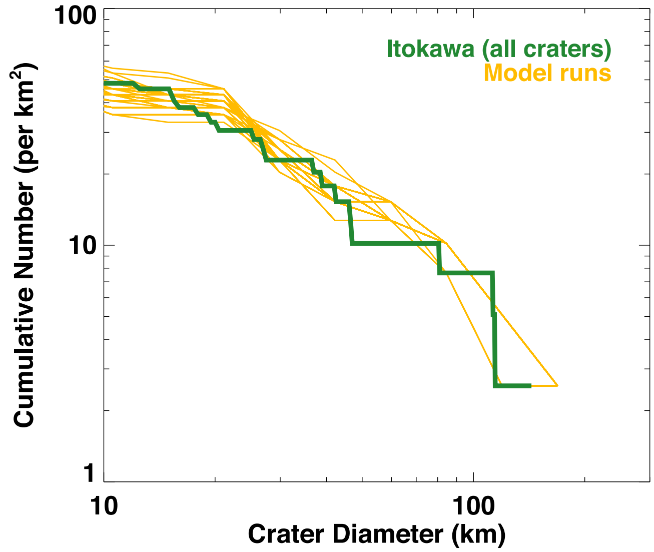

Figure 10. The crater SFD for Itokawa's craters. The green curve shows 20 craters from the work of N. Hirata et al. (2009). They were classified at confidence levels of 1 and 2 from a scale between 1 and 4. The gold curves show our model crater SFD over 49 different orbital pathways (see Figure 2). As with Figure 8, stochastic crater production and an imperfect crater damage function will create some minor mismatches between model and data.

4. Crater Production Model

We are now ready to discuss our crater production model NEA-EVOL. We start with an overview of how the code works, which will be followed by a description of its various components. The initial step in NEA-EVOL is to choose a target NEA, in this case Bennu, Ryugu, or Itokawa, as well as a probable orbital pathway from our preexisting model runs shown in Figure 2 (Section 2.2). Here an orbital pathway is defined by the body's (*a, e, i*) values at each output time step, with the time step set at 10,000 yr. Next, the code determines the impact flux on the target asteroid for each time step using a series of look-up tables in (*a, e, i*) space that include the collision probabilities, impact velocities, and SFDs for our three impactor populations: the main-belt, Mars-crossing, and NEA populations. These look-up tables are discussed in Section 4.1 and are calculated across a series of (*a, e, i*) bins prior to the start of our trial run.

At a given time step, NEA-EVOL calculates the combined impact flux for the target asteroid and turns it into a crater production model using crater scaling laws (Section 4.2). The craters formed within the time step are then saved as an output file for entry into the code CRASAT (Section 4.3). As will be discussed in more detail below, CRASAT uses this input, along with random deviates, to choose the size and location of each crater on the target body's surface formed during the time step. By modeling each crater individually, CRASAT can account for "cookie-cutter" crater erasure (i.e., craters can be partially or completely erased when another crater forms on top of them), crater erasure from sandblasting processes (i.e., the rims of large craters can be removed by small impacts), crater saturation processes, and additional crater erasure processes included by the user (Section 4.4). Craters from different model time steps are then combined into a single model crater SFD on the target asteroid at that time and orbit. This synthesis model SFD can be directly compared to the observed crater SFD on the target NEA (e.g., craters found by various mission teams for Bennu, Ryugu, and Itokawa).

The next several subsections describe the various NEA-EVOL model components in more detail (Sections 4.1–4.4).

4.1. Impacting Asteroid Populations

NEAs that depart the main asteroid belt are not yet safe from impacting asteroids. A large fraction of the NEAs have high enough eccentricities that they will continue to cross the main-belt population for an extended time (W. F. Bottke et al. 1994a, 1994b; 1996). Even when they reach orbits that are collisionally decoupled from most main-belt asteroids (approximately aphelion $Q < 1.6$ au; W. F. Bottke et al. 1996), they can still cross a population of Mars-crossing asteroids and NEAs, with many capable of hitting at speeds $>10\ \mathrm{km\ s^{-1}}$ (W. F. Bottke et al. 1996). These populations are considerably smaller than the main belt, but their impacts still contribute at a substantial level to the cratering record of long-lived NEAs on low semimajor-axis and eccentricity orbits, particularly if they have been resurfaced on such orbits.

At present, there is no crater production model that accounts for impacts from all three of these populations simultaneously on a dynamically evolving NEA. Instead, previous papers have generally adopted impact rate estimates for representative NEAs, with these bodies getting hit by other NEAs and/or main-belt asteroids (such as those impact rates developed in W. F. Bottke et al. 1994b; see, e.g., S. Sugita et al. 2019; K. J. Walsh et al. 2019; Y. Cho et al. 2021; E. B. Bierhaus et al. 2022; 2023). Some complicating issues in using this strategy are that (i) it is not easy to choose a representative NEA orbit (see Figures 2–4), (ii) the NEA impact rates on NEAs calculated in W. F. Bottke et al. (1994b) were developed when relatively little was known about the NEA population, and (iii) no group has yet considered crater production from Mars-crossing asteroids, which can affect some NEAs that are collisionally decoupled from the main belt.

For those reasons, NEA-EVOL calculates the combined impact flux and collision velocities for projectiles striking a target NEA on any $(a,\ e,\ i)$ orbit within the inner solar system. The projectiles striking our target come from our best estimates of the orbital and size distributions of the main-belt, Mars-crossing, and NEA populations. We discuss them in Sections 4.1.1–4.1.3.

Our procedure is as follows. First, we created a look-up table of intrinsic collision probabilities (P_{i}) and mean impact velocities (V_{imp}) between test bodies uniformly distributed in $(a,\ e,\ i)$ space and a representative orbital sample of objects from the main-belt, Mars-crossing, and NEA populations. The details of these populations will be given in the following subsections. We assumed that the test bodies in our look-up table were distributed across a grid of $(a,\ e,\ i)$ orbits across the inner solar system that covered all of the places where an asteroid might travel: $0.1\ \mathrm{au} \leqslant a < 3.0\ \mathrm{au}$ with $\Delta a = 0.1$ au, $0.0 \leqslant e < 1.0$ with $\Delta e = 0.1$, and $0° \leqslant i < 90°$ with $\Delta i = 3°$. By inserting these values into the collision probability code developed by W. F. Bottke et al. (1994a), we generated a look-up table of ($P_{i,\ \mathrm{pop}}$, $V_{\mathrm{imp,\ pop}}$) values for wherever our target NEA would go in $(a,\ e,\ i)$ space. Here "pop" is defined as the main-belt (mb), Mars-crossing (mc), or NEA population (NEA).

Next, we chose a suitable impactor SFD from each population. We define the cumulative number of model asteroids larger than a given size D_{ast} in each SFD as $N_{\text{pop-ast}}$ ($>D_{\text{pop-ast}}$), where "pop-ast" is one of the three populations under consideration. Accordingly, the number of model craters forming per square kilometer on the surface of the target body from the chosen population within time Δt is defined as $N_{\text{pop-crat}}$ ($>D_{\text{pop-crat}}$) and is given by the equation

$$N_{\mathrm{pop-crat}}(>D_{\mathrm{pop-crat}}) = \frac{P_{i,\mathrm{pop}}(a,\ e,\ i)\Delta t\, N_{\mathrm{pop-ast}}(>D_{\mathrm{pop-ast}})}{4\pi}. \tag{4}$$

The missing component here is the crater scaling law that transforms our projectiles $D_{\text{pop-ast}}$ into craters $D_{\text{pop-crat}}$ on our target body. This will be discussed in Section 4.2.

At every model time step Δt, we compute these values for all three populations and add them together to get our synthesis crater production model. These results are input into our crater code CRASAT. As the body evolves in $(a,\ e,\ i)$ over various time steps, new craters will be added to the target body. The result is a synthesis crater SFD that can be compared to the observed craters on the target body.

4.1.1. Main-belt Model

To produce the crater production model for target asteroids crossing the orbits of main-belt asteroids, our first task is to choose a representative sample of main-belt orbits. We refer the reader to the more lengthy discussion of this issue in Section 4 of W. F. Bottke et al. (2020). In that work, we argued that a reasonable statistical proxy for the orbital distribution of the main-belt population were the 682 asteroids with $D_{\mathrm{ast}} \geqslant 50$ km as defined by P. Farinella & D. R. Davis (1992) and used by W. F. Bottke et al. (1994a) (black circles in Figure 11(a)). This sample is imperfect, but it avoids certain complicating issues that come up when trying to use the Wide-field Infrared Survey Explorer diameter-limited catalog of main-belt objects, which is currently incomplete for some sizes (e.g., J. R. Masiero et al. 2011). As mentioned above, the collision probabilities and impact velocities are $P_{i,\ \mathrm{mb}}$ $(a,\ e,\ i)$ and $V_{\mathrm{imp,\ mb}}$ $(a,\ e,\ i)$, respectively.

Next, we selected a representative SFD for the main-belt population from the results of W. F. Bottke et al. (2020), who modeled the collisional evolution of the main-belt population. After considerable testing, they argued that their main-belt SFD #6 (see their Figure 1) did the best job of reproducing main-belt SFD and asteroid family constraints, while also reproducing the crater SFDs of spacecraft-observed asteroids with $D_{\mathrm{ast}} \geqslant 10$ km. These values define $N_{\text{mb-ast}}$ ($>D_{\text{mb-ast}}$) and are shown in Figure 12.

4.1.2. Mars-crossing Asteroid Model

The Mars-crossing (MC) population used in our model is defined as those bodies with perihelion $1.3\ \mathrm{au} < q < 1.66$ au and $a < 3$ au (Figure 12). These values were chosen to avoid double-counting; many MCs are also NEAs. We will treat the NEAs as a separate population below. This means that the MCs in our model are objects on solely Mars-crossing orbits with $q > 1.3$ au. The MCs have evolved out of the main belt via numerous small resonances, and many still reside in those resonances. As discussed by W. F. Bottke et al. (2002), the MCs are quasi-stable, and many take considerable time before they become NEAs.

Using the JPL Horizons database as of 2022, we found that there were 1104 MCs with absolute magnitude $H \leqslant 16$ that fit our dynamical definition and numerous bodies with $H > 16$.

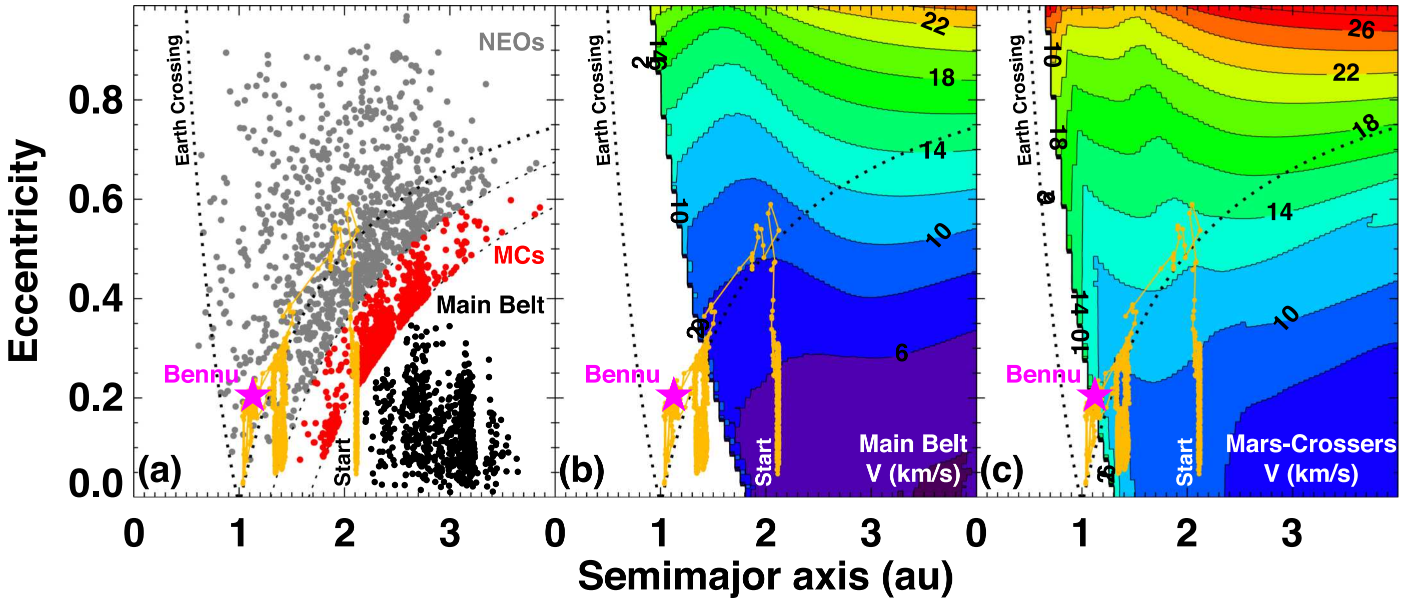

Figure 11. (a) One possible dynamical pathway for Bennu. The gold line shows how the test asteroid goes from the ν_6 resonance on the inner edge of the main belt to its current orbit (magenta star). Each gold circle is 0.01 Myr. Portions of main-belt (black), Mars-crossing (MCs; red), and NEA populations (gray) are shown for reference. The dashed lines between the gray/red and red/black circles show perihelion $q = 1.3$ and 1.66 au, respectively. Objects between the dotted lines are on Earth-crossing orbits. (b) Mean impact velocities for main-belt asteroids hitting test bodies with $i = 5°$. Bennu is hit until it reaches $a < 1.5$ au. (c) Same as panel (b), except MCs are used. MCs are 6 times the size of the NEA population and can strike Bennu on its current orbit (Figure 11).

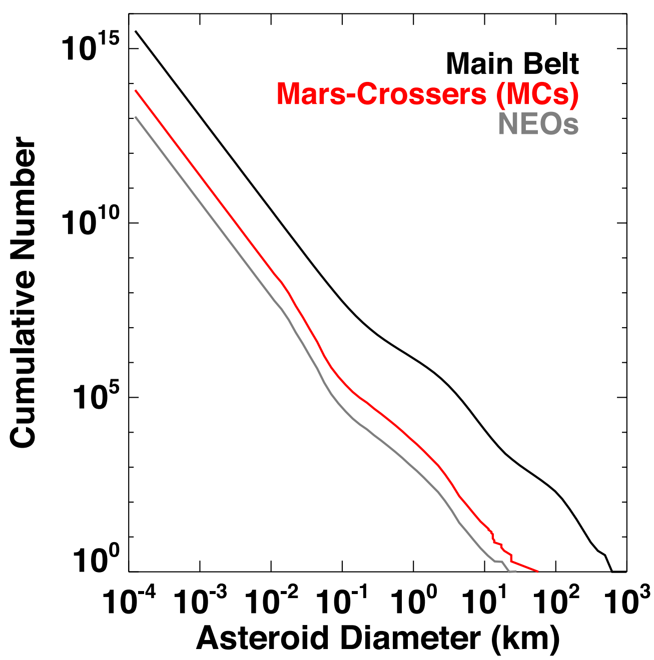

Figure 12. The estimated asteroid SFDs of the main-belt population (black), the asteroid population on solely Mars-crossing orbits with perihelion $q > 1.3$ au (red), and the NEA populations (i.e., $q < 1.3$ au; aphelion $Q > 0.983$ au; gray). The main-belt SFD was defined at SFD #6 in W. F. Bottke et al. (2020). The NEA SFD was defined by A. W. Harris & P. W. Chodas (2021). The Mars-crossing (MC) SFD was defined as being 6 times larger than the NEA SFD (see text for details). Impact rates on target asteroids are calculated from these SFDs after multiplying them by (i) the intrinsic collision probability found between representative members of each impactor population and the (a, e, i) orbital bin where the target asteroid is located and (ii) the cross-section area of the target asteroid.

By plotting the MCs against debiased estimates of the NEA absolute magnitude distribution (A. W. Harris & P. W. Chodas 2021; D. Nesvorný et al. 2023), we found that this population is essentially complete. We chose the $H \leqslant 16$ bodies as a statistical proxy for the orbital distribution of all MCs. They were used to calculate our look-up table of collision probabilities and impact velocities for the MCs, which are defined as $P_{i,\,\mathrm{mc}}\,(a, e, i)$ and $V_{\mathrm{imp,\,mc}}\,(a, e, i)$.

Using the same data set, we identified 189 objects with $H \leqslant 16$ that are NEAs (i.e., $q \leqslant 1.3$ au; red circles in Figure 11(a)). The ratio between the two populations for $H \leqslant 16$ is approximately 6, so we assume here that the MC absolute magnitude distribution is 6 times larger than the NEA absolute magnitude distribution.

The MC SFD was defined as follows. We assumed that the top end of the SFD is set by the $H \leqslant 16$ population, with H converted to diameter by the relationship (J. W. Fowler & J. R. Chillemi 1992; Appendix in P. Pravec & A. W. Harris 2007)

$$D_{\mathrm{ast}}(\mathrm{km}) = 1329 \times 10^{-H/5}\, p_v^{-1/2}. \tag{5}$$

The standard representative visual geometric albedo chosen to make this change is $p_v = 0.14$ (A. W. Harris & P. W. Chodas 2021). The conversion has been recently revised by D. Nesvorný et al. (2024b) using a more complicated numerical approach, but for this paper we opted to keep things simple and use this value. Finally, for objects with $H > 16$, we grafted the shape of the debiased NEA SFD from Harris & Chodas (2021) onto our SFD. It defines $N_{\mathrm{MC\text{-}ast}}\,(> D_{\mathrm{MC\text{-}ast}})$ and is shown in Figure 12. We will discuss more about the shape of the NEA SFD in Section 4.1.3.

4.1.3. Near-Earth Asteroid Model

Our model of the NEA population is based on the work of M. Granvik et al. (2016, 2018). They constructed a model of the NEA population using the methodology described in W. F. Bottke et al. (2002). Specifically, they tracked ∼90,000 test asteroids escaping the inner, central, and outer main belt and followed them throughout the inner solar system using the numerical integrator SWIFT-RMVS4 (H. F. Levison & M. J. Duncan 1994). The planets Mercury through Neptune were included in these runs, and each asteroid was followed until it hit a planet, it hit the Sun, or Jupiter threw it out of the inner solar system. These results told them where objects were statistically most likely to spend their time. By combining these residence time probability distributions with a model of observation selection effects for NEA surveys, as well as an NEA absolute magnitude distribution with adjustable parameters, they were able to compare their model NEO population to NEAs detected between 2005 and 2013 by the Catalina Sky Survey. Using numerical methods to find a best-fit case, they were able to solve for the debiased orbital and absolute magnitude distribution of all NEOs, even those not yet detected.

Note that estimates of the debiased NEO orbit and absolute magnitude/size distributions have recently been revised and updated by D. Nesvorný et al. (2023, 2024a, 2024b). Our tests show relatively small changes in our collisional model results between using the NEA orbital model from M. Granvik et al. (2016; 2018) and using that from D. Nesvorný et al. (2023, 2024a). Given that most of our infrastructure and results are based on the M. Granvik et al. (2016, 2018) model, we have opted to continue to use them for this work rather than start over from scratch.

Using their NEA probability distribution in four dimensions (a, e, i, H), we used random deviates to create a population of 1214 objects, all nominally with $H \leqslant 18$ (gray circles in Figure 11(a)). These bodies were chosen to be our statistical sample representing the debiased orbital distribution of the NEO population. Using our collisional probability code, we calculated a look-up table of collisional probabilities and impact velocities defined as $P_{i,\ \mathrm{NEA}}$ (a, e, i) and $V_{\mathrm{imp,\ NEA}}$ (a, e, i).

For the NEA SFD, we had several options to choose from, but we opted to use the SFD provided by A. W. Harris & P. W. Chodas (2021). It defines $N_{\text{NEA-ast}}$ ($>D_{\text{NEA-ast}}$; Figure 12). It has the advantage over the others in that it goes to submeter sizes, values that are needed to calculate small-crater production on our target asteroids. Most alternative methods to calculate the NEA SFD only go to a few tens of meters at best, and this lower diameter limit is too large for our purposes (e.g., W. F. Bottke et al. 2002; M. Granvik et al. 2016, 2018; D. Nesvorný et al. 2023, 2024a, 2024b).

4.2. Crater Scaling Laws

Our next step is to convert the impact flux and impactor velocities from Section 4.1 into a crater production model for the time step in question. This requires the use of crater scaling laws appropriate for the target asteroid. Unfortunately, the properties of the asteroid are not known beforehand. For example, the first crater modeling results for Bennu used a strength scaling law (K. J. Walsh et al. 2019), while a later paper used gravity scaling (E. B. Bierhaus et al. 2022). Interestingly, we now have ground-truth data on crater formation for small carbonaceous-chondrite-like asteroids from the SCI experiment that was part of JAXA's Hayabusa2 mission to Ryugu (M. Arakawa et al. 2020).

The SCI experiment consisted of a 2 kg copper projectile that was accelerated to $\sim 2\ \mathrm{km\ s^{-1}}$ just prior to striking the surface of Ryugu (M. Arakawa et al. 2020). The projectile produced a crater on Ryugu that was nearly 14 m in diameter. This value indicates that a crater made by a carbonaceous-chondrite-type projectile with the same mass and impact velocity would be nearly two orders of magnitude larger than the projectile. This value is enormous; in comparison, modeling results show that observed craters on $D > 10$ km asteroids tend to have crater-to-projectile size ratios near 10 (W. F. Bottke et al. 2020). It also implies that Ryugu craters formed in the gravity regime rather than the strength regime (M. Arakawa et al. 2020).

Given this, we opted to use the crater scaling law suggested by E. Tatsumi & S. Sugita (2018) for craters in the gravity regime, as E. B. Bierhaus et al. (2022) also did in his work:

$$\frac{\rho_t \theta_c}{m_p + m_t} = K_1[\pi_2^* \pi_4^{-1/3} + K_2 \xi^{-(2+\mu_2)/2}]^{-3\mu_1/(2+\mu_1)} \tag{6}$$

$$\pi_2^* = \left(\frac{m_p}{m_p + m_t}\right)^{-\frac{7}{3}} \left(\frac{a_p g}{V^2}\right) \tag{7}$$

$$\pi_4 = \frac{\rho_t}{\rho_p} \tag{8}$$

$$\xi = \frac{m_p V^2/2}{m_t Q_D^*}. \tag{9}$$

Here the bulk densities of the projectile and target are ρ_p and ρ_t, the masses of the projectile and target are m_p and m_t, the volume of the crater is θ_c, the impactor radius is a_p, the gravity of the target body is g, the impact velocity is V, the energy per unit mass needed to produce the disruption of a typical body on the surface is Q^*_D, and μ_1, μ_2, K_1, and K_2 are experimentally derived parameters. The transient crater diameter D_{tr} can be calculated from the transient crater volume θ_{c} by assuming that it had a parabolic shape, such that $D_{\mathrm{tr}} \approx 2.2\theta_c^{1/3}$ (H. J. Melosh 1989). The final crater size D_{crater} is assumed to be $1.18 D_{\mathrm{tr}}$.

For Bennu and Ryugu, we adopted values for the parameters μ_1, μ_2, K_1, and K_2 of 0.41, 1.23, 0.24, and 0.01, respectively. For main-belt projectiles, we set the bulk density ρ_p to $1.3\ \mathrm{g\ cm^{-3}}$, given that most of the main belt is composed of C-complex objects (e.g., W. F. Bottke et al. 2020). The bulk densities of Bennu and Ryugu are both $1.19\ \mathrm{g\ cm^{-3}}$, while gravity g for Bennu is $6 \times 10^{-5}\ \mathrm{m\ s^{-2}}$ (M. G. Daly et al. 2020) and that for Ryugu is $1.4 \times 10^{-4}\ \mathrm{m\ s^{-2}}$ (M. Jutzi et al. 2022). Their Q^*_D values were set to $9.0 \times 10^6\ \mathrm{erg\ g^{-1}}$ (K. R. Housen & K. A. Holsapple 1999).

Some example results are as follows. For a 1 m diameter main-belt impactor ($a_p = 0.5$ m) striking Bennu and Ryugu at $V = 10\ \mathrm{km\ s^{-1}}$, a common impact velocity between main-belt projectiles and NEA targets (W. F. Bottke et al. 1996), these scaling laws yield a final crater size of 72 and 71 m, respectively. These results are both consistent with expectations based on the SCI results. They also suggest that the surface ages of both worlds are relatively young, since small projectiles can make sizable craters (see Section 2).

For Itokawa, insights into the appropriate crater scaling law for this asteroid can be gleaned from the DART spacecraft's impact into Dimorphos, the 150 m diameter S-type moon of (65803) Didymos. From their simulations of the collision, S. D. Raducan et al. (2024) found that Dimorphos had a weak cohesive strength of less than a few Pa, much like Ryugu and Bennu. Itokawa is also close to the asteroid size where Q^*_D

values reach their minimum (W. F. Bottke et al. 2020), so these size bodies are relatively easy to disrupt from an energy-per-mass perspective. On that basis, we will assume that Itokawa's craters formed close to or in the gravity regime.

For our crater scaling law, we will use the same parameters for K_1, K_2, μ_1, and μ_2 as Bennu and Ryugu, but we will change the bulk density to 1900 kg m^{-3} (A. Fujiwara et al. 2006). The gravity of Itokawa was set to 7.5×10^{-5} m s^{-2}, while the Q^*_D value was kept the same as before (9.0×10^6 erg g^{-1}; K. R. Housen & K. A. Holsapple 1999). Accordingly, a 1 m diameter main-belt impactor at $V = 10$ km s^{-1} yields a final crater size of 63 m. This value is comparable to those found for Bennu and Ryugu.

The scaling laws presented here allow us to generate a crater production model for each of the impactor populations discussed in Section 3.1. When our target NEA moves to the next *(a, e, i)* orbit along its orbital pathway, we calculate the number and sizes of craters formed in that time step from each impactor population. These SFDs are then added together and are used as input for our crater code CRASAT, which is described in the next section.

4.2.1. Sample Bennu Run

In Figures 11(a)–(c), we show an example of what the evolution of a model Bennu asteroid looks like compared to the location of the main-belt (black circles), Mars-crossing (red circles), and NEA populations (gray circles). The gold line represents the model asteroid's orbital path, with the small gold circles showing the orbit every 10,000 yr.

The object starts its journey in the innermost region of the main belt, with Yarkovsky drift moving it into the ν_6 resonance (W. F. Bottke et al. 2015b). From there, the body migrates to larger eccentricity values, it is removed from resonance by an Earth encounter, and then it gradually walks down to lower (*a*, *e*) values until it reaches the orbit of Bennu (magenta star).

The color contours in Figures 11(b) and (c) show the impact speeds of main-belt and solely Mars-crossing asteroids with our model Bennu, provided that it has an inclination $<5°$. One can see how the impact velocities change as a function of (*a, e*) and the limit to the reach of main-belt and Mars-crossing impacts.

4.3. CRASAT Code

Modeling crater formation on asteroid surfaces can be challenging to do correctly. As described by H. J. Melosh (1989), craters can be partially or completely erased when they land on top of one another, which we refer to here as "cookie-cutter" erasure. Their rims can also be softened and potentially destroyed by numerous smaller impacts, which we refer to here as "sandblasting" erasure. Crater models must also account for "saturation equilibrium," a state where the erosive and destructive effects of subsequent cratering prevent crater spatial densities from increasing on a given surface (D. E. Gault 1970; H. J. Melosh 1989). In equilibrium saturation, for every crater added to a surface, another is taken away.

To include these effects in our crater simulation, we modeled the production of crater SFDs using the crater formation and evolution model CRASAT (W. F. Bottke & C. R. Chapman 2006; S. Marchi et al. 2012). The overall approach of this code is similar to several crater formation and surface evolution models described in the literature (A. Woronow 1985; C. R. Chapman & W. B. McKinnon 1986; J. E. Richardson et al. 2005, 2020; J. E. Richardson 2009).

CRASAT simulates the random formation of craters on a square grid that represents the surface area of the target body. Each crater, defined as having diameter $D_{\rm crater}$, is drawn from an input crater production SFD using a random deviate and is placed sequentially onto the grid, with crater rims represented by circles in two dimensions. The location of each crater is also chosen using a random deviate and is recorded. The progress of the crater size distribution is provided throughout the simulation.

Crater obliteration by "cookie-cutter" erasure, defined as one crater landing on another and destroying some or all of it, is simulated as follows. CRASAT craters are defined by their rims; when 70% of a crater's rim has been removed by overlapping craters, we assume that it is no longer recognizable. When a new crater ($D_{\rm crater}$) is formed, it can destroy a portion of the rim of a putative crater underneath ($D_{\rm under}$), but only if $D_{\rm crater} > D_{\rm under}/f$, where *f* is a numerical factor. In this expression, *f* allows small craters of a given size to erase the rims of larger ones but prevents very small craters from having any effect. For example, 30 m craters formed on a 100 m crater will produce damage that is easily observable from images, but 1 m craters are less likely to do so.

While *f* is an unknown quantity, W. F. Bottke & C. R. Chapman (2006) determined its value empirically using crater-saturated terrains within the Sinus Medii region of the Moon (D. E. Gault 1970). As shown in Figure 9 of S. Marchi et al. (2012), the best-fit results used $f \sim 9$. We will use that value in our simulations.

Several papers have discussed the issue of boulder armoring (e.g,. E. Tatsumi & S. Sugita 2018; R.-L. Ballouz et al. 2020; E. B. Bierhaus et al. 2022). In this regime, very small impactors may be unable to reach the surface of a target asteroid covered by boulders and therefore do not make traditional craters. Instead, the impact takes place on the boulder itself, with the boulder protecting the surface from damage. E. B. Bierhaus et al. (2022) found that boulder armoring prevents the formation of craters on Bennu smaller than a few meters. For this reason, the smallest crater tracked in CRASAT for our Bennu simulations will be $D_{\rm crater} \geqslant 6$ m. While Itokawa and Ryugu are also covered with boulders, we are only using $D_{\rm crater} \geqslant 10$ m craters for this paper. Accordingly, while the boulder armoring regime may indeed exist for both asteroids, we are presumably avoiding it in our work. We also assume that boulder armoring does not affect the crater scaling law of modest-sized craters on any of our three asteroids.

Given our choice of $f \sim 9$, however, CRASAT still needs to account for the effects of impacts that are 9 times smaller than $D_{\rm crater} > 6$ and 10 m, depending on the target asteroid to be used. Both sizes are well within the boulder armoring regime. If there were no other effects included, this issue would force us to make modifications to CRASAT to account for boulder armoring. As we discuss in Section 3.3.1, however, we sidestep this issue by using a crater damage function, which is designed to approximate the behavior of impacts erasing small craters on the surface of our target bodies.

4.4. Small Crater Erasure in CRASAT

A number of $D < 10$ km asteroids have been observed by spacecraft at high enough resolution to assess their crater populations. In increasing order of size, and ignoring asteroid satellites like Dimorphos, Selam, and Dactyl, they are Itokawa, Bennu, Dinkinesh, Didymos, Ryugu, Toutatis, and Steins. The crater SFDs of these asteroids all appear to follow a similar pattern. Each shows several craters whose diameters are a sizable fraction of the diameter of the asteroid itself. These craters, when plotted as a cumulative SFD, have power-law slopes that generally match expectations based on crater production models and the crater SFDs found on large main-belt asteroids and the Moon (e.g., S. Marchi et al. 2015; W. F. Bottke et al. 2020; O. S. Barnouin et al. 2024; H. F. Levison et al. 2024). The cautionary note here would be that the largest craters are limited in number, so many slope fits are possible within uncertainties.

For smaller craters, however, the SFDs show a strong depletion compared to expectations, with the differences between observations and expectations growing larger as the craters decrease in size. As an example, for Bennu and Ryugu, which are 0.5 and 0.9 km in diameter, respectively, crater depletion on the cumulative SFD shown for Bennu in Figure 9 starts near crater sizes $D_{\text{crater}} < 0.1$ km, while those for Ryugu in Figure 10 start near $D_{\text{crater}} < 0.15$ km. The depletion continues on Bennu's surface to craters that are several meters in diameter. For craters smaller than that size, we enter the realm of boulder armoring, where small projectiles are more likely to make craters on individual boulders than on the surface (e.g., E. B. Bierhaus et al. 2022). While interesting, our focus is on crater sizes larger than the boulder armoring regime.

There is no single hypothesis to explain the missing craters at this time, but some ideas can be ruled out. For example, one hypothesis is that the main-belt and other populations are missing small asteroids (e.g., J. Saito et al. 2006). The problem is that such a putative reduction in population, whatever its cause, would produce a feedback effect in collisional evolution that would change the main-belt SFD at larger sizes (D. P. O'Brien & R. Greenberg 2005; D. P. O'Brien et al. 2006; W. F. Bottke et al. 2015a).

We argue that the most plausible scenario is that one or more physical mechanisms are erasing small craters. The possibilities include the following:

1. "Cookie-cutter" erasure, where larger craters overlap smaller ones (as already included in CRASAT).
2. Sandblasting erasure, where small impacts destroy the rims of larger craters (which is already included in CRASAT).
3. Spin-up from YORP thermal torques, which can lead to steeper slopes for high-latitude terrains and downhill mass movement when angle of repose is exceeded (e.g., E. R. Jawin et al. 2020, 2022). As discussed above, the ability of this effect to erase small craters depends on the circumstance and many different parameters (Section 2.4).
4. Close encounters with Earth (or Venus) capable of causing a resurfacing event on the target asteroid (e.g., D. C. Richardson et al. 1998; Y. Kim et al. 2023; see Section 2.5).
5. Impact-produced shattering of the target body. Here the target body loses enough mass that its cratered surface is reset. As discussed above, the threshold projectile size needed to produce a crater reset event is unknown, but it is likely smaller than the size needed for a catastrophic disruption (Section 2.3)
6. Impact-induced "jolting," where a large impact causes regolith across the surface to be launched off and redistributed around the surface, thereby burying small craters regionally or globally beyond some size (R. Greenberg et al. 1994; 1996; P. Michel et al. 2009). This effect is combined with ejecta blanket burial, where debris ejected from an impact site buries smaller craters near the crater site.
7. Impact-induced seismic shaking that mobilizes materials to flow downhill and fill in craters (J. E. Richardson et al. 2005, 2020; J. E. Richardson 2009; Y. Tang et al. 2023, 2024). We assume that impact-induced mass movement, where crater formation causes nearby boulders, rocks, and regolith to slide/move/jump away from the impact site, is similar to the kind of downhill movement favored on Bennu by E. R. Jawin et al. (2022).

Some mechanisms, like YORP spin-up or tidal resurfacing, may produce local, regional, or global crater erasure events, depending on the circumstances. The last two mechanisms, which will be discussed below, can be considered smaller versions of impact resurfacing. They erase small craters in a stochastic fashion while presumably preserving larger ones.

The reader should be aware that all these mechanisms, outside of cookie-cutter and sandblasting erasure, are difficult to model in a quantitative fashion within CRASAT. We have tested many different parameterizations of these mechanisms, but our limited knowledge of Bennu, Ryugu, and Itokawa in terms of their physical properties, interior structures, orbital and rotational histories, etc., has prevented us from finding a one-size-fits-all solution.

Accordingly, in the discussion below, we present what we know and what we tested, but our CRASAT model solution for small-crater erasure should be considered an approximate "work-around" solution.

4.4.1. Global Event-driven Crater Erasure

Both Bennu and Ryugu show evidence for mass movement of near-surface materials that could have erased some small craters (e.g., Y. Cho et al. 2021; O. S. Barnouin et al. 2022; M. E. Perry et al. 2022). In fact, E. R. Jawin et al. (2020, 2022) have shown that 5–10 m of material has been mobilized from midlatitudes to the equator on Bennu. Several mechanisms may have triggered this downslope movement, such as impact-triggered landslides (combined with impact-produced ejecta), YORP-driven slope increases, and/or jostling by Earth's tidal forces. While this flow may be a contributing factor to crater erasure through infilling, the lack of an obvious trend in crater-depth-to-diameter ratios from the midlatitudes to the equator makes it difficult to identify which mechanism is the most important for small-crater erasure (R. T. Daly et al. 2022).

Some important clues regarding crater evolution and erasure mechanisms can be found in the results from E. B. Bierhaus et al. (2022, 2023). They identified evidence for a transition in crater morphology for craters smaller than 25 m, which contain more small particles and fewer larger particles than surrounding terrains. They suggested that a possible source could be a global subsurface layer of finer-grained materials at a depth of 1–4 m. This putative layer would be breached by craters that were $D_{\text{crater}} > 25$ m. The source of this global layer would be seismic shaking from crater formation, which could potentially produce this layer over time by a variation of the "Brazil nut" effect.

Possibly related to these effects, crater SFDs on Bennu with different degrees of space weathering show similar differential power-law slopes, though the older craters illustrate some variation from a single slope (see Figure 15 of E. B. Bierhaus et al. 2023). The power-law slopes shown in E. B. Bierhaus et al. (2023) are broadly consistent with the expected production crater SFD identified among the very largest craters. They also suggest that a sizable event (e.g., the formation of a few very large craters; a close tidal encounter with Earth) led to an intermediate-sized crater erasure event (perhaps $D_{\mathrm{crat}} < 30$–40 m; E. B. Bierhaus et al. 2022). Evidence may also exist that a different event eliminated some large craters as well. After each erasure, the smaller craters would build up again, following a production crater SFD. On a cumulative plot, with all asteroid craters plotted, this effect would lead to a bend in the power-law SFD, with smaller craters at a shallower slope than the largest craters.

This kind of crater SFD may provide some support for the so-called "jolt" effect (R. Greenberg et al. 1994, 1996). This putative mechanism is caused when a large impactor hits a target asteroid hard enough to mobilize surface materials across the body. One result of jolting is that it can shake up and damage existing craters. A second is that it can launch some material off the surface at low velocities. When the debris returns and settles, it can partially or completely fill in small craters.

Depending on the size of the impactor, jolting can potentially erase craters smaller than some threshold size (D_{thresh}) over a local, regional, or global scale, though we caution that boulder armoring may affect this process. Craters with $D > D_{\mathrm{thresh}}$ will not be completely buried, so they will survive, though they may be damaged. For Bennu, it is possible that the largest craters produced different kinds of jolting events (E. B. Bierhaus et al. 2023). Similarly, jolting may explain why Ryugu's crater populations have different spatial densities across the body (Y. Cho et al. 2021).

As a proof of concept, we tried to test various forms of jolting within CRASAT, using Bennu as our target body. Whenever an impactor larger than a certain size struck Bennu, we assumed that jolting would damage or erase all craters smaller than a given diameter out to a predefined distance from the impact site. As part of this work, we developed the concept of a rim damage function, which we will use below. Rather than assume that a certain-sized crater had to be completely erased by a given jolt event, we instead assigned its rim elements a degree of damage that could range from 0 to 1. When the value 1 was reached, the rim element was assumed to have been erased. In this fashion, we could test different damage functions that vary based on the size/velocity of the impactor, the crater sizes to be erased, and distance from the impact site. In some cases, we assumed that the largest jolting events erased all small craters from the pole to the equator in latitude and several tens of degrees in longitude.

While our work did yield some interesting case studies, it did not lead to satisfying results. The reason is that at present we lack sufficient constraints to quantify our rim damage function for the jolt effect. The same problem exists for other proposed large-scale crater erasure mechanisms, such as YORP mass-shedding events, tidal resurfacing events, or nonjolt impact-driven resurfacing events. Examining existing geological studies of Bennu and Ryugu with such mechanisms in mind (e.g., Y. Cho et al. 2021; E. R. Jawin et al. 2020, 2022; E. B. Bierhaus et al. 2022, 2023) may be a productive avenue for future work.

4.4.2. Seismic Shaking and Impact-driven Mass Movement

A leading hypothesis to produce crater depletion is impact-induced seismic shaking (J. E. Richardson et al. 2005, 2009, 2020; D. P. O'Brien et al. 2006; P. Michel et al. 2009; Y. Tang et al. 2023, 2024). In this scenario, impacts on the target asteroid cause its regolith layer to vibrate in a low-g environment, which in turn produces sufficient particle, rock, and boulder migration to fill in and/or shake away craters. Evidence in support of seismic shaking can also be found on the 17 km diameter asteroid (433) Eros, with crater spatial densities lower near Shoemaker crater (P. C. Thomas & M. S. Robinson 2005). Over time, seismic shaking should mix and stir the regolith while also bringing large boulders to the surface by the so-called "Brazil nut effect" (e.g., H. Miyamoto et al. 2007; S. Matsumura et al. 2014; V. Perera et al. 2016; T. M. Yamada et al. 2016; C. Maurel et al. 2017; E. B. Bierhaus et al. 2023; Y. Tang et al. 2023, 2024). Impact-induced seismic shaking may also trigger landslides, such as those observed on Bennu (e.g., E. R. Jawin et al. 2020).

There have been many published models of how seismic shaking affects small asteroids (J. E. Richardson et al. 2005, 2020; J. E. Richardson 2009; Y. Tang et al. 2023, 2024). It can be argued that slumping observed on Bennu (K. J. Walsh et al. 2019) and Ryugu (S. Sugita et al. 2019) was produced by seismic shaking. Unfortunately, the rules governing how it affects shattered aggregates or rubble-pile bodies are complex. Ultimately, its effectiveness depends on the porosity and cohesion of an asteroid; high porosity and lower cohesion make it less effective (G. Nishiyama et al. 2021).

A poorly understood issue concerning impact-induced seismic shaking is how it depends on the size of the target asteroid. Consider (25143) Itokawa and (433) Eros, which are 0.3 and 17 km S-type asteroids, respectively (e.g., W. F. Bottke et al. 2020). The crater SFDs for each world have been imaged at high resolution (by JAXA's Hayabusa mission and NASA's NEAR-Shoemaker mission, respectively). Eros's SFD for 0.5 km $< D_{\mathrm{crater}} < 10$ km craters has a shape consistent with its formation by main-belt impactors (W. F. Bottke et al. 2020). For 0.2 km $< D_{\mathrm{crater}} < 0.5$ km craters, Eros's craters are largely in equilibrium saturation (C. R. Chapman 2002). One exception is the spatial density of 0.2 km $< D_{\mathrm{crater}} < 0.5$ km craters near the relatively young 7.6 km Shoemaker crater, which are 40% lower than other Eros regions (P. C. Thomas & M. S. Robinson 2005). As mentioned above, seismic shaking associated with the formation of Shoemaker crater may be responsible for this depletion.

If one assumes that small-crater erasure by seismic shaking is more difficult on larger asteroids, which presumably require highly energetic events to put materials across the entire surface into motion, our expectation is that Eros's crater SFD for small craters should be different from that of Itokawa. In fact, we might expect an increase in power-law slope at very small sizes, which would come from small craters formed between impact-induced seismic shaking episodes. These differences are not observed. Instead, each world shows increasing depletion for $D_{\rm crater} < 0.1$ km craters, with the resultant SFDs having similar shapes (see Figure 1 of P. Michel et al. 2009). These crater SFDs can be compared with Bennu and Ryugu, which both show evidence for crater depletion for $D_{\rm crater} < 0.1$ km craters (Figures 8 and 9; see also Figure 2 of N. Takaki et al. 2022). The fact that crater erasure does not appear to correlate with target size suggests that we are missing something in our understanding of impact-driven seismic shaking.

Additional information on this puzzling issue comes from the Hayabusa SCI experiment. It revealed that the cohesion of the subsurface layer on Ryugu is much smaller than previously assumed, with values of 1.4×10^{-4} MPa to 6.7×10^{-4} MPa (M. Arakawa et al. 2020). The cohesion of these materials is low enough that impact-induced seismic shaking in the gravity regime may be less viable for crater erasure than previously thought, at least in the sense of an impact erasing craters far from the impact site (R. Honda et al. 2021; N. Takaki et al. 2022). We note that the Hayabusa2 team did not identify seismic shaking as the primary cause of crater erasure on Ryugu (S. Sugita et al. 2019; M. Arakawa et al. 2020; G. Nishiyama et al. 2021; N. Takaki et al. 2022).

Conversely, the SCI experiment caused boulders within 20 m of the impact center to move at least 15 cm from their original locations (R. Honda et al. 2021; G. Nishiyama et al. 2021). Y. Tang et al. (2023, 2024) argued that this mass movement was initiated by seismic shaking. To make their case, they conducted a detailed survey of the surface boulder arrangement and geomorphology of two Bennu regions and then used a numerical model of seismic shaking to reproduce observations.

Taking a broader view, it seems fair to say that impact-driven mass movement is an important component of crater erasure on small asteroids (E. B. Bierhaus et al. 2022). Here seismic shaking can be combined with the idea that impacts also push around boulders, rocks, and regolith that can fill in and/or erase nearby craters. In other words, small impacts, by shaking or by shoving, provide the means to produce mobility on an asteroid's surface, albeit one that occurs on an intermittent basis. Examples of this may be found in E. B. Bierhaus et al. (2022, 2023), where they found that small craters on Bennu often were often surrounded by a ring of boulders.

It seems logical that this same mechanism should favor the erasure of small craters over larger ones. In addition, we know that Bennu is pummeled by many energetic meteoroids (W. F. Bottke et al. 2020). These powerful "kicks" to surface boulders in Bennu's low-g environment should also produce some limited mass movement over time.

One advantage of thinking about impact-driven mass movement in this way is as follows. Impacts should be able to push around boulders and regolith in a similar manner on many small bodies, including those of very different sizes (e.g., Itokawa, Bennu, Ryugu, and Eros). The main impediment to slowing or stopping this mechanism would be gravity; as bodies become larger, gravity can become strong enough to restrict the extent of such lateral movement. Impact-driven mass movement can also be assisted by seismic shaking and a near-surface layer of fine particles inferred to exist on Bennu and perhaps other small asteroids (E. B. Bierhaus et al. 2023). Our expectation is that this mechanism would erase craters all the way up to the largest formed on the surface. The issue is how to model this effect in some kind of quantitative manner.

4.4.3. CRASAT Damage Function for Impact-driven Mass Movement

As discussed in Section 4.4.2, simulating the impact-driven movement on surface material on small asteroids in a physically meaningful manner, as well as how such movement can erase small craters, is complicated, parameter dependent, and hard to quantify. It requires knowledge of the asteroid shape, surface and subsurface structure, the crater scaling law applicable to different asteroid sizes, the SFD of the impacting population, and how far a given impact can move material around. Similarly, as discussed in Section 4.4.1, regional/global crater erasure via impact-driven jolt, YORP-driven mass shedding, or tidal resurfacing is also a thorny problem. Our CRASAT tests to date have not produced an obvious path to success.

Given these challenges, we decided to use an approximate strategy to account for crater erasure on Bennu, Ryugu, and Itokawa within CRASAT. Based on what we learned from testing the jolt function in CRASAT, we decided to create a "crater damage function" that would track how different-sized craters degrade and erode over time. To the zeroth order, we assume that this function follows expectations for impact-driven mass movement mechanisms. It is an empirical function set by the user that allows one to match the observed crater SFD on each asteroid. The shape of the function constrains the nature and timing of the real crater erasure mechanism. The advantage in using this method is that crater damage functions from Bennu, Ryugu, and Itokawa can be readily compared to one another. It also tells you what the crater erasure mechanism needs to do to match observations.

Numerically, we have treated the crater damage function as follows. Every crater that forms on our target NEA larger than a minimum threshold diameter ($D_{\rm thresh}$) is assigned a size, position, and effective formation time in CRASAT. This means that its diameter is D_1 and the positions of its rim elements, which are defined by a series of (x, y) values on the surface grid, are tracked within two arrays, one for the x values (x_1) and one for the y values (y_1).

There are also small craters in CRASAT that can damage the rim of craters with $D > D_{\rm thresh}$. We must account for them, though we do not save their positions and size for future time steps. As discussed in Section 4.3, the smallest crater in CRASAT is defined by $D_{\rm thresh} = D_{\rm under}/f$, with $f = 9$ and $D_{\rm under}$ being the smallest crater used in our recorded SFD (see also S. Marchi et al. 2012). This means that we allow small craters with sizes between $D_{\rm thresh} \leqslant D_{\rm crater} < D_{\rm under}$ to form and damage the rims of craters modestly larger than $D_{\rm under}$.

Within CRASAT, we track time using the number of craters formed with $D_{\rm crater} \geqslant D_{\rm thresh}$. Hence, if the first crater on the surface has a diameter $D_{\rm crater} \geqslant D_{\rm under}$, it is assigned to be crater 1. It is given an effective age of n_1, where n_1 is the number of craters that have formed on the target surface with $D_{\rm crater} \geqslant D_{\rm thresh}$ at the formation time of crater 1 (e.g., if 10,000 craters with $D_{\rm crater} \geqslant D_{\rm thresh}$ formed in the model at the time crater 1 was created, the effective time is $n_1 = 10{,}000$). The same logic applies to crater 2, crater 3, etc., The effective time difference between crater 1 and crater x formation is then $\Delta n = n_x - n_1$.

The advantage of tracking time this way is that one can follow how crater populations evolve on a body without

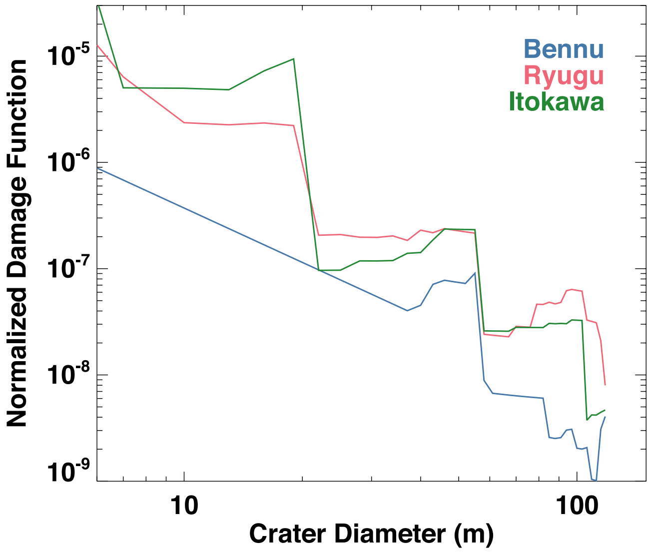

Figure 13. The crater damage function created for Bennu, Ryugu, and Itokawa. See text for details. The functions are normalized by Bennu's surface area for comparison. Larger values destroy craters faster.

worrying about how the production rate might change with time. This method is handy for many solar system problems, such as those where the impact flux is declining in some unknown manner. By making craters the clock, a single CRASAT run can provide useful information on a wide range of possibilities, provided that the impacting SFD keeps the same shape.

Our crater damage function is described as follows. After a given crater D_{crater} has formed, we perform checks at preset values of Δn to see whether it has been erased by our damage function. The probability of erasure P_{erase} for crater D_{crater} is

$$P_{\mathrm{erase}}(D_{\mathrm{crater}}) = 1 - e^{-\Delta n \lambda (D_{\mathrm{crater}})}. \tag{10}$$

Here λ (D_{crater}) is our assigned damage function, which is entered by the user. If a random deviate is less than P_{erase}, we consider the crater fully eroded and remove it from the population.

The damage functions for Bennu, Ryugu, and Itokawa, plotted as a function of crater size, are shown in Figure 13. Each has been normalized by Bennu's nondimensional surface area. For larger crater sizes, their behavior across the three cases is largely comparable to one another, but differences exist for smaller craters (particularly for Bennu). This could indicate that there is a dominant crater erasure mechanism that works on all three asteroids and that it is largely independent of target size.

5. Results

We are now ready to compare our model crater SFDs to the observed crater SFDs found on Bennu, Ryugu, and Itokawa (Section 3). For each of these target asteroids, we simulated 75, 77, and 49 possible orbital pathways from the body's starting orbit within the main belt to the asteroid's current (*a, e, i*) orbit. Our procedure was as follows.

Starting at the observed orbit of Bennu, Ryugu, or Itokawa, we moved each test asteroid backward to its previous output time step, which we will call t_1. Given that the time steps are 10,000 yr, the starting (*a, e, i*) orbit for t_1 is now 10,000 yr away from reaching Bennu, Ryugu, or Itokawa. From there, we tracked the path of the test asteroid's orbit forward in time and calculated how the model craters increased as the asteroid evolved to its observed orbit. When the observed orbit of Bennu, Ryugu, and Itokawa was reached, we compared the model crater SFD and the observed crater SFD using methods we will describe below. When complete, we start again and go back to the next farthest time step t_2, which is 20,000 yr away from reaching Bennu, Ryugu, or Itokawa. This process is repeated until we have a measure of the fits between the model and observed crater SFDs for all time steps.

The process described is relatively straightforward, but there are complications that need to be considered. For example, typical fitting procedures between model and data focus on where the data are most plentiful. For crater SFDs, this would be for the smallest craters. The problem is that small craters are the hardest to identify on Bennu, Ryugu, and Itokawa, and they are the most susceptible to crater erasure effects, shape distortion from boulders, etc. Beyond this, we are using an empirical (and imperfect) crater erasure function, we are unsure that we are using the correct crater scaling law, our model craters are created in a stochastic fashion, the orbits used are just a small set of all possible pathways that could be derived from a much larger numerical campaign, etc.

Given these limitations, we adopted the principle that "good enough" was reasonable when considering our fits between the model and observed crater SFDs; trying to account for all fit and model uncertainties in the most quantitative fashion possible was not going to yield more clarity. Accordingly, we decided to adopt a scoring method used successfully in W. F. Bottke et al. (2010, 2020, 2023, 2024) to track fits between model and observed SFDs. For each crater SFD, we created a distribution of N points interpolated from the data that are uniform in log D. The value of N was typically several tens. Next, we set up a scoring system like that described in W. F. Bottke et al. (2010) and looked for fits that minimized the score between the crater production model at different times and our synthetic craters:

$$S = \sum_{i=1}^{M} (N_{\mathrm{model}}(>D_i) - N_{\mathrm{obs}}(>D_i))^2. \tag{11}$$

Here N_{model} and N_{obs} are the cumulative numbers of model and synthetic craters, respectively, and $D_i = 1,\ldots, M$, are the diameters of model and synthetic craters. This equation resembles a χ^2 test, but because the craters were created for fitting purposes, the denominator is not statistically meaningful, so it is dropped.

To further demonstrate our method, Figure 14 shows different scores for Ryugu, calculated between different model runs and the observed crater SFD. Sample runs with low, medium, and high scores (S) are shown in the left, middle, and right panels, respectively. The lower scores correspond to better fits. Note that we assumed that all runs had to have at least one model crater as large as the observed craters to achieve a valid score.

From these kinds of runs, our job was to select a threshold score for an acceptable fit. Unfortunately, this required us to balance many subjective factors. For example, cratering is a stochastic process, so perfect fits between model and data will be rare. Accordingly, by choosing a threshold score too low, one can end up with results skewed toward larger surface ages. As a second example, consider the fit between the green curve in the left panel ($S = 570$) and the black curve in the middle

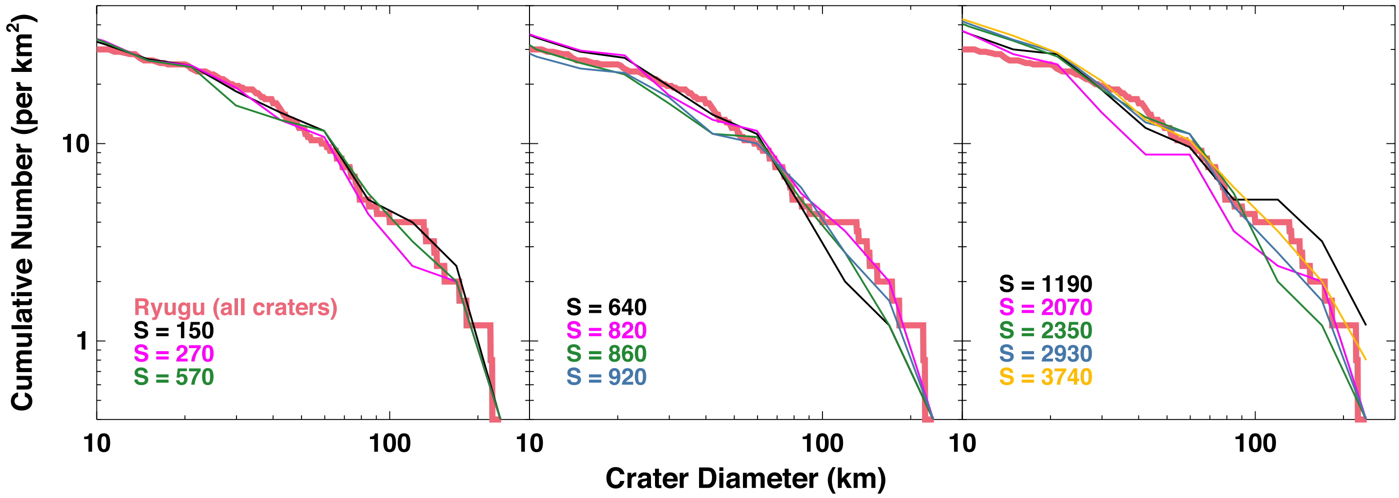

Figure 14. Example scores (S) for Ryugu between different model crater SFDs and its observed crater SFD (Figure 9). The low, medium, and high scores are shown in the left, middle, and right panels, respectively. The scores were calculated using Equation (11). The fit qualities in the left and middle panels represent those used to generate our minimum surface ages in Figure 9.

panel ($S = 640$). While both scores are similar, the green curve's fit is arguably more visually appealing than the black one. The difference is that the black curve has a superior match for smaller craters while the green curve is better for larger craters. Favoring one curve over the other could be accomplished by further modifying our scoring system, but at the cost of additional subjectivity.

Given these considerations, we decided to treat these above issues as follows. Using our "good enough" principle, we selected modest threshold scores for our Bennu, Ryugu, and Itokawa runs that balance the issues discussed above. Acceptable fits between the model and observed SFDs were deemed to be comparable to those from the middle panel of Figure 14 (e.g., $S < 900$ for Ryugu). Our fits for our crater SFDs are shown in Figures 8–10.

We also assumed that in each run the first occurrence of a score lower than the threshold score defines the minimum surface age of that world. These values make up the surface ages discussed below. The only exception was when several back-to-back surface ages had scores below the threshold score. In that circumstance, we selected the minimum score from the set.

In a few cases, when Bennu, Ryugu, and Itokawa are evolving along low (a, e) orbits (Figures 2–3), we find that the set of back-to-back scores below the threshold score may become extensive. The reason is that these regions have a low impact flux, allowing the incremental addition of small craters to be more or less balanced against small-crater erasure. We cannot rule out such older ages, but they are rare enough that they are not the focus of our analysis.

5.1. Bennu

5.1.1. Model Surface Ages for Bennu

We start with our analysis of Bennu. The cratering score is used to determine the best match between our 75 simulations and the measured data. Figure 8 shows this comparison, both for the full crater SFD (blue curve) and for the crater SFD of the youngest, reddest craters on Bennu (magenta curve). Our mean simulation is shown in gold.

We find relatively good matches between our simulation and the measurements. With that said, our simulations do not fully capture the abundance of large red craters, with the largest ones modestly offset from our production SFD. One possible explanation is that one of the largest red craters formed a little before expectations based on our production population. Matching crater SFDs that happen to include stochastic behavior is always a complicated affair in Monte Carlo models. A second explanation is that the real crater erasure function changes as a function of time, and we are not quite capturing its true behavior for very young ages. We find this plausible, in that our crater damage function is designed to reproduce the shape of the full crater SFD, not the youngest craters. Regardless, the mismatch between model and observations is minor and does not affect our age predictions.

The surface ages of the reddest craters (i.e., the least space weathered) are shown on the left side of Figure 15. We find that the youngest space-weathered surface is 60,000 yr old, while the median age of the distribution is 220,000 yr old. These ages compare reasonably well to previous estimates from D. N. DellaGiustina et al. (2020), who found that the reddest craters were less than $\sim 10^5$ yr old if the craters formed in the gravity regime of their chosen crater scaling law. Note that D. N. DellaGiustina et al. (2020) assumed that Bennu was being hit by the same impact flux as the Moon, which we consider to be a reasonable approximation for Bennu's current semimajor axis and eccentricity of 1.1264 au and 0.204, respectively. Bennu cannot move very far in less than $\sim 10^5$ yr, so its present-day (a, e, i) parameters should be similar to those from modestly earlier in its evolution; therefore, we should expect Bennu to have a similar impact flux in both orbits. They also match results from E. B. Bierhaus et al. (2023), who computed an age of $\sim$150,000 yr for the reddest craters.

Note that these results appear consistent with the expected timescales for space weathering on the S-type asteroid Itokawa, based on an analysis of its returned samples (L. P. Keller & E. L. Berger 2014). One grain named RA-QD02-0211 yielded a minimum space-weathering age of $\geqslant$30,000 yr, under the assumption that the solar flare track production rate at 1 au was the same as that for Itokawa at 1.324 au. Laboratory studies of space weathering in primitive

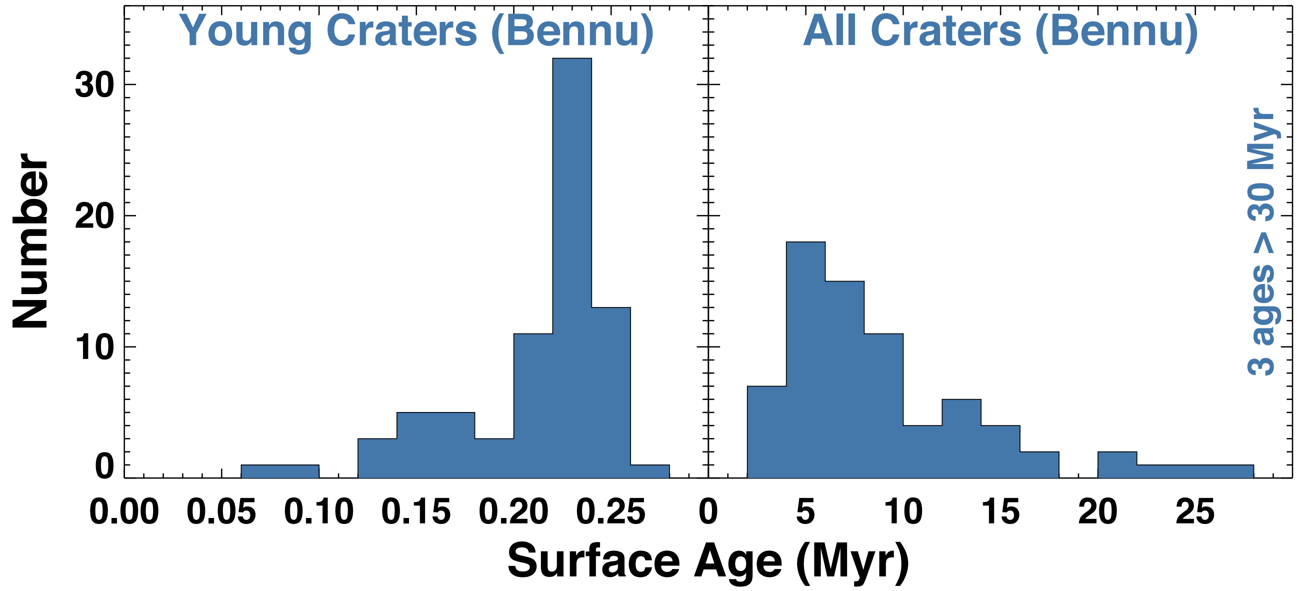

Figure 15. The computed surface ages for Bennu's youngest craters (left) and all craters (right). They represent the time in the past when our model crater SFDs achieved their best match with the observed SFD of Bennu's craters (i.e., for a given test asteroid's orbital pathway, the lowest score found for all possible time steps, with the score calculated using Equation (11); Figure 8). The median ages for the young craters are 0.22 Myr, while those for all craters are 7.7 Myr. The spread in these ages corresponds to 75 different orbital pathways for Bennu (Figure 2).

carbonaceous chondrite meteorites yield similar kinds of ages, with timescales similar to 10^4 yr (C. Lantz et al. 2017).

When better measures of space-weathering rates become available from the returned Bennu samples, it may be possible to use the degree of space weathering found on young Bennu craters to estimate their ages. If those ages, as a group, turn out to be younger than our model estimates, it could be an indication that our crater scaling law needs revision.

For example, right now, CRASAT is often assuming that the ratio of crater to projectile sizes for main-belt projectiles is comparable to 70 or so, with values up to 100 being relatively common. To achieve even younger ages, our crater scaling law may need to consistently yield ratios larger than 100. This could imply that we need to tweak our assumed crater scaling law parameters or that CRASAT is not fully capturing the effects of high-velocity projectiles coming from the NEA population.

The same procedure was applied to the full Bennu crater SFD, with the expected surface ages shown on the right side of Figure 15. We find that the most probable surface age for Bennu is 5 Myr, with the median surface age being 7.8 Myr. A tail of surface ages extends out to 30 Myr. They are linked to orbital evolution pathways where our model Bennus reside for an extended time on deep NEA orbits. They are decoupled from the main belt but not from the Mars-crossing or NEA populations, so they experience a lower impact flux prior to reaching Bennu's current (a, e, i) orbit. These pathways yield older crater retention ages than our more nominal cases, where the model Bennus move relatively quickly from main-belt-crossing orbits to Bennu's existing orbit.

These model surface ages for Bennu tend to be younger than some previously reported in the literature. The reason is dominated by the crater scaling law used by NEA-EVOL, though the impactor model used also plays some role. For example, K. J. Walsh et al. (2019) used a crater production model where it was assumed that nearly all of Bennu's craters were made while it was drifting across the inner main belt. Combined with a crater scaling law that assumed dry soil with a strength of 0.18 MPa, they found ages of between 100 Myr and 1 Gyr. In W. F. Bottke et al. (2020), two options were provided for the surface ages of Bennu, Ryugu, and Itokawa. One assumed that crater scaling laws designed to reproduce crater SFDs on $D > 10$ km main-belt asteroids were applicable to $D < 10$ km asteroids, and a second assumed that different scaling laws applied to $D < 10$ km bodies. For the former scaling law, W. F. Bottke et al. (2020) estimated that the surface age of Bennu, Ryugu, and Itokawa could be nearly 1 Gyr old. No age was calculated for alternative scaling laws, but the assumption was that all three asteroids could be considerably younger.

In hindsight, there is a crucial issue that needs to be factored in when choosing a crater scaling law for a small asteroid. From an impact energy per mass perspective, asteroids with diameters near 0.2 km are the easiest to catastrophically disrupt (e.g., see Figure 2 of W. F. Bottke et al. 2020). For reference, Bennu, Ryugu, and Itokawa are not far from these sizes. This implies that projectiles modestly smaller than the size needed for disruption must make craters that rival the diameter of the target body and/or they must reconfigure the target body itself. This was seen for the DART spacecraft's impact into Dimorphos, which did not create a crater but instead may have reshaped the body (S. D. Raducan et al. 2024). Accordingly, while the ratio between crater and projectile sizes on $D > 10$ km asteroids was found to be ~ 10 (W. F. Bottke et al. 2020), for asteroids near 0.2 km, that same ratio must be substantially higher than 10.

Accordingly, E. B. Bierhaus et al. (2022), using the E. Tatsumi & S. Sugita (2018) scaling law but with modestly different parameters than those used here, found a much shorter surface age for Bennu than K. J. Walsh et al. (2019), namely $\sim$10–65 Myr based on $D_{\rm crater} > 100$ m craters. Conversely, E. B. Bierhaus et al. (2022) found an age of 1.6–2.2 Myr for $D_{\rm crater} < 30$–40 m craters, which is younger than the ages reported above. In their work, they examined different differential crater SFDs on Bennu and argued that the $D_{\mathrm{crater}} < 30–40$ m craters were in production. This suggests that they formed after a major crater erasure event that preserved most large craters. The 1.6–2.2 Myr age was determined by comparing their differential SFD to model crater SFDs in production.

5.1.2. Comparison with Cosmic-Ray Exposure Ages and Related Ages

It is interesting to compare Bennu's model surface ages to the CRE ages measured for Bennu samples. The primary collection site for the OSIRIS-REx samples was called Nightingale. It was located at high northern latitudes (56° latitude; 43° longitude) within a 20 m diameter crater whose spectral signature was very red. As discussed above, these spectral attributes suggested that the crater had formed recently and had exposed relatively fresh dark materials. Of the four candidate sample sites on Bennu, Nightingale had the lowest temperature (B. Rozitis et al. 2022). The regolith at the site also appeared likely to contain fine-grained material with sizes suitable for return within the OSIRIS-REx sample head (e.g., K. N. Burke et al. 2021). Sample extraction and return were successful, with the OSIRIS-REx mission returning 121.6 g safely to Earth (D. S. Lauretta et al. 2024).

CRE ages define how long the grains have been within a few meters of the surface of the body. As a reference, consider that surface materials taken back from the Moon by the Apollo astronauts often have CRE ages that are many hundreds of Myr old (R. Wieler 2002). In contrast, measurements of different grains within the Bennu samples showed that they had CRE ages between 1 and 6 Myr (B. Marty et al. 2024). Five of the eight grains examined so far have ages between 1 and 2 Myr, while two have ages near 3 Myr and one has an age between 5 and 6 Myr.

These oldest ages are an intriguing match with our most likely crater retention ages for Bennu, which are between 4 and 6 Myr. We find it plausible that the oldest CRE ages in the samples represent the time of the last major resurfacing event on Bennu. The younger CRE ages are a match for the 1.6–2.2 Myr ages of $D_{\mathrm{crater}} < 30–40$ m craters from E. B. Bierhaus et al. (2023).

The youngest CRE ages from Bennu are more difficult to define. Given our work above, the red source crater within Nightingale is probably $\lesssim 0.2$ Myr, so none of the grains appear linked to its formation (see also D. N. DellaGiustina et al. 2020; E. B. Bierhaus et al. 2023). It seems more likely that these sample ages represent some kind of churn timescale for the near surface, with small impacts constantly moving around boulders, blocks, and regolith (e.g., N. Takaki et al. 2022). These events would presumably bring some subsurface material close enough to the surface to receive cosmic-ray damage.

Bennu samples appear to be most consistent with known CI chondrites (D. S. Lauretta et al. 2024). We will review what we know of the CRE ages of CI chondrites in the next section. To set the stage, we find it useful to review what we know of CRE ages for CMs, which may be as weak as many CI chondrites and at least some of the Bennu samples.

Over 100 CMs have been analyzed to date, with recent analysis provided by M. Zolensky et al. (2020) and D. Krietsch et al. (2021). Drawing on the work of K. Nishiizumi & M. W. Caffee (2012), M. Zolensky et al. (2020) report that CMs have a CRE age distribution with several peaks near 0.2, 0.5, and 2 Myr. Most CM chondrites have very short CRE ages of <2 Myr, and none were older than about 8 Myr.

In D. Krietsch et al. (2021), the CRE ages from their own work and those from the literature are combined and are shown as a probability distribution (see their Figure 9). They find that the largest cluster of CRE ages is near ∼0.2 Myr. Other CRE age peaks are at 1 Myr, 4.5–6 Myr, and 8 Myr. A few of the newly measured CM meteorites from D. Krietsch et al. (2021) have ages beyond 11 Myr, which has never been seen before among previously dated CM meteorites.

Overall, the oldest CM ages in the CRE age distribution are compatible to the age distribution found in the Bennu samples to date. The CM peak near 0.2 Myr, however, is not observed, nor do any Bennu samples have ages <1 Myr (so far). Our thoughts on the source of these peaks will be provided in Section 6.

Another measure of the surface age of Bennu comes from its boulders. Examining images of meteoroid impact craters on Bennu's boulders, R.-L. Ballouz et al. (2020) determined that the likely impact strength of meter-sized boulders was 0.44–1.7 MPa. From there, they estimated that the surface exposure age of the meter-sized boulders from meteoroid impacts was 1.75 ± 0.75 Myr. These ages are consistent with the CRE ages of many Bennu particles, as discussed above.

R.-L. Ballouz et al. (2020) argued that 1.75 ± 0.75 Myr was equivalent to the time Bennu has been decoupled from the main-belt impactor population, though in the title it was imprecisely described as the age when Bennu became an NEA. We find this time to be a good match with our work. Using our 75 test asteroids for Bennu and the same codes used to make Figure 3, we find that the median time that Bennu has been decoupled from main-belt collisions is 3.1 Myr.

5.2. Ryugu

5.2.1. Model Surface Ages for Ryugu

Overall, while Ryugu shows the same general behavior as Bennu when it comes to its dynamical evolution (Figure 2), Ryugu's crater SFD shows a different qualitative shape than Bennu's crater SFD (Figures 8 and 9). Notably, Ryugu's SFD levels off at small crater diameters, whereas Bennu's slope continues more steeply. This difference is probably an artifact of the data, as OSIRIS-REx obtained higher-resolution images of Bennu's global surface (D. N. DellaGiustina et al. 2018) than Hayabusa2 did with Ryugu (S. Sugita et al. 2019). OSIRIS-REx also had the additional advantage of being able to globally map the surface using a scanning laser altimeter (M. G. Daly et al. 2017).

We have opted to track Ryugu's crater SFD down to 10 m using our CRASAT model results, though we caution that N. Hirata et al. (2020) set a minimum diameter threshold of 20 m. The difference in tracking craters with $D_{\mathrm{crater}} > 10$ m and > 20 m does not meaningfully affect our results in terms of determining the surface age of Ryugu.

The results of our Ryugu simulations are shown in Figure 9. By eye, we find good agreement between our model crater SFDs (gold lines) and the observed crater SFD (red line). The differences that do exist may be the result of an inexact damage function or the stochastic effects of drawing a model crater SFD from an idealized production SFD.

Our model surface ages for Ryugu are shown in Figure 16. Most simulations match the full SFD within 8 Myr. Only a few

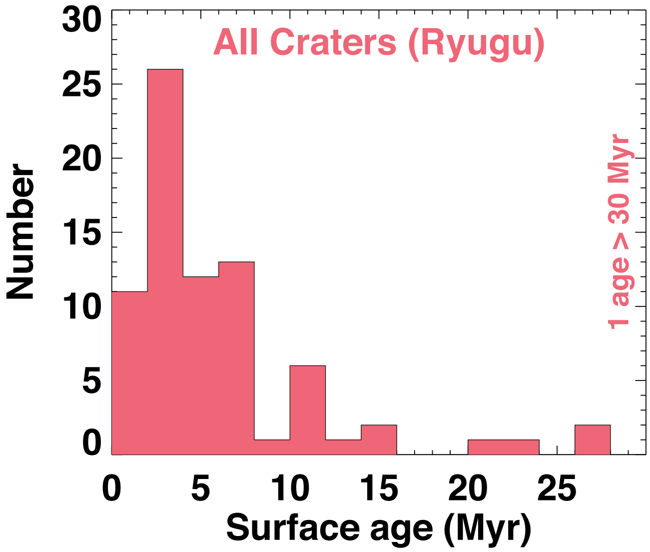

Figure 16. The surface ages for Ryugu's craters. They represent the time in the past when our model crater SFDs achieved their best match with the observed SFD of Ryugu's craters (Figure 9). The median ages for the model craters are 4.1 Myr. The spread in ages corresponds to 77 different orbital pathways for Ryugu (Figure 2).

outliers take longer than this time. They correspond to simulations in which Ryugu spends some extended time on solely Mars-crossing orbits or deep within NEA space decoupled from the main belt. The median surface age is 4.1 Myr.

5.2.2. Comparison with Cosmic-Ray Exposure Ages and Related Ages

Previous estimates of Ryugu's surface age can be found in S. Sugita et al. (2019). As with Bennu, the values can vary widely based on the impactor model and the choice of crater scaling law. By assuming that most craters formed when Ryugu was within the main asteroid belt, that craters on Ryugu form in material with an effective strength around 0.18 MPa, and that Ryugu's surface age is represented by 100–200 m diameter craters, S. Sugita et al. (2019) calculated a representative age of 158 ± 47 Myr. Alternatively, by changing the crater scaling law so craters formed in strengthless material (i.e., within the gravity-controlled regime; M. Arakawa et al. 2020), the surface age was reduced to 7.8 ± 2.3 Myr (from their supplemental materials) or 8.9 ± 2.5 Myr (from the label on their Figure 2(e)). The last two values are similar to our estimated surface ages for Ryugu.

An update to these ages was provided by Y. Cho et al. (2021). In their work, surface ages were calculated for distinct regions as well as the entire surface. To make a direct comparison with our work, we concentrate on the latter ages. Making the same assumptions as S. Sugita et al. (2019) for their impacting population and crater scaling laws, they found that $D_{\mathrm{crater}} > 100$ m craters yielded a surface age of 8.1 ± 2.5 Myr. A different model calculation based on the population of $D_{\mathrm{crater}} > 70$–80 m craters, which have likely experienced some crater erasure, yielded 4.1 ± 1.1 Myr. As before, our range of model surface ages in Figure 16 is compatible with these ages.

Y. Cho et al. (2021) also mention that Ryugu was likely decoupled from the main belt between 0.2 and 7 Myr ago, with the latter age representing the crater age of Ryugu if all impactors came from the NEA population. In their text, however, their choice for the NEA SFD is not specified. Given that the NEA population is about a factor of 1000 smaller than the main-belt population (Figure 12), we suspect that the latter age is probably too high, or that their crater production model is being fit to the small craters, which is challenging to do because the craters have likely experienced substantial crater erasure.

CRE ages have also been calculated for over 20 Ryugu samples. Those in Chamber A came from Ryugu's equatorial ridge region, where 3.237 ± 0.002 g of samples were recovered (T. Yada et al. 2021). As reported by K. Nishiizumi & M. W. Caffee (2023), these samples had CRE ages that ranged from 2.9 to 7.5 Myr. The samples in Chamber C, which had a net mass of 2.025 ± 0.003 g, came from the second touchdown sampling event near the crater created by the SCI experiment (T. Yada et al. 2021). This collection location was chosen to gather subsurface materials excavated by SCI that had not experienced long-term exposure to space. Their CRE ages ranged from 1.6 to 5.8 Myr (K. Nagao et al. 2022; R. Okazaki et al. 2022; K. Nishiizumi & M. W. Caffee 2023). The CRE ages of the surface and subsurface samples discussed in R. Okazaki et al. (2022) are 5.3 ± 0.9 Myr and 5.2 ± 0.8 Myr, respectively.

All these ages are comparable to the calculated surface age for Ryugu from our model, with probable ages going out to 8 Myr. As with Bennu, the shorter ages would suggest some degree of mixing or churn in the uppermost layers of Ryugu. The reason the ages do not go longer than 5.8–7.8 Myr could be because that was the time Ryugu experienced a global resurfacing event.

The samples returned from Ryugu are thought to have CI chondrite composition. As discussed in K. Nishiizumi & M. W. Caffee (2023), this means that a comparison between the Hayabusa2 CRE ages and those of CI1 meteorite samples may yield insights into their origins on their precursor bodies. In their Table 1, they list their ages that have been calculated from both radionuclide and ^{21}Ne concentrations. For the meteorite Alais, they adopt a CRE age of 8 Myr, the longest exposure age of the known CI1 meteorites. For Ivuna, they find a CRE age of 0.16 ± 0.02 Myr, with some evidence that the meteorite has been exposed multiple times. So far, out of 100 CI or CM tested, it is the only one that shows evidence for a complex exposure. For Orgueil, its radiometric CRE age is 6–8 Myr, while its noble gas CRE age is 2.8 Myr. K. Nishiizumi & M. W. Caffee (2023) point out that these two ages are inconsistent with one another. For Tonk, the noble gas CRE age is 1.6 Myr, while for Y-86029, 980115, and 980134 the CI1 are nearly the same at 0.14 ± 0.02 Myr. They remark that these values are similar to Ivuna.

In summary, the older CRE ages of the CI1s are comparable to the oldest ages found among both the Bennu and Ryugu samples, as well as the CRE ages in the CM chondrites (see Section 5.1.2). The youngest CRE ages of the CI1s, however, are several Myr younger than the youngest CRE ages in the Ryugu samples. Taken at face value, this could suggest that the young CI1 ages were produced by cratering events on CI-like asteroids on Earth-crossing orbits, while the oldest ages correspond to global resurfacing events on those CI1 asteroids.

There are also additional possibilities to consider. First, consider that Earth's atmosphere is screening out many weak CI1 from reaching the ground, so the CRE ages of the CI1 meteorites are almost certainly biased. Second, Bennu and Ryugu are only two asteroids among a sizable population of low-albedo NEAs. No one has yet attempted to quantitatively model the flux of CI1 material collectively coming from all these bodies. For the youngest CRE ages, it is possible that resurfacing events driven by YORP mass-shedding and tidal resurfacing events among CI1-like NEAs (Figures 6 and 7) are producing much of the meteorite flux, though more modeling and constraints in the area are needed.

What we can reasonably say at this time is that the apparent match between the older CRE ages of the CI1 and CM meteorites and the surfaces ages of Bennu and Ryugu does suggest that much of the CI1 flux could plausibly be coming from NEAs whose surface reset times are near these values. The question is whether this assertion is consistent with other meteorite constraints. We will return to this topic in Section 6.

5.3. Itokawa

5.3.1. Model Surface Ages for Itokawa

Using our NEA-EVOL infrastructure, we can also examine the crater histories of NEAs that have a different composition than CI chondrite-like bodies Bennu and Ryugu, namely ordinary chondrite-like Itokawa. The complicating issue is that the crater scaling law used for Itokawa lacks direct constraints, such as the SCI experiment employed at Ryugu by the Hayabusa2 mission. The reader should be advised that this means that our estimated surface ages for Itokawa may need future revision as new information is brought to light. Future missions to sub-kilometer-sized S-type asteroids with surface-interaction experiments, such as OSIRIS-APEX to the 300 m diameter asteroid (99942) Apophis, may provide us with new data that can improve our crater scaling laws (D. N. DellaGiustina et al. 2023).

Itokawa's current orbit is similar to that of Bennu and Ryugu, with $(a, e, i) = (1.324\ \text{au}, 0.280, 1^\circ\!.621)$ (Figure 2). This is not a surprise, in that sample-return missions prefer targets with Earth-like orbits that allow spacecraft to get there, rendezvous, and come back with limited propellant. Accordingly, the orbital evolution of Itokawa from the main belt follows the same general dynamical pathway trends discussed above with Bennu and Ryugu (Figure 2).

A comparison between our model crater SFDs for Itokawa (gold lines) and the observed crater SFD (green line) is shown in Figure 10. There are a limited number of observed craters with $D > 10$ m, and the spread in the gold lines reflects that paucity. As with Bennu and Ryugu (Figures 15–16), most surface ages on Itokawa are <10–15 Myr (Figure 17). A large spike of ages exists for <2 Myr, with the median surface age being 3.1 Myr.

5.3.2. Comparisons with Previous Work and Sample Data

As with Bennu and Ryugu, the derived surface age of Itokawa depends strongly on the crater scaling law one chooses to use to model crater production on its surface, as well as the parameter choices made for the impacting population (e.g., impactor collision probabilities and impact velocities). In some cases, previous models have assumed that Itokawa received most of its craters while residing in the main belt.

P. Michel et al. (2009) tested different crater scaling laws that did and did not consider frictional resistance to shear flow during the crater modification phase. They found solutions where Itokawa's surface age is at least ~75 Myr and could be possibly as large as 1 Gyr (see also W. F. Bottke et al. 2020). By assuming that Itokawa's surface has a "soft soil" target strength of 10–20 kPa, J. E. Richardson et al. (2020) derived a surface age of 20 ± 5 Myr.

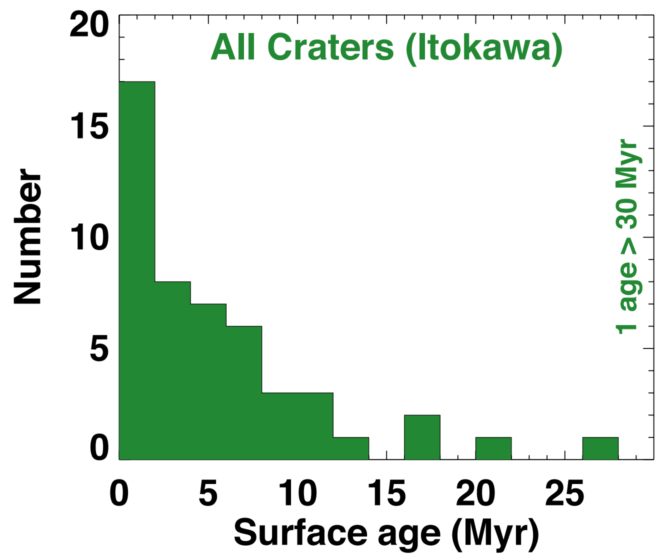

Figure 17. The surface ages for Itokawa's craters. They represent the time in the past when our model crater SFDs achieved their best match with the observed SFD of Itokawa's craters (Figure 10). The median ages for the craters are 3.2 Myr. The spread in ages corresponds to 49 different orbital pathways for Itokawa (Figure 2).

Using a crater scaling law based on laboratory shot experiments into coarse-grained targets, E. Tatsumi & S. Sugita (2018) derived an age range between 10 and 33 Myr for class 1–4 craters from N. Hirata et al. (2009) and ages of 3–17 Myr for class 1–2 craters. The closest values to our surface age estimates come from the latter case, probably because we use the same class 1–2 craters from N. Hirata et al. (2009). Most of the CRASAT model ages shown in Figure 16 are at the lower end of their 3–17 Myr range.

The CRE ages from Itokawa grains also constrain the surface age of the body, or at least the residence time of grains in the regolith. They show somewhat surprisingly young ages of ~1 Myr (M. M. M. Meier et al. 2013, 2014), with an upper limit of ~8 Myr that could also stretch to 66 Myr (K. Nagao et al. 2011). For exposure ages, the samples show 1.5 Myr for Ne (M. M. M. Meier et al. 2014) and >3–4 Myr for Be (K. Nishiizumi et al. 2015). Spectral ages, which may reflect the exposure time of the surface, were <10 Myr (S. Koga et al. 2014) and ~2–8 Myr (L. Bonal et al. 2015). These ages are consistent with those shown in Figure 17.

Note that Itokawa ages are considerably younger than the CRE ages of most LL chondrites. The majority have CRE ages that range between 5 and 50 Myr, with a peak near ~15 Myr (O. Eugster et al. 2006). There are only two LL chondrites with similar values: Appley Bridge, which is an LL6 with a CRE age of 1.5 ± 0.5 My, and Chelyabinsk, an LL5 with a CRE age of ~1.2 Ma (e.g., M. Trieloff et al. 2018). Overall, the LL chondrite data tell us that Itokawa's surface is younger than most of the ordinary chondrites reaching Earth.

Many of Itokawa's grains also show signs of abrasion, with rounded surfaces that could be a consequence of grain migration within the surface (A. Tsuchiyama et al. 2011). As

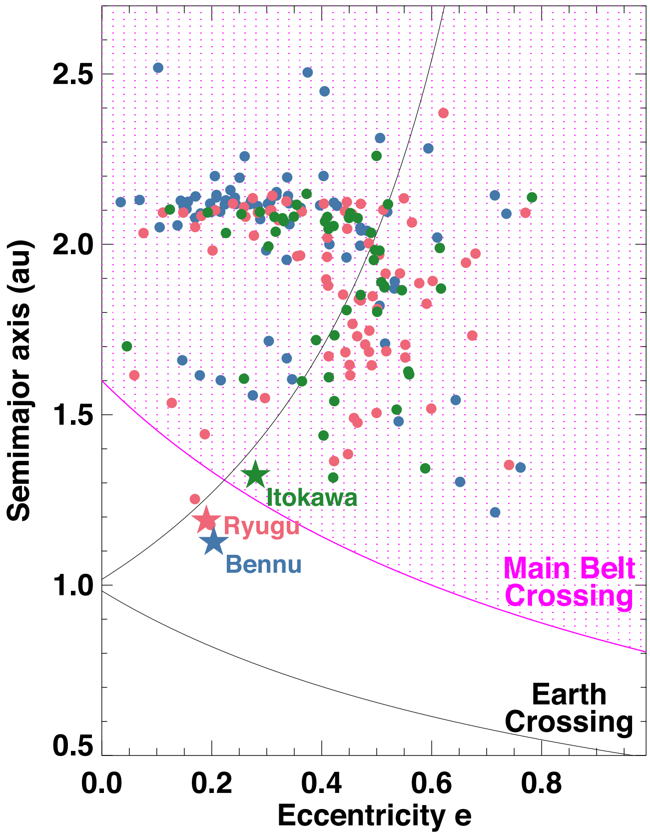

Figure 18. The predicted test asteroid orbits for Bennu (blue), Ryugu (red), and Itokawa (green) where their cratered surfaces were reset. See Figure 2 for label descriptions. Possible reset mechanisms are large impacts, YORP spin-up (which leads to landslides and mass shedding), and tidal resurfacing during a close Earth encounter. We lack sufficient information to say which mechanism affected the real Bennu, Ryugu, and Itokawa, but we can discuss trends. Nearly all test asteroids are on main-belt-crossing orbits. This suggests that impacts are a viable resurfacing mechanism for all three bodies. Tidal resurfacing is ruled out for bodies beyond the Earth-crossing line. See Figure 6 for additional context. YORP spin-up occurs more quickly for bodies with low perihelion values, but main-belt impact velocities are also high for such bodies (see Figure 12).

with Bennu and Ryugu, there appears to be some level of mixing and surface mobility on Itokawa. K. Nagao et al. (2011) argue that their short CRE ages are indicative of surface materials being lost at a rate of several tens of centimeters per million years, possibly from impacts or landslides.

6. Discussion

6.1. Possible Causes for Surface Reset Events

Using the predicted ages of our test asteroids for Bennu, Ryugu, and Itokawa from Figures 15–17, we can now consider their orbital locations when their surfaces were reset. Here we take advantage of the 75, 77, and 49 test asteroid pathways we have for these bodies, respectively. Starting at the observed orbits of each test asteroid, we can propagate their orbit backward in time as far as the calculated surface age. This yields the (a, e) orbits shown in Figure 18, for Bennu (blue circles), Ryugu (red circles), and Itokawa (green circles). The other labels were defined in Figure 2.

The predicted orbits give us insights into the mechanisms that may have caused the surface reset event (e.g., potentially caused by a large impact, YORP spin-up that produces landslides or mass shedding, and tidal resurfacing during a close Earth encounter). Our first observation is that nearly all the test asteroids are on main-belt-crossing orbits. This indicates that large impacts are a plausible resurfacing mechanism for Bennu, Ryugu, or Itokawa.

For our second observation, we compared the orbits in Figure 18 to the orbits where tidal resurfacing is most likely to occur, namely the red contours found in Figure 6. Few Bennu orbits are found near these contours, while a modest number from Ryugu and Itokawa are found with $a > 1.5$ au. This suggests that Bennu was unlikely to have experienced a tidal reset event, but the odds are better for Ryugu and Itokawa. With that said, the most likely orbits for tidal resurfacing have $a < 1.5$ au, and almost no orbits are found there. Our takeaway from this is that tidal resurfacing is unlikely for our target asteroids.

Our third observation is that Bennu, Ryugu, and Itokawa have many orbits with relatively large perihelion values (i.e., the upper right corner of the plot). Here impacts or YORP spin-up are plausible mechanisms. The same is true for bodies with low perihelion values that are far from the likely orbits needed for tidal resurfacing. YORP spin-up occurs more quickly for bodies with low perihelion values, but main-belt impact velocities are also higher for such bodies as well (Figure 12). Until we have more information on the nature of surface reset events on Bennu, Ryugu, and Itokawa, this may be as far as we can go with our predictions.

A telltale sign of YORP-driven resurfacing events may be a satellite. On that basis, it is curious why we do not see at least one of these bodies with a tiny moon. The answer may partly come from the composition of Bennu and Ryugu. As discussed in Section 2.5, C-type asteroids have a surprising paucity of moons compared to S-type asteroids (K. Minker & B. Carry 2023; L. Liberato et al. 2024). This might be indicative of low-cohesion, low-friction internal structures that allow the bodies to transform their shapes to deal with a modest increase in rotational angular momentum (Y. Zhang et al. 2022).

Another answer may come from the effects of Earth's tidal forces. As shown in Figure 8, the dynamical evolution of our test asteroids can bring them close to Earth, such that any putative satellites that existed would be readily removed during the encounter. We can even quantify this behavior. A. J. Meyer & D. J. Scheeres (2021) estimated that satellites are stripped from the primary at close-encounter distances of $\sim$50,000 km, or roughly 8 Earth radii. The cross section of the distance to the center of Earth goes as the square of the encounter distance, so the probability of one of our three bodies losing a moon from an Earth encounter should increase by over an order of magnitude over the likelihood of a collision with Earth (Figure 7). These kinds of results indicate that binary asteroids are dynamically fragile (Walsh et al. 2006; see also A. Morbidelli et al. 2006); if a body has an Earth-like orbit, it is more likely to have a close encounter with Earth, and that means that the probabilities will be high that a putative satellite would be lost via an encounter.

While additional work on impact-driven asteroid resurfacing is needed, new constraints now exist from the DART spacecraft's impact into Dimorphos. For example, using numerical hydrocodes capable of simulating the effects of impacts onto rubble-pile bodies, S. D. Raducan et al. (2024) showed that the Dimorphos impact produced global deformation and resurfacing. The predictions of their modeling results will be tested in the near future when ESA's Hera mission visits the Didymos–Dimorphos system (P. Michel et al. 2022).

6.2. The Curious Dichotomy in Meteorite Cosmic-Ray Exposure Ages

In Sections 5.1.1, 5.2.1, and 5.3.1, we discussed the CRE ages of CM, CI, and LL chondrites. In general, we found that the CM and CI have CRE ages that are usually <8 Myr, with many ages that are a few $\times$ 10^{-1} Myr to <2 Myr. In contrast, the LL chondrites, along with the other ordinary chondrites, achondrites, and those carbonaceous chondrites considered as strong as ordinary chondrites (i.e., CO, CK, CV), have a paucity of short CRE ages (O. Eugster et al. 2006). Overall, most CRE ages from the stronger meteorites are >6 Myr, with a large fraction having ages of several tens of Myr.

It is interesting to compare these CRE age distributions with the surface ages of Bennu, Ryugu, and Itokawa, all whose model crater retention ages are likely to be several Myr old (Figures 15–17; see also E. B. Bierhaus et al. 2023). While Itokawa is small and thus may not be a representative member of S-type NEAs, there is no question that Bennu, Ryugu, and Itokawa provide us with insights into the population of NEAs on Earth-like orbits. All three have short YORP spin-up timescales, and tidal resurfacing is possible as well, though it is more likely for Ryugu and Itokawa than for Bennu. Moreover, an excess population of sub–100 m objects has also been predicted to be on orbits similar to these three asteroids (e.g., Figure 5). Collectively, it seems like these kinds of NEAs should be capable of providing Earth with a considerable flux of short CRE age meteorites. If so, why do we not see more of them?

To explore this issue, it is useful to discuss the current thinking on the meteorite delivery process (e.g., W. F. Bottke et al. 2006b). It can be argued that meteorites are delivered to Earth as part of a collisional cascade, with some collisions taking place within the main belt. Stronger meteorites can evolve far enough by the Yarkovsky effect to enter into main-belt resonances. From there, these bodies can be driven into Earth-crossing orbits where they can hit Earth. The net transit time for stronger meteorites is many Myr to tens of Myr (P. Farinella et al. 1998; W. F. Bottke et al. 2006b).

Conversely, weaker meteorites like CM and CI chondrites cannot survive long as free-floating meter-sized objects without being disrupted. They would be dependent on larger precursors acting as "motherships" to transfer them onto Earth-crossing orbits. Their CRE ages would represent the transit time from when they were ejected from their precursors, already in Earth-crossing space, to when they reached the surface of Earth. Moreover, if they were weak enough, only a small fraction would survive passage through Earth's atmosphere. Given that only a few percent of all meteorite falls are CM or CI compared to the combined flux of ordinary chondrites and achondrites (e.g., T. H. Burbine et al. 2002) and that most materials observed on and returned from Bennu and Ryugu are thought to be weak (e.g., D. S. Lauretta et al. 2024), this scenario makes sense from a big-picture standpoint.

There is much to like about the story presented above, but certain worrisome details have troubled us for some time. For example, our NEA-EVOL model allows one to calculate the collisional lifetimes of objects throughout the inner solar system. Given that the NEA population is many orders of magnitude smaller than the main belt, it stands to reason that once meteorite precursors become decoupled from the main belt (i.e., once they are on low (a, e) orbits), they are much less likely to undergo a collisional disruption event from small asteroidal impactors. We also know that the dynamical lifetimes of objects on low (a, e) orbits can be tens of Myr, long enough to build up a sizable steady-state population of NEAs (e.g, W. F. Bottke et al. 2002; M. Granvik et al. 2016, 2018; D. Nesvorný et al. 2023, 2024a, 2024b). If these low (a, e) NEAs are also ejecting rocks and boulders via YORP spin-up mechanisms or tidal disruption, it seems probable that (i) the weaker meteorites should have a sizable fraction of CRE ages >8 Myr and (ii) the stronger meteorites should have a sizable fraction with CRE ages <6 Myr. This creates a paradox: where are these meteorites?

For stronger meteorites, the easiest solution is that the flux of meter-sized objects coming out of the main belt is simply much higher than the population created at low (a, e) orbits by NEAs (e.g., W. F. Bottke et al. 2005c, 2015a). For weaker meteorites like the CM and CI chondrites, we suspect that the meteorite flux is dominated by objects in Earth-crossing space that have high (a, e) orbits. The precursors for these objects would be collisionally coupled to the main belt, so in turn they would be far more likely to undergo cratering and disruption events. This idea is consistent with the orbits of CM and CI meteorite falls where a surviving sample has been identified, such as Tagish Lake, Maribo, Sutter's Mill, Winchcombe, Flensburg, and Orgueil; the fireballs for all of these meteorites had semimajor axes >2 au and eccentricities high enough to reach Earth-crossing orbits (M. Gounelle et al. 2006; M. Granvik & P. Brown 2018; J. Borovička et al. 2021; A. J. King et al. 2022).

Many CM and CI meteorite orbits are also associated with high-eccentricity regions where weak carbonaceous NEAs can potentially be broken down by thermal forces (e.g., M. Granvik et al. 2016; D. Nesvorný et al. 2023, 2024a). It is plausible that the disruption of sizable NEAs near the Sun could flood the meter-sized population with an influx of CM or CI materials. If they can survive long enough to get away from the Sun, this could explain observations. This idea could be further enhanced by YORP spin-up; it is more efficient near the Sun, which in turn would lead to more mass-shedding events.

In our unpublished numerical experiments of this scenario, however, we found that a substantial fraction of fragments from test asteroids that had disrupted near the Sun would eventually evolve to low (a, e) orbits. Ideally, they reside on those orbits for tens of Myr. Over time, we would expect the low (a, e) population to build up into a sizable steady-state population, as seen with the NEA population. Such a chain of events would negate our explanation for why $a > 2$ au objects dominate CM and CI falls. Clearly the meteorite delivery scenario discussed above is missing something important.

A possible solution comes from an unexpected source, namely the particle ejection events observed on Bennu. Several particle ejection events were observed between the end of 2018 December, the time when OSIRIS-REx entered into Bennu orbit, and 2019 February (D. S. Lauretta et al. 2019). The three largest events observed during this interval, which all occurred 3.5–6 hr after local noon, placed numerous $D < 10$ cm particles on temporary orbits around Bennu, with other objects ejected into the solar system. From an extensive analysis, two likely solutions emerged to explain the source of these events. One was the thermal fracturing of boulders (Molaro et al. 2020; B. Rozitis et al. 2020), and the second was meteoroid impacts (W. F. Bottke et al. 2020). Both could reasonably reproduce the constraints provided by Bennu's ejection events. For this paper, we will focus on the latter mechanism.

Meteoroids are small particles that are largely derived from disrupted Jupiter family comets and, to a lesser degree, nearly isotropic comets and main-belt asteroids (e.g., D. Nesvorný et al. 2010). They collide with everything, including spacecraft, Earth, the Moon, and asteroids. They can also strike bodies at very high speeds; while their estimated velocities at Bennu average $20\,\mathrm{km\,s^{-1}}$, retrograde particles can reach speeds between 40 and $80\,\mathrm{km\,s^{-1}}$. Calculations by W. F. Bottke et al. (2020) showed that Bennu was struck near perihelion every 2 weeks by 7000 J impact events. For reference, such blasts are the energy equivalent of shooting Bennu with a shotgun.

We postulate that meteoroid impacts are the missing component in our understanding of meteorite CRE ages. Unlike main-belt impactors, there are no dynamical hiding places from meteoroid impacts, and as semimajor axis decreases, the meteoroid flux increases within the inner solar system. The impact energies involved with meteoroid impacts are also more than sufficient to disrupt the immediate precursors of CM and CI chondrite meteorites, which should be considerably weaker than ordinary chondrites and achondrites. This would prevent such small bodies from building up a large steady-state population at low (a, e) orbits, even though these orbits are decoupled from the main belt.

As a simple test of this idea, consider two meteorite precursor populations, one made from weak CI and CM materials and another made from stronger ordinary chondrite and achondrite materials. Here we will assign a mean collisional lifetime to the two populations of 2 and 15 Myr, respectively, close to where we see the average CRE ages of each meteorite group (O. Eugster et al. 2006). Assuming that both start with the same population (N_0) and undergo exponential decay from meteoroid impacts, we find that the ratio of ordinary chondrite materials to CM/CI materials is ~80 after 10 Myr, ~6000 after 20 Myr, and ~440,000 after 30 Myr. These values suggest that if enough time passes, stronger materials will dominate the meteorite flux if both are started with the same initial conditions.

Note that this thought experiment ignores small-body replenishment via a collisional cascade. Based on our experience with collisional evolution models, though (e.g., W. F. Bottke et al. 2015a), if we assumed weaker C-complex bodies and stronger S-complex bodies within two identical SFDs and then let these SFDs collisionally evolve in the main belt, the results for meter-sized bodies would still favor the S-complex bodies. The reason is that the reservoir of bodies capable of meter-size replenishment would be decimated faster, which in turn would mean fewer meter-sized bodies.

At this point, we have enough information to try to put everything together. For sturdy materials such as ordinary chondrites, achondrites, and stronger carbonaceous chondrites like CKs, COs, and CVs, most of their flux can presumably come directly from the main belt (e.g., see review in W. F. Bottke et al. 2006b). This would explain why so many of these meteorite groups have CRE age distributions skewed to older ages. Additional meteorites can come directly from NEAs via a range of mechanisms: cratering events, disruption events, tidal disruption, or YORP-driven mass-shedding events. They would explain some of the younger CRE ages observed to date in these meteorite groups, but the net flux from these mechanisms is not enough to dominate the main-belt flux.

Conversely, for weaker CM and CI chondrites, their flux out of the main belt is presumably decimated by collisions en route to Earth-crossing orbits. This prevents many potential meteorites from obtaining long CRE ages. Instead, the meteorite flux for these compositions comes from bodies that have barely escaped the main belt or from more sizable objects already on Earth-crossing orbits. For the latter, they would be produced by cratering events, impact-driven disruption events, tidal disruption, and YORP-driven mass-shedding events. The fragments must reach Earth quickly after liberation, however, or meteoroid particles, main-belt projectiles, or extreme heating near the Sun will destroy them. This behavior explains why the CRE age distributions of the CM and CI meteorites are skewed toward young ages.

These ideas take us to the fact that all CM and CI meteorite falls with known orbits have $a > 2$ au. One explanation for this could be that many of the main-belt objects reaching Earth-crossing orbits via the ν_6 resonance, J3:1, or other related resonances spend some time with $a > 2$ au (W. F. Bottke et al. 2002; M. Granvik et al. 2018; D. Nesvorný et al. 2023). Accordingly, (i) many potential meteorites can hit Earth from this orbital zone, (ii) many NEAs can get close enough to the Sun to undergo some kind of thermal disruption (M. Granvik et al. 2016), (iii) objects with $a > 2$ au can be hit by main-belt projectiles, and (iv) many YORP-driven mass-shedding events can take place here. Conversely, attrition among the immediate precursors of CI and CM meteorites may be too strong to produce a strong meteorite component for $a < 2$ au. The fact that carbonaceous-chondrite-like asteroids are more likely to morph into new shapes rather than shed mass via YORP spin-up (and presumably tidal disruption; Y. Zhang et al. 2022) may also contribute to why few CM or CI falls come from $a < 2$ au.

7. Conclusions

Here we summarize the conclusions in this paper regarding the evolution of Bennu, Ryugu, and Itokawa.

Our numerical integration work has shown that Bennu, Ryugu, and Itokawa likely followed a "dynamical superhighway" that many NEAs take to reach Earth-like orbits (Sections 2.1–2.2; Figure 2). It drove them from the main belt via various resonances to an Earth-crossing orbit, where they were likely removed from resonance by an Earth encounter. From there, they had repeated encounters with Earth, allowing them to migrate down to low (a, e) orbits along lines of constant Tisserand invariant with Earth. Variations along these paths came from interactions with numerous small resonances that may have modified their eccentricities and inclinations. The median timescales for transitioning from the epoch when Bennu, Ryugu, and Itokawa first became Earth-crossing to their current (a, e, i) orbits were 7.6, 5.7, and 6.0 Myr, respectively (Figure 3).

During these transits, the asteroids were repeatedly struck by asteroids from three populations: the main belt, objects on solely Mars-crossing orbits with perihelion $q > 1.3$ au, and NEAs (Section 4.1). The main belt is the largest of the three populations (Figure 12) and can strike NEAs until their aphelion $Q < 1.6$ au. This implies that many craters on their surfaces are derived from main-belt impactors, even though they probably formed after the NEAs had reached an Earth-crossing orbit.

NEAs moving to Earth-like orbits along the dynamical superhighway can be hit by large impactors, mainly from the main belt (Section 2.3). They are also susceptible to YORP-driven mass-shedding events (Section 2.4) and close Earth encounters that can produce tidal distortion or disruption (Section 2.5). All three mechanisms can potentially produce regional or global resurfacing events.

Using the code NEA-EVOL, we tracked crater production on 75, 77, and 49 test asteroids that traveled from the main belt to the observed orbits of Bennu, Ryugu, and Itokawa (Section 4). Our crater production model used a scaling law from E. Tatsumi & S. Sugita (2018) that assumed that craters formed in the gravity regime, though we did not account for the effects of Boulder armoring (E. B. Bierhaus et al. 2022; Section 4.2). Typical ratios of crater sizes to projectile sizes during the runs were ∼70 but frequently reached values >100. We also tried to account for the erasure of craters between a few meters and 100 m in diameter using an empirical crater damage function. It assumed that smaller craters would be gradually erased by the mass movement of surface materials (Section 4.4).

Our model SFDs for each asteroid were compared to the observed crater SFDs of Bennu, Ryugu, and Itokawa (Section 5). For Bennu, we examined the SFD of craters least affected by space weathering, as well as its total crater SFD (Figure 8). We found that the median ages for the youngest craters ($D_{\rm crater} > 3$ m) were 0.22 Myr, with some model runs having ages as low as 60,000 yr (Figure 15, left). For the full crater SFD, the median surface age was found to be 7.8 Myr, with a peak value between 4 and 6 Myr (Figure 16, right). These values are consistent with the CRE ages of the Bennu samples measured so far, which have ages between 1 and 6 Myr (B. Marty et al. 2024).

For Ryugu (Section 5.2), we compared our model SFDs to the observed total crater SFD (Figure 9). Our median model surface age was 4.1 Myr, with most runs having ages <8 Myr. These values are consistent with the CRE ages of the Ryugu samples measured so far, which have ages <5.8–7.8 Myr, depending on the chamber measured (T. Yada et al. 2021; K. Nagao et al. 2022; R. Okazaki et al. 2022; K. Nishiizumi & M. W. Caffee 2023).

For Itokawa (Section 5.3), we compared our model SFD to the observed SFD in Figure 10. We found that the median age of its surface is 3.1 Myr, with most runs having ages <10–15 Myr. The CRE ages of Itokawa samples are similar, with ages going from ∼1 Myr to an upper limit of ∼8 Myr (K. Nagao et al. 2011; M. M. M. Meier et al. 2013; 2014). These timescales are shorter than the CRE ages of most LL chondrites, which mostly range between 5 and 50 Myr and peak near ∼15 Myr (O. Eugster et al. 2006).

The surface ages of Bennu and Ryugu, as well as the CRE ages of their samples, are broadly consistent with the CRE ages found for CI and CM meteorites (Sections 5.1.2, 5.2.2, 6.2). For the two meteorite classes, most have CRE ages ranging between 0.1 Myr and several Myr, and almost none are older than 8 Myr. A reasonable interpretation is that their durability is limited and that meter-sized objects are readily destroyed, possibly by meteoroid impacts (Section 6.2). This leads us to favor the idea that many of the CM and CI meteorites do not evolve out of the main belt intact but instead need to ride on larger immediate precursors that act as a “mothership” that transports them to near-Earth space. Many of these large precursors are destroyed with $a > 2$ au orbits, explaining the plethora of CM and CI meteorite falls with these orbits. Conversely, stronger meteorites, such as ordinary chondrites, can probably reach their final size while migrating within the main belt.

Finally, our results suggest that impacts and YORP-spin-up-driven mass-shedding events produce a fair amount of churn on NEAs with Earth-like orbits (Section 6.1) (Figure 18). Tidal resurfacing is also possible, but it is more likely for Ryugu and Itokawa than for Bennu (Figure 6). Given that tidal resurfacing is most probable for objects near the Earth-crossing line on low (a, e) orbits and that few of our test asteroids had their craters reset on those orbits, we argue that tidal resurfacing was not a primary crater erasure mechanism for Bennu, Ryugu, or Itokawa.

Acknowledgments

We thank the OSIRIS-REx mission and team for their support, where these ideas were first considered as part of a larger work on the evolution of NEAs and meteorite precursors. We also thank Kevin Walsh for his comments and for being part of many interesting discussions. We appreciate the useful comments and suggestions provided by our two anonymous referees, which made this a better paper. The work in this paper was supported by NASA’s New Frontiers Data Analysis program through grant 80NSSC21K0828. The work of D.V. was partially supported by the Czech Science Foundation (grant 25-16507S).

ORCID iDs

William F. Bottke https://orcid.org/0000-0002-1804-7814
Alex J. Meyer https://orcid.org/0000-0001-8437-1076
David Vokrouhlický https://orcid.org/0000-0002-6034-5452
David Nesvorný https://orcid.org/0000-0002-4547-4301
Edward B. Bierhaus https://orcid.org/0000-0001-5890-9821
Daniella N. DellaGiustina https://orcid.org/0000-0002-5643-1956
Rachael Hoover https://orcid.org/0000-0003-0926-7513
Harold C. Connolly https://orcid.org/0000-0002-1803-5098
Dante S. Lauretta https://orcid.org/0000-0002-2597-5950

References

Abell, P. A., Korsmeyer, D. J., Landis, R. R., et al. 2009, M&PS, 44, 1825
Agrusa, H. F., Zhang, Y., Richardson, D. C., et al. 2024, PSJ, 5, 54
Arakawa, M., Saiki, T., Wada, K., et al. 2020, Sci, 368, 67
Asphaug, E., & Benz, W. 1996, Icar, 121, 225
Avdellidou, C., Delbo’, M., Nesvorný, D., Walsh, K. J., & Morbidelli, A. 2024, Sci, 384, 348
Ballouz, R.-L., Walsh, K. J., Barnouin, O. S., et al. 2020, Natur, 587, 205
Barnouin, O. S., Daly, M. G., Seabrook, J. A., et al. 2022, JGRE, 127, e06927
Barnouin, O. S., Ballouz, R.-L., Marchi, S., et al. 2024, NatCo, 15, 6202
Bierhaus, E. B., Rossmann, F., Johnson, C., et al. 2023, Icar, 406, 115736
Bierhaus, E. B., Trang, D., Daly, R. T., et al. 2022, NatGe, 15, 440
Binzel, R. P., DeMeo, F. E., Turtelboom, E. V., et al. 2019, Icar, 324, 41
Binzel, R. P., Morbidelli, A., Merouane, S., et al. 2010, Natur, 463, 331
Bonal, L., Brunetto, R., Beck, P., et al. 2015, M&PS, 50, 1562

Borovička, J., Bettonvil, F., Baumgarten, G., et al. 2021, M&PS, 56, 425
Bottke, W. F., Brož, M., O'Brien, D. P., et al. 2015a, in Asteroids IV, ed. P. Michel, F. E. DeMeo, & W. F. Bottke (Tucson, AZ: Univ. Arizona Press), 701
Bottke, W. F., & Chapman, C. R. 2006, LPSC, 37, 1349
Bottke, W. F., Durda, D. D., Nesvorný, D., et al. 2005a, Icar, 175, 111
Bottke, W. F., Durda, D. D., Nesvorný, D., et al. 2005b, Icar, 179, 63
Bottke, W. F., Durda, D., Nesvorný, D., et al. 2005c, in IAU Colloq. 197, Dynamics of Populations of Planetary Systems (Cambridge: Cambridge Univ. Press), 357
Bottke, W. F., Morbidelli, A., Jedicke, R., et al. 2002, Icar, 156, 399
Bottke, W. F., Nesvorný, D., Grimm, R. E., Morbidelli, A., & O'Brien, D. P. 2006a, Natur, 439, 821
Bottke, W. F., Nesvorný, D., Vokrouhlický, D., & Morbidelli, A. 2010, AJ, 139, 994
Bottke, W. F., Nolan, M. C., Greenberg, R., & Kolvoord, R. A. 1994a, Icar, 107, 255
Bottke, W. F., Nolan, M. C., Greenberg, R., & Kolvoord, R. A. 1994b, in Hazards Due to Comets and Asteroids, ed. T. Gehrels, M. S. Matthews, & A. Schumann (Tucson, AZ: Univ. Arizona Press), 337
Bottke, W. F., Nolan, M. C., Melosh, H. J., Vickery, A. M., & Greenberg, R. 1996, Icar, 122, 406
Bottke, W. F., Richardson, D. C., & Love, S. G. 1998, P&SS, 46, 311,317
Bottke, W. F., Richardson, D. C., Michel, P., & Love, S. G. 1999, AJ, 117, 1921
Bottke, W. F., Vokrouhlický, D., Ballouz, R.-L., et al. 2020, AJ, 160, 14
Bottke, W. F., Vokrouhlický, D., Marschall, R., et al. 2023, PSJ, 4, 168
Bottke, W. F., Vokrouhlický, D., Nesvorný, D., et al. 2024, PSJ, 5, 88
Bottke, W. F., Vokrouhlický, D., Rubincam, D. P., & Nesvorný, D. 2006b, AREPS, 34, 157
Bottke, W. F., Vokrouhlický, D., Walsh, K. J., et al. 2015b, Icar, 247, 191
Brož, M., Vernazza, P., Marsset, M., et al. 2024, A&A, 689, A183
Burbine, T. H., McCoy, T. J., Meibom, A., Gladman, B., & Keil, K. 2002, in Asteroids III, ed. W. F. Bottke, Jr. (Tucson, AZ: Univ. Arizona Press), 653
Burke, K. N., DellaGiustina, D. N., Bennett, C. A., et al. 2021, RemS, 13, 1315
Campins, H., de León, J., Morbidelli, A., et al. 2013, AJ, 146, 26
Campins, H., Morbidelli, A., Tsiganis, K., et al. 2010, ApJL, 721, L53
Čapek, D., & Vokrouhlický, D. 2004, Icar, 172, 526
Chapman, C. R. 2002, in Asteroids IV, ed. W. F. Bottke, Jr. et al. (Tucson, AZ: Univ. Arizona Press), 315
Chapman, C. R., & McKinnon, W. B. 1986, in IAU Colloq. 77, Some Background about Satellites (Tucson, AZ: Univ. Arizona Press), 492
Chesley, S. R., Farnocchia, D., Nolan, M. C., et al. 2014, Icar, 235, 5
Cho, Y., Morota, T., Kanamaru, M., et al. 2021, JGRE, 126, e06572
Daly, M. G., Barnouin, O. S., Dickinson, C., et al. 2017, SSRv, 212, 899
Daly, M. G., Barnouin, O. S., Seabrook, J. A., et al. 2020, SciA, 6, eabd3649
Daly, R. T., Barnouin, O. S., Bierhaus, E. B., et al. 2022, Icar, 384, 115058
de León, J., Licandro, J., Serra-Ricart, M., Pinilla-Alonso, N., & Campins, H. 2010, A&A, 517, A23
de León, J., Pinilla-Alonso, N., Delbo, M., et al. 2016, Icar, 266, 57
Delbo, M., Avdellidou, C., & Walsh, K. J. 2023, A&A, 680, A10
Delbo, M., & Michel, P. 2011, ApJL, 728, L42
DellaGiustina, D. N., Bennett, C. A., Becker, K., et al. 2018, E&SS, 5, 929
DellaGiustina, D. N., Burke, K. N., Walsh, K. J., et al. 2020, Sci, 370, eabc3660
DellaGiustina, D. N., Emery, J. P., Golish, D. R., et al. 2019, NatAs, 3, 341
DellaGiustina, D. N., Kaplan, H. H., Simon, A. A., et al. 2021, NatAs, 5, 31
DellaGiustina, D. N., Nolan, M. C., Polit, A. T., et al. 2023, PSJ, 4, 198
Demura, H., Kobayashi, S., Nemoto, E., et al. 2006, Sci, 312, 1347
Dunn, T. L., Burbine, T. H., Bottke, W. F., & Clark, J. P. 2013, Icar, 222, 273
Ďurech, J., & Hanuš, J. 2023, A&A, 675, A24
Ďurech, J., Vokrouhlický, D., Pravec, P., et al. 2024, A&A, 682, A93
Dykhuis, M. J., Molnar, L., Van Kooten, S. J., & Greenberg, R. 2014, Icar, 243, 111
Eugster, O., Herzog, G. F., Marti, K., & Caffee, M. W. 2006, in Meteorites and the Early Solar System II, ed. D. S. Lauretta & H. Y. McSween, Jr. (Tucson, AZ: Univ. Arizona Press), 829
Farinella, P., & Davis, D. R. 1992, Icar, 97, 111
Farinella, P., Vokrouhlický, D., & Hartmann, W. K. 1998, Icar, 132, 378
Fowler, J. W., & Chillemi, J. R. 1992, IRAS Asteroid Data Processing, The IRAS Minor Planet Survey, Tech. Rep. PLTR-92-2049, Phillips Laboratory, https://irsa.ipac.caltech.edu/IRASdocs/surveys/PL-TR-92-2049.pdf
Fujiwara, A., Kawaguchi, J., Yeomans, D. K., et al. 2006, Sci, 312, 1330
Gault, D. E. 1970, RaSc, 5, 273
Granvik, M., & Brown, P. 2018, Icar, 311, 271
Granvik, M., Morbidelli, A., Jedicke, R., et al. 2016, Natur, 530, 303
Granvik, M., Morbidelli, A., Jedicke, R., et al. 2018, Icar, 312, 181
Granvik, M., & Walsh, K. J. 2024, ApJL, 960, L9
Graves, K. J., Minton, D. A., Hirabayashi, M., DeMeo, F. E., & Carry, B. 2018, Icar, 304, 162
Greenberg, R., Bottke, W. F., Nolan, M., et al. 1996, Icar, 120, 106
Greenberg, R., & Nolan, M. C. 1993, Resources of Near-Earth Space (Tucson, AZ: Univ. Arizona Press), 473
Greenberg, R., Nolan, M. C., Bottke, W. F., Kolvoord, R. A., & Veverka, J. 1994, Icar, 107, 84
Gounelle, M., Spurný, P., & Bland, P. A. 2006, M&PS, 41, 135
Hamilton, V. E., Simon, A. A., Christensen, P. R., et al. 2019, NatAs, 3, 332
Harris, A. W., & Chodas, P. W. 2021, Icar, 365, 114452
Hartzell, C. M. 2019, Icar, 333, 234
Hartzell, C. M., & Scheeres, D. J. 2013, JGRE, 118, 116
Hergenrother, C. W., Maleszewski, C. K., Nolan, M. C., et al. 2019, NatCo, 10, 1291
Hirabayashi, M., Nakano, R., Tatsumi, E., et al. 2020, Icar, 352, 113946
Hirabayashi, M., Sánchez, D. P., & Scheeres, D. J. 2015, ApJ, 808, 63
Hirata, N., Barnouin-Jha, O. S., Honda, C., et al. 2009, Icar, 200, 486
Hirata, N., Morota, T., Cho, Y., et al. 2020, Icar, 338, 113527
Hirata, N., Namiki, N., Yoshida, F., et al. 2021, Icar, 354, 114073
Honda, R., Arakawa, M., Shimaki, Y., et al. 2021, Icar, 366, 114530
Housen, K. R., & Holsapple, K. A. 1999, Icar, 142, 21
Hu, Y., Moynier, F., Dai, W., et al. 2024, Icar, 409, 115884
Hudson, R. S., & Ostro, S. J. 1999, Icar, 140, 369
Hyodo, R., & Sugiura, K. 2022, ApJL, 937, L36
Jaumann, R., Schmitz, N., Ho, T.-M., et al. 2019, Sci, 365, 817
Jawin, E. R., McCoy, T. J., Walsh, K. J., et al. 2022, Icar, 381, 114992
Jawin, E. R., Walsh, K. J., Barnouin, O. S., et al. 2020, JGRE, 125, e06475
Jourdan, F., Timms, N. E., Nakamura, T., et al. 2023, PNAS, 120, e2214353120
Jutzi, M., Raducan, S. D., Zhang, Y., Michel, P., & Arakawa, M. 2022, NatCo, 13, 7134
Kanamaru, M., Sasaki, S., & Wieczorek, M. 2019, P&SS, 174, 32
Kaplan, H. H., Lauretta, D. S., Simon, A. A., et al. 2020, Sci, 370, eabc3557
Keller, L. P., & Berger, E. L. 2014, EP&S, 66, 71
Kim, Y., DeMartini, J. V., Richardson, D. C., & Hirabayashi, M. 2023, MNRAS, 520, 3405
King, A. J., Daly, L., Rowe, J., et al. 2022, SciA, 8, eabq3925
King, A. J., Schofield, P. F., & Russell, S. S. 2021, GeCoA, 298, 167
Kitazato, K., Milliken, R. E., Iwata, T., et al. 2021, NatAs, 5, 246
Kleine, T., Budde, G., Burkhardt, C., et al. 2020, SSRv, 216, 55
Krietsch, D., Busemann, H., Riebe, M. E. I., et al. 2021, GeCoA, 310, 240
Koga, S., Sugita, S., Kamata, S., et al. 2014, LPSC, 45, 1721
Lantz, C., Brunetto, R., Barucci, M. A., et al. 2017, Icar, 285, 43
Lauretta, D. S., Adam, C. D., Allen, A. J., et al. 2022, Sci, 377, 285
Lauretta, D. S., Balram-Knutson, S. S., Beshore, E., et al. 2017, SSRv, 212, 925
Lauretta, D. S., Connolly, H. C., Aebersold, J. E., et al. 2024, M&PS, 59, 2453
Lauretta, D. S., Dellagiustina, D. N., Bennett, C. A., et al. 2019, Natur, 568, 55
Levison, H. F., & Duncan, M. J. 1994, Icar, 108, 18
Levison, H. F., Marchi, S., Noll, K. S., et al. 2024, Natur, 629, 1015
Liberato, L., Tanga, P., Mary, D., et al. 2024, A&A, 688, A50
Lowry, S. C., Weissman, P. R., Duddy, S. R., et al. 2014, A&A, 562, A48
Marchi, S., Bierhaus, B., Robbins, S., et al. 2024, LPSC, 3040, 1520
Marchi, S., Bottke, W. F., Kring, D. A., & Morbidelli, A. 2012, E&PSL, 325, 27
Marchi, S., Chapman, C. R., Barnouin, O. S., Richardson, J. E., & Vincent, J.-B. 2015, in Asteroids IV, ed. P. Michel, F. E. DeMeo, & W. F. Bottke (Tucson, AZ: Univ. Arizona Press), 725
Margot, J.-L., Pravec, P., Taylor, P., Carry, B., & Jacobson, S. 2015, in Asteroids IV, ed. P. Michel, F. E. DeMeo, & W. F. Bottke (Tucson, AZ: Univ. Arizona Press), 355
Marty, B., Zimmermann, L., Füri, E., et al. 2024, LPICo, 3036, 6428
Masiero, J. R., Mainzer, A. K., Grav, T., et al. 2011, ApJ, 741, 68
Matsumura, S., Richardson, D. C., Michel, P., Schwartz, S. R., & Ballouz, R.-L. 2014, MNRAS, 443, 3368
Maurel, C., Ballouz, R.-L., Richardson, D. C., Michel, P., & Schwartz, S. R. 2017, MNRAS, 464, 2866
McCain, K. A., Matsuda, N., Liu, M.-C., et al. 2023, NatAs, 7, 309
McCoy, T. J., Russell, S. S., Zega, T. J., et al. 2025, Natur, 637 1072
Meier, M. M. M., Alwmark, C., Bajt, S., et al. 2013, LPSC, 44, 1937
Meier, M. M. M., Alwmark, C., Bajt, S., et al. 2014, LPSC, 45, 1247

Melosh, H. J. 1989, Impact Cratering: A Geologic Process, Vol. 11 (Oxford: Clarendon), 245
Meyer, A. J., & Scheeres, D. J. 2024, ApJL, 963, L14
Michel, P., Ballouz, R.-L., Barnouin, O. S., et al. 2020, NatCo, 11, 2655
Michel, P., Küppers, M., Bagatin, A. C., et al. 2022, PSJ, 3, 160
Michel, P., O'Brien, D. P., Abe, S., & Hirata, N. 2009, Icar, 200, 503
Minker, K., & Carry, B. 2023, A&A, 672, A48
Miyamoto, H., Yano, H., Scheeres, D. J., et al. 2007, Sci, 316, 1011
Morbidelli, A., Bottke, W. F., Nesvorný, D., & Levison, H. F. 2009, Icar, 204, 558
Morbidelli, A., Gounelle, M., Levison, H. F., & Bottke, W. F. 2006, M&PS, 41, 874
Morota, T., Sugita, S., Cho, Y., et al. 2020, Sci, 368, 654
Nagao, K., Okazaki, R., Nakamura, T., et al. 2011, Sci, 333, 1128
Nagao, K., Okazaki, R., Nishiizumi, K., et al. 2022, LPICo, 85, 6320
Nakamura, T., Matsumoto, M., Amano, K., et al. 2023, Sci, 379, abn8671
Nakamura, T., Noguchi, T., Tanaka, M., et al. 2011, Sci, 333, 1113
Nesvorný, D., Bottke, W. F., Vokrouhlický, D., Chapman, C. R., & Rafkin, S. 2010, Icar, 209, 510
Nesvorný, D., Brož, M., & Carruba, V. 2015, in Asteroids IV, ed. P. Michel, F. E. DeMeo, & W. F. Bottke (Tucson, AZ: Univ. Arizona Press), 297
Nesvorný, D., Deienno, R., Bottke, W. F., et al. 2023, AJ, 166, 55
Nesvorný, D., Vokrouhlický, D., Shelly, F., et al. 2024a, Icar, 411, 115922
Nesvorný, D., Vokrouhlický, D., Shelly, F., et al. 2024b, Icar, 417, 116110
Nishiizumi, K., & Caffee, M. W. 2012, LPSC, 43, 2758
Nishiizumi, K., & Caffee, M. W. 2023, LPICo, 86, 6280
Nishiizumi, K., Caffee, M. W., & Welten, K. C. 2015, LPSC, 46, 2499
Nishiyama, G., Kawamura, T., Namiki, N., et al. 2021, JGRE, 126, e06594
O'Brien, D. P., & Greenberg, R. 2005, Icar, 178, 179
O'Brien, D. P., Greenberg, R., & Richardson, J. E. 2006, Icar, 183, 79
Okazaki, R., Miura, Y. N., Takano, Y., et al. 2022, SciA, 8, eabo7239
Park, J., Turrin, B. D., Herzog, G. F., et al. 2015, M&PS, 50, 2087
Perera, V., Jackson, A. P., Asphaug, E., & Ballouz, R.-L. 2016, Icar, 278, 194
Perry, M. E., Barnouin, O. S., Daly, R. T., et al. 2022, NatGe, 15, 447
Pinilla-Alonso, N., de León, J., Walsh, K. J., et al. 2016, Icar, 274, 231
Pravec, P., & Harris, A. W. 2007, Icar, 190, 250
Raducan, S. D., Jutzi, M., Cheng, A. F., et al. 2024, NatAs, 8, 445
Raymond, S. N., & Izidoro, A. 2017, SciA, 3, e1701138
Richardson, D. C., Bottke, W. F., & Love, S. G. 1998, Icar, 134, 47
Richardson, D. C., Leinhardt, Z. M., Melosh, H. J., Bottke, W. F., & Asphaug, E. 2002, in Asteroids III, ed. W. F. Bottke, Jr. (Tucson, AZ: Univ. Arizona Press), 501
Richardson, J. E. 2009, Icar, 204, 697
Richardson, J. E., Melosh, H. J., Greenberg, R. J., & O'Brien, D. P. 2005, Icar, 179, 325
Richardson, J. E., Steckloff, J. K., & Minton, D. A. 2020, Icar, 347, 113811
Rossi, A., Marzari, F., & Scheeres, D. J. 2009, Icar, 202, 95
Rozitis, B., & Green, S. F. 2013a, MNRAS, 433, 603
Rozitis, B., & Green, S. F. 2013b, MNRAS, 430, 1376
Rozitis, B., Ryan, A. J., Emery, J. P., et al. 2020, SciA, 6, eabc3699
Rozitis, B., Ryan, A. J., Emery, J. P., et al. 2022, JGRE, 127, e07153
Rubincam, D. P. 2000, Icar, 148, 2
Saito, J., Miyamoto, H., Nakamura, R., et al. 2006, Sci, 312, 1341
Scheeres, D. J. 2015, Icar, 247, 1
Sridhar, S., & Tremaine, S. 1992, Icar, 95, 86
Statler, T. S. 2009, Icar, 202, 502
Sugita, S., Honda, R., Morota, T., et al. 2019, Sci, 364, eaaw0422
Tachibana, S., Sawada, H., Okazaki, R., et al. 2022, Sci, 375, 1011
Takaki, N., Cho, Y., Morota, T., et al. 2022, Icar, 377, 114911
Takir, D., Emery, J. P., Bottke, W. F., & Arredondo, A. 2024, NatSR, 14, 15965
Tang, Y., Lauretta, D. S., Ballouz, R.-L., et al. 2023, Icar, 395, 115463
Tang, Y., Lauretta, D. S., Ballouz, R.-L., et al. 2024, Icar, 415, 116056
Tatsumi, E., Popescu, M., Campins, H., et al. 2021b, MNRAS, 508, 2053
Tatsumi, E., Sakatani, N., Riu, L., et al. 2021a, NatCo, 12, 5837
Tatsumi, E., Sugimoto, C., Riu, L., et al. 2021c, NatAs, 5, 39
Tatsumi, E., & Sugita, S. 2018, Icar, 300, 227
Terada, K., Sano, Y., Takahata, N., et al. 2018, NatSR, 8, 11806
Thomas, P. C., & Robinson, M. S. 2005, Natur, 436, 366
Trieloff, M., Korochantseva, E. V., Buikin, A. I., et al. 2018, M&PS, 53, 343
Tonui, E., Zolensky, M., Hiroi, T., et al. 2014, GeCoA, 126, 284
Tsuchiyama, A., Nakano, T., Uesugi, K., et al. 2013, GeCoA, 116, 5
Tsuchiyama, A., Uesugi, M., Matsushima, T., et al. 2011, Sci, 333, 1125
Vernazza, P., Binzel, R. P., Thomas, C. A., et al. 2008, Natur, 454, 858
Vokrouhlický, D., Bottke, W. F., Chesley, S. R., Scheeres, D. J., & Statler, T. S. 2015, in Asteroids IV, ed. P. Michel, F. E. DeMeo, & W. F. Bottke (Tucson, AZ: Univ. Arizona Press), 509
Vokrouhlický, D., Bottke, W. F., & Nesvorný, D. 2017, AJ, 153, 172
Vokrouhlický, D., Čapek, D., Kaasalainen, M., & Ostro, S. J. 2004, A&A, 414, L21
Vokrouhlický, D., & Nesvorný, D. 2008, AJ, 136, 280
Walsh, K. J. 2018, ARA&A, 56, 593
Walsh, K. J., Ballouz, R.-L., Bottke, W. F., et al. 2024, NatCo, 15, 5653
Walsh, K. J., Delbó, M., Bottke, W. F., Vokrouhlický, D., & Lauretta, D. S. 2013, Icar, 225, 283
Walsh, K. J., & Jacobson, S. A. 2015, in Asteroids IV, ed. P. Michel, F. E. DeMeo, & W. F. Bottke (Tucson, AZ: Univ. Arizona Pres), 375
Walsh, K. J., Jawin, E. R., Ballouz, R.-L., et al. 2019, NatGe, 12, 242
Walsh, K. J., Morbidelli, A., Raymond, S. N., O'Brien, D. P., & Mandell, A. M. 2011, Natur, 475, 206
Walsh, K. J., & Richardson, D. C. 2006, Icar, 180, 201
Walsh, K. J., & Richardson, D. C. 2008, Icar, 193, 553
Walsh, K. J., Richardson, D. C., & Michel, P. 2008, Natur, 454, 188
Watanabe, S., Hirabayashi, M., Hirata, N., et al. 2019, Sci, 364, 268
Watanabe, S., Tsuda, Y., Yoshikawa, M., et al. 2017, SSRv, 208, 3
Wieler, R. 2002, RvMG, 47, 125
Woronow, A. 1985, JGRS, 90, C817
Yada, T., Abe, M., Okada, T., et al. 2021, NatAs, 6, 214
Yamada, T. M., Ando, K., Morota, T., & Katsuragi, H. 2016, Icar, 272, 165
Yano, H., Kubota, T., Miyamoto, H., et al. 2006, Sci, 312, 1350
Yokoyama, T., Nagashima, K., Nakai, I., et al. 2023a, Sci, 379, abn7850
Yokoyama, T., Wadhwa, M., Iizuka, T., et al. 2023b, SciA, 9, eadi7048
Yoshikawa, M., Kawaguchi, J., Fujiwara, A., & Tsuchiyama, A. 2015, in Asteroids IV, ed. P. Michel, F. E. DeMeo, & W. F. Bottke (Tucson, AZ: Univ. Arizona Press), 397
Zhang, Y., Michel, P., Barnouin, O. S., et al. 2022, NatCo, 13, 4589
Zolensky, M., Velbel, M., & Le, L. 2020, LPSC, 51, 1946